Impact of Mud Contamination on Performance of Granite-Based Geopolymers

by

Pouya Khalili

Thesis submitted in fulfilment of
the requirements for the degree of
PHILOSOPHIAE DOCTOR
(PhD)

University
of Stavanger

Faculty of Science and Technology
Institute of Energy and Petroleum Engineering
2024

University of Stavanger
NO-4036 Stavanger
NORWAY
www.uis.no

ISBN:978-82-8439-262-2
ISSN:1890-1387
PhD: Thesis UiS No. 782

Acknowledgements

I would like to express my sincere gratitude to my supervisors, Professor Mahmoud Khalifeh and Professor Arild Saasen, for their invaluable guidance and support throughout this project. I would also like to thank my co-supervisor Dr. Jan Aage Aasen and Dr. Jostein Djuve for their support.

I gratefully acknowledge TotalEnergies, AkerBP, ConocoPhillips and Research Council of Norway for financially supporting the SafeRock KPN Project (RCN #319014- New Cementitious Material for Oil Well Cementing Applications - SafeRock) at the University of Stavanger, Norway. Special thanks to Laurent Delabroy and Gunnar Lende, Roy Middelton, Johan Kverneland, Carl Johnson, and Mohamed Oukil Benmesbah for their valuable contributions throughout the project.

A heartfelt thank you to all the staff and engineers at the Department of Energy and Petroleum Engineering (IEP) for their support throughout my three-year project. I extend my gratitude to Øystein Arild, Hilde Jonsbråten, Kim Andre Vorland, Caroline Rudd, Olaf Cezary Normann, Inger Johanne Olsen, Caroline Einvik, and Emil Kristiansen. Your assistance has been essential to the success of this project.

I would like to also express my gratitude to the staff at Pontifical Catholic University of Rio de Janeiro, particularly Professor Monica Naccache, Professor Paulo R.de Souza Mendes, Dr. Elias Rodrigues, and Dr. Behbood Abedi. I appreciate the support provided by the team during my exchange period.

I want to thank my friends and colleagues in the SWIPA Lab at UiS for your continuous support and assistance throughout this project. A special thanks to Dr. Mohammadreza Kamali, Dr. Sajjad Yousefi Oderji, Dr. Fawzi Chamssine, and Mr. Seyed Hasan Hajiabadi.

Last but certainly not least, I want to thank my father, mother, and sister. Your unconditional support has been my guiding light.

Pouya Khalili

Stavanger- March 2024

Preface

Ensuring zonal isolation and long-term integrity are fundamental in primary cementing in the well construction phase. Successful cementing can be compromised by various factors, including contamination with drilling fluid. Given that drilling fluid is present in the wellbore before cementitious material is pumped, it is possible that mixing between these fluids takes place downhole, affecting the properties of the barrier material. To mitigate this, spacer fluid is normally pumped in front of the cement slurry to minimize the commingling of drilling fluid and improve bonding. Geopolymer is seen as a potential replacement for Ordinary Portland Cement. Prior to its use in well construction and abandonment, the impact of drilling fluid contamination on geopolymer performance must be assessed.

In this study, the impact of drilling fluid contamination on the liquid-state and solid-state properties of granite-based geopolymer, developed at the University of Stavanger (UiS), was investigated at elevated temperatures (50 ℃ BHCT/70 ℃ BHST). Oil-based drilling fluid (OBDF) and water-based drilling fluid (WBDF) were formulated in the lab with representative mix designs for the contamination study. Additionally, a spacer fluid tailored for geopolymer was designed to minimize contamination by drilling fluid. The thesis presented here is the result of the SafeRock Project, a collaboration between UiS and operators aimed to meet industry standards with geopolymeric materials.

The PhD dissertation is structured into two primary sections: the first section outlines the research project, while the second section consists of appended papers comprising detailed scientific findings. The outcomes of this research have been published across five scientific papers: three in journals, one in a peer-reviewed conference, and one in an SPE conference. These papers are included as appendices and are labeled using Roman numerals. Throughout this thesis, the same numerals are utilized for the sake of referring.

Paper I: Geopolymer slurry was contaminated with different ratios of OBDF and WBDF, and its rheological behavior was analysed at 50°C. The flow curve, viscoelastic properties, gel strength, and rheological parameters of the geopolymer, post contamination, were investigated in the study. Experimental measurements were conducted using a scientific rheometer and a V-G meter, serving as industry-standard equipment, to ensure comparisons of the results.

Paper II: The effect of OBDF and WBDF contamination on the mechanical properties of geopolymer was investigated. The analysis targeted compressive strength, tensile strength, sonic strength development, and microstructure of the geopolymer.

Paper III: A hardening spacer was developed for the geopolymer. The design process consisted of tuning the viscosity profile with conventional rheology modifiers and optimizing the surfactant content to remove the drilling fluid layer from the casing and water-wet the surface. Finally, a compatibility study of the optimized spacer with geopolymer was performed.

Paper IV: The rheological compatibility of various mixtures of the spacer with OBDF was examined using a rheometer, and the resulting R-index, a measure of compatibility between downhole fluids, was determined. Additionally, the influence of surfactant in the spacer design on rheological compatibility was investigated. A small-scale mud displacement experiment was conducted to assess the effect of surfactant on drilling fluid displacement.

Paper V: A case study was conducted using 2D simulations to examine the process of drilling fluid displacement by spacer and geopolymer. The aim was to mitigate the risk associated with deploying new materials by quantitatively predicting optimal practices, including viscosity and density hierarchies while minimizing eccentricity to enhance displacement efficiency.

Appendix 6 presents a filed patent in Norway and Europe titled ‘LOW DENSE SETTABALE GEOPOLYMER SLURRY COMPRISING A SWELLABLE CLAY, AND SETTABLE TREATMENT FLUIDS OBTAINABLE FROM THE SLURRY’.

List of Publications

I. P. Khalili, M. Khalifeh, and A. Saasen, "The Effect of Fluid Contamination on Rheological Properties of Geopolymer Materials," presented at the ASME 2022 41st International Conference on Ocean, Offshore and Arctic Engineering, 2022. https://doi.org/10.1115/OMAE2022-78994.

II. P. Khalili, M. Khalifeh, and A. Saasen, "The Effect of Drilling Fluid Contamination on the Properties of Granite-Based Geopolymers at Elevated Temperature," Paper presented at the IADC/SPE International Drilling Conference and Exhibition, Galveston, Texas, USA, March 2024. doi: https://doi.org/10.2118/217942-MS.

III. P. Khalili, M. Khalifeh, A. Saasen, J. Djuve, and L. Delabroy " Experimental Evaluation of Hardening Spacer for Rock-Based Geopolymer," (submitted to a scientific journal 2024)

IV. P. Khalili, M. Khalifeh, A. Saasen, and M. Naccache, "Rheological Compatibility of a Hardening Spacer Fluid and Oil-Based Drilling Fluid," SPE Journal, pp. 1-16, 2023, doi: 10.2118/217446-pa.

V. A. Renteria, P. Khalili, I. Frigaard, and M. Khalifeh, "A case study for tailored formulation of geopolymers aided by annular displacement simulations," Geoenergy Science and Engineering, vol. 229, p. 212110, 2023/10/01/ 2023, doi: https://doi.org/10.1016/j.geoen.2023.212110.

Table of Contents

Table of Figures

List of Tables

1. Introduction

In this chapter we delve into the background of this study by discussing the fundamentals of well cementing and presenting an alternative barrier material to OPC (Ordinary Portland Cement) called geopolymer. Subsequently, mud displacement which is an integral part of the well cementing program is explained. Finally, we present investigation results of the major contamination impact of mud on the OPC properties as the dominant barrier material currently used in the industry, assuming the mud displacement is unsuccessful.

1.1 Well cementing and zonal isolation

The construction of wells is of utmost importance in deep subsurface activities. This involves drilling and cementing, known as primary cementing (Figure 1). Drilling entails a rotating drill bit penetrating the subsurface rocks while drilling fluid transports the cuttings to the surface through the annular space between the drill pipe and the borehole wall. Controlling pressure with the drilling fluid is crucial, as too light or heavy mud can lead to risks like fluid influx or reservoir fracture. When a desired depth (decided based on the geological information) is reached, the casing is run into the hole. Cementing involves conditioning the hole, cleaning it with preflush fluids, and pumping in cement slurry to form a solid seal around the casing. The cement surrounding the casing serves various purposes, such as ensuring zonal isolation by preventing the migration of formation fluids between distinct zones, protecting freshwater formation, casing corrosion protection, and securing the casing in its position. It is important to have a superior-quality cement as an annular barrier to maintain the integrity of the well. The industry standard document Norsok D-010 [1], which outlines specifications and recommendations concerning well integrity during drilling and later activities defines qualified well barrier elements, among others, with the ability to: i) tolerate the maximum temperature and pressure that might be subjected to ii) function effectively and tolerate the environment that can be in contact with during its expected lifetime.

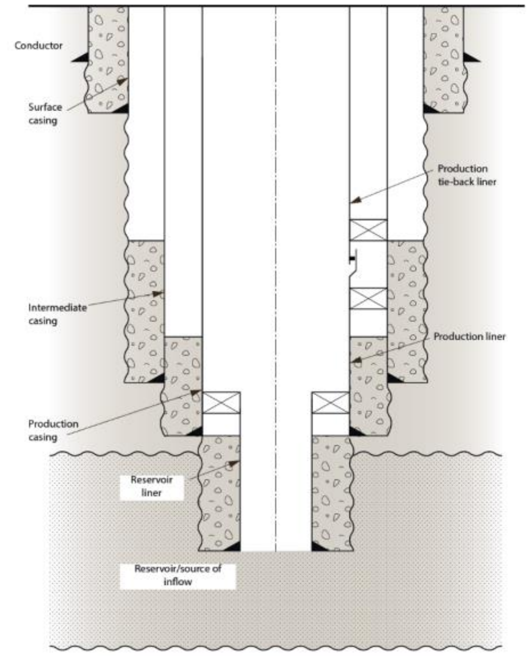

Figure 1 : Placing cement barrier in annulus during well construction [1]

A common outcome of compromised well integrity is the sustained casing pressure (SCP). This signifies that pressure persists in the annular gap between casings or between the casing and the formation, despite attempts to release it to zero at the surface. SCP indicates imperfect zonal isolation which can lead to substantial costs for remediation, and in worst case scenario negative environmental consequences and accidents. A study from 2011 reports well integrity issues in around 75 of 406 investigated wells in the Norwegian Continental Shelf [2]. A study by Davies et al. [3] revealed that depending on the dataset under examination, between 1.9% to 75% of the wells were identified to have integrity problems. The significant variation in the percentage of problematic wells in each dataset was attributed to differences in the total number of wells, their age, and their configurations. This wide range of well integrity issues and SCP are not only rooted from cement. For instance, corrosion of casing and tubing, poor thread connections, etc., are also root causes of the problem. Research conducted on wells in the Gulf of Mexico showed that approximately 33% of the 6650 wells experiencing well integrity issues were associated with cement failure. In the downhole environment, numerous factors contribute to the degradation of the cement sheath quality, including corrosive conditions [4], fluctuations in thermal and mechanical stresses [5, 6], tectonic and overburden stresses [7, 8], mud-cement interaction [9, 10], and pressure cycling resulting from operations like multi-stage fracturing [11].

1.2 Geopolymer as an Alternative Material

OPC has been dominant well barrier material for primary cementing, and plug and abandonment (P&A) due to global availability, well-established chemistry and reliability [12]. Despite these advantages, there are several drawbacks linked to OPC. These are shrinkage, durability issues, instability in HPHT and corrosive environments, low ductility, and incompatibility with OBDF [13-17]. Most significantly, high emission of CO_2 is associated with the production process of OPC, which can account for as much as 5-8% of global CO_2 emissions [18]. Indeed, it makes sense to seek alternative materials to address the issues. Geopolymers is among the materials considered as alternatives named after Davidovits [19]. This alumino-silicate inorganic polymer is classified as cementitious materials when a liquid alkaline activator is combined with aluminosilicate sources like fly ash, blast-furnace slag, rice husk ash, metakaolin, red mud, and natural pozzolans [20-22]. The alkali activator commonly used are sodium and potassium hydroxide, sodium and potassium silicate, sodium carbonate, or a combination of these. Various sources of aluminosilicate yield different chemical structures in geopolymers, resulting in materials with diverse mechanical and chemical properties. Figure 2 shows a simplified general mechanism of reactions involved in geopolymerization [22]. Dissolution involves hydrolysis of Al-O-Si bonds and OH^- ions in high pH medium attacking the Si-O-Si bonds. This results in releasing aluminate and silicate species in the solution that might also contain additional silicate from the alkali activator. The alkaline cations in solution also neutralize the negative charges on $Si\text{-}O^-$, preventing the reversion to Si-O-Si. In highly concentrated solutions, a gel is formed where the oligomers create extensive networks through condensation while releasing H_2O as product. The produced water stays in the open pores and gel micropores [21, 23, 24]. Following gelation, the system undergoes further reorganization, leading to an increase in the connectivity of the gel network. This process ultimately results in the formation of the three-dimensional aluminosilicate network typically associated with geopolymers. The by-product of this reaction is water while in cement hydration water is consumed.

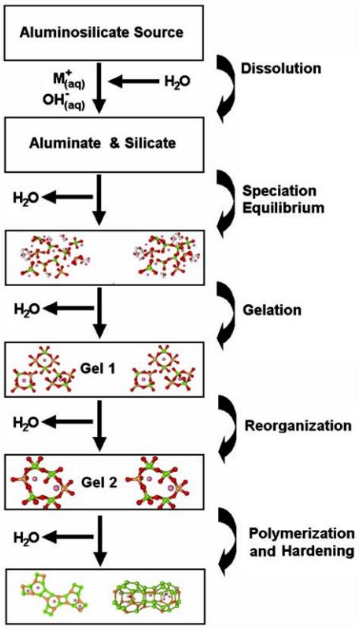

Figure 2 : Conceptual mechanism of geopolymerization [22]

1.3 Mud Displacement

The overall success of the cementing operation and subsequently maximizing annular barrier performance is significantly impacted by the effectiveness of mud displacement. The interaction between cement and drilling fluid, normally nicknamed as mud, in case of incomplete displacement primarily occurs through intermixing, the channelling of cement into the wider side of the annulus, and the presence of residual mud layers on the walls (wet microannuli). In the last case, mud can dehydrate after being in contact with cement for a period resulting in microannuli which provides a path for gas migration [25, 26]. Completely preventing the mixing at the interface of two in-contact fluids being circulated in drill pipe, which can be solved by using wiper plugs) and up to the annulus is almost impossible [27]. Thus, it is important to have well-designed spacer fluid as buffer to separate the incompatible fluids (i.e., cement and mud). Compatibility is not the only criteria for the spacer. Also the density and viscosity must be carefully designed. This ensures that spacer is not channelling in mud column which eventually end up with unwanted contact of cement and mud. Accordingly, design rules have been developed to have effective displacement in laminar flow [28, 29]. For instance, based on ELF (Effective Laminar Theory), displacing fluid must be heavier than displaced fluid by at least 10%, and frictional pressure gradient of displacing fluid be at least 20% greater [29]. Moreover, the shear stress exerted by displacing fluid should surpass the yield stress of displaced fluid. More careful consideration is required for these design methodologies when applied to horizontal and near-horizontal wells due to the restricted flow toward the lower side of the annulus in case of density hierarchy [30]. While the design rules were proven to be useful and contained several physical meanings, fundamental understanding was limited, and the recommendations tended to be conservative. Later, a model called 2D-gap averaged (2DGA) was developed, leading to the availability of a widely used two-dimensional mud displacement simulator for field applications [31, 32].

Beside fluid properties that was mentioned before, there are other factors influencing the success rate of displacement such as flow rate, geometry and inclination of the wellbore, spacer contact time, centralization and casing movement [33]. A common practice to prevent channelling is to use centralizers on the casing. Higher eccentricity can cause spacer or cement to follow the path of least resistance, leaving pockets of mud on the narrower side (Figure 3). Indeed, one of the several reasons of cement failure in Macondo incident was inadequate amount of centralizers on liners [34].

A static layer of mud can form on the casing and formation walls if the shear stress created by the displacing fluid at the wall does not exceed the yield stress of the displaced fluid. It has been reported that the ratio between the yield stress of the displaced and displacing fluids, and Bingham number are determining factors in whether a static mud layer will form on the walls or not [35]. Formation of mud filtercake on the walls represents an extreme case of a static mud layer, particularly when the yield stress is substantial. Consequently, simply increasing the shear stress is often insufficient to remove it and alternative mechanism such as mechanical (e.g., scraping and brushing), abrasion and physico-chemical methods are needed. According to Ravi et al. [36], better hole cleaning was achieved by pumping spacer fluid containing particles compared to water, despite both exerting the same shear stress at the walls. Abrasion mechanism of the filter cake by the particles from displacing fluid is less known. Shear rates involve vorticity, creating complex flow patterns with rotating particles at the microscale. Upon contact of the particle-containing fluid with mud cake, these rotating particles diffuse across the interface, and break some part of it [37]. An example of physico-chemical method is adding surfactants which aid in removing the static oil-based drilling fluid layer from the wall by reducing interfacial tension. The time that spacer is in contact with mud layer is also important. An experimental study showed that the efficiency of mud cake removal can increase from 45% to 74% if the duration of washing contact is extended from 4 minutes to 10 minutes [38].

When it comes to spacer design for minimizing the contamination of cement by drilling fluid, an optimized design should possess: (i) a tuneable viscosity profile and density to aid mud displacement under various conditions, (ii) components ensuring compatibility with mud and cement during and after pumping, and (iii) appropriate surfactants to dissolve oil-based mud layers on walls and enhance cement bonding.

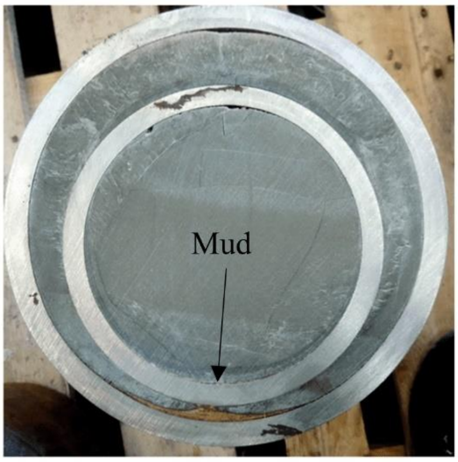

Figure 3 : Channeling of the cement toward the wide side of annuli, leaving a pocket of mud in narrow side that provides leakage path [39]

1.4 Mud Contamination

Previously, we discussed effective practices for improving mud displacement to prevent cement contamination. Now, we explore the consequences of inadequate mud removal on cement properties and its effectiveness as a barrier material. We can categorize these negative effects into two groups: those that adversely affect the cement job during placement and those that create problem after the cement setting process. The choice of drilling fluid significantly influences the extent of contamination. Multiple factors contribute to drilling fluid selection, including temperature and pressure conditions, environmental concerns, well trajectory, shale formations, and economic considerations. The following section presents some findings on the impact of different types of drilling fluids on OPC properties.

1.4.1 Liquid-State Properties

The thickening time of cement is a critical property. If it becomes unpredictable and too short, it can result in the cement setting at undesired depths. Conversely, if it is significantly delayed, it can lead to unreasonably high Wait On Cement (WOC) time, resulting in a more costly operation. The brine present in the internal phase of the Oil-based drilling fluid (OBDF) can act as accelerators, reducing the cement thickening time when the internal phase gets broken as result of the contact with cement [17]. On the other hand, the Water-Based Drilling Fluid (WBDF) might increase the thickening time, by increasing the water to cement ratio [40]. Unpredictable impact of drilling fluid-cement interaction on rheological behavior can also be hazardous to cementing job. If the resulting mixture gets excessively viscous, it might be difficult for the bulk cement to displace it, raising the risk of channelling through the wider side of the annuli. Additionally, this viscosity increase can elevate the Equivalent Circulating Density (ECD) due to heightened annular friction pressure, posing a risk of fracturing weak formations. OBDF resulted in increase in viscosity profile of cement specifically at lower temperatures [41, 42]. One possible mechanism suggested is that due to osmotic pressure, the internal phase of OBDF can absorb additional water from the cement, resulting in a reduction of accessible water within the cement matrix [41]. Incorporating the wetting agent in OBDF design resulted in lower plastic viscosity and yield stress of the mixtures by oil wetting of cement grains and increasing the lubricity [17]. The fatty alcohol ether sulfates surfactant proved to be effective in mitigating the negative impact of OBDF on flow behavior of cement

[41]. WBDF reduced viscosity of cement due to extra water becoming available for cement [40, 42].

1.4.2 Solid-State Properties

The drilling fluid contamination can also impair the zonal isolation by influencing the after-setting properties which are essential to prevent leakage of unwanted fluid. Katende et al. [43] reported that 30% OBDF can increase the permeability of class-H cement from roughly 3 to 64 Micro Darcy. Similar trends were observed for the porosity of cement as well. They further noted that the inclusion of OBDF in cement did not trigger any chemical reactions, but it does contribute to the formation of fractures and holes within the cement matrix. The wetting agent also aids in mitigating the deterioration of cement strength caused by OBDF by stabilizing the oil phase within the matrix, leading to smaller cavity diameters [17]. Li et al. [41] reported that contamination with 5% OBDF can reduce the compressive strength of cement by 30% after one day and degradation of cement escalated with higher levels of fluid intermixture. The mechanism of contamination they described involves the encapsulation of cement particles by oil, which hinders hydration resulting in a honeycomb-like structure. A research by Aughenbaugh et al. [44] demonstrated that synthetic-based drilling fluid without any brine content exhibited notably superior performance. This finding strongly suggests that osmotic forces which moves the water available for hydration to the internal phase of OBDF is the primary mechanism responsible for the detrimental effects of contamination. The strength of cement could also be reduced by WBDF, with partially hydrolyzed polyacryl amide (PHPA) polymer drilling fluid having the most significant impact [40]. Cheng et al. [45] suggested that polymers can adsorb onto the surface of cement particles, hindering the hydration process of the cement.

1.4.3 Interface Properties

Insufficient cement bonding at the interfaces with the formation and casing can lead to failure of the cement sheath and inadequate zonal isolation. Drilling fluid layer which is left on the walls due to incomplete mud displacement can impair the sealing function and bonding of barrier material. Studies has been done to evaluate the bonding of cement to surface of formation and casing in presence of drilling fluid. A work by Opedal et al. [46] showed that OBDF causes less contact of cement and formation rock and slightly lower shear bond strength was measured for this type of drilling fluid. They also observed that in rock samples with higher permeability and porosity, the bonding is reduced due to the loss of drilling fluid filtrate, leading to the formation of a thick layer. The shear bonding strength of cement to casing surface can be reduced to half of its original value in presence of OBDF due to wettability alteration [47].

2. Scope and Objectives

The main objective is to assess the effects of drilling fluid contamination on the properties of granite-based geopolymer at elevated temperature. Additionally, this study aims to develop a spacer fluid that is compatible with the geopolymers while maintaining the necessary characteristics for effective spacer performance. The sub-objectives are as follows:

- Understanding the mechanisms that are involved when contamination happens.
- Understanding the changes in the structure and morphology of the geopolymer after contamination.
- Designing a spacer fluid that has an ability to efficiently displace the drilling fluid in the well and also be compatible with both drilling fluid and the geopolymer as a cementitious material.

This project can be divided into three steps that were followed to meet the objectives (Figure 4):

Step I: Impact of different ratios of OBDF and WBDF contamination on rheological behavior and mechanical properties of geopolymer were investigated. Additionally, analyses were performed to understand the changes in microstructure and morphology of the geopolymer after contamination.

Step II: After understanding the adverse impact of drilling fluids on geopolymer performance, the focus was to design a spacer that have acceptable compatibility with the same geopolymer. The design process consisted of tuning the viscosity and density to improve the displacement process and optimizing the surfactant content to remove the drilling fluid from the casing and alter the wettability of the casing. Compatibility studies were also performed for geopolymer/designed spacer/drilling fluid.

Step III: Important factors involved in proper placement of the geopolymer in annulus space of upper sections of the well were investigated by performing displacement simulation in surface and intermediate casing.

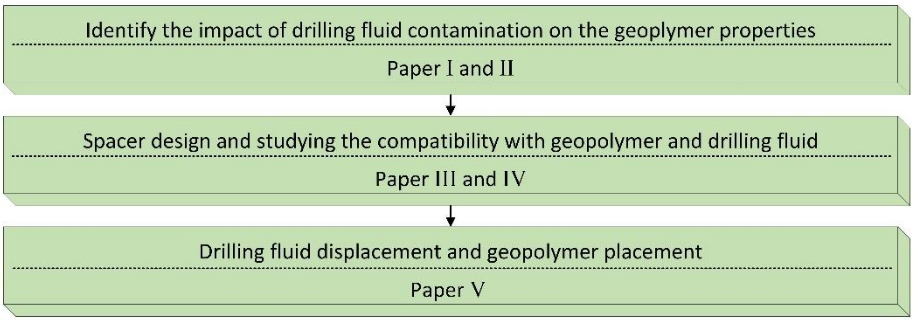

Figure 4 : Steps followed for fulfillment of the research objectives

3. Materials and Mix Design

3.1 Granite

Granite served as the base material for producing the geopolymer discussed in this work. Granite, a prevalent rock type on Earth, is classified as an igneous rock, displaying notable variations in its characteristics and mineral composition based on its environmental conditions. Its primary feature lies in the presence of mineral crystals, incorporating a mix of quartz, feldspar, mica, hornblendes, albite, and pyroxene. The granite in this work was sourced from Sandnes, Norway. The chemical composition of the granite as the main component of solid precursor should be detected. Table 1 shows the granite composition determined by X-ray fluorescence (XRF). It can be noted that granite is rich in Si and Al; however, in crystal forms. This granite has around 15% amorphous content and mainly acts as nucleation site

Table 1: Chemical composition of the solid precursors determined using XRD

Chemical composition (wt.%)	Granite	GGBFS	Microsilica
SiO_2	73.44	35.78	95.50
Al_2O_3	13.33	12.72	0.70
Fe_2O_3	2.06	0.18	0.30
MgO	0.44	12.77	0.50
CaO	1.12	33.74	0.40
Na_2O	3.12	0.55	0.40
K_2O	5.11	0.82	1.00
TiO_2	0.23	2.23	0.00
MnO	0.04	0.58	0.00
LOI	0.90	0.30	2.00

Analysing the X-ray diffraction (XRD) pattern for granite and employing peak fitting analyses (depicted in Figure 5), it becomes apparent that various phases, including quartz, albite, microcline, and biotite are identifiable.

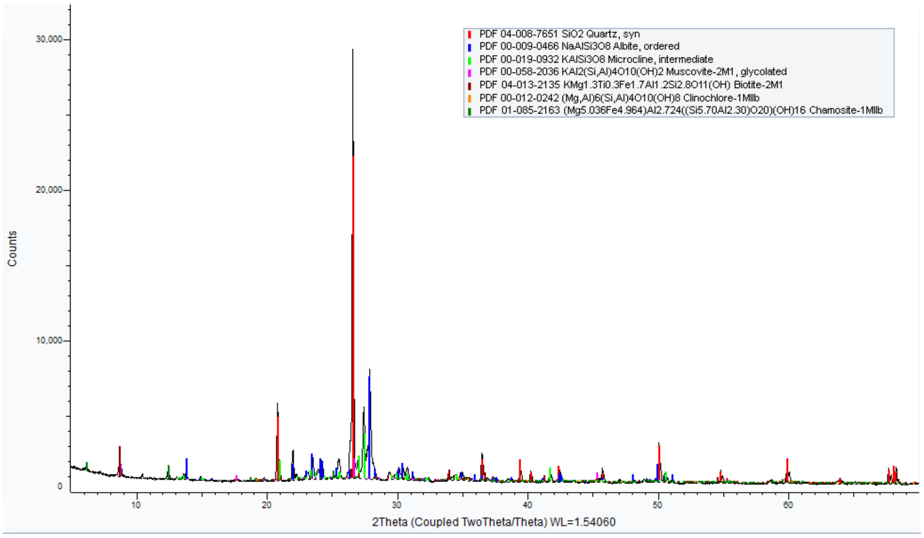

Figure 5 : XRD pattern of granite

Rietveld refinement was used for quantitative phase analysis and weight percent of each mineral is presented in Table 2. It can be observed that quartz is the dominant phase followed by microcline and albite.

Table 2: Quantitative analysis of granite phases using XRD Rietveld refinement

Phase	Wt%	Group
Quartz	30.383	Quartz
Microcline	26.961	Feldspar
Albite	17.284	Feldspar
Clinochlore	7.737	Chlorite
Oligoclase	5.125	Plagioclase
Muscovite	4.899	Muscovite
Chamosite	4.072	Chlorite
Biotite	3.539	Biotite

Morphology of the granite was investigated through scanning electron microscopy (SEM), as shown in Figure 6. Particles of granite exhibit a rough surface and possess an angular morphology.

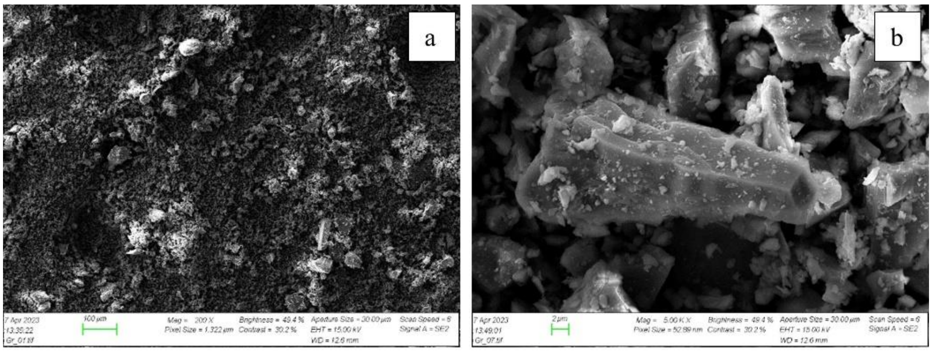

Figure 6 : SEM images of granite (a) 200X magnitude (b) 5K X magnitude

3.2 Ground Granulated Blast-Furnace Slag (GGBFS)

GGBFS which is a by-product of metal processing was incorporated to enhance the early strength development of the granite-based geopolymer and hardening spacer. Given its amorphous nature and the presence of calcium-containing elements, GGBFS serves as a strength development agent, helping the formation of interconnected phases of hydrates that reinforce the geopolymer matrix by bridging the gaps between unreacted particles [48-50]. The impact of various calcium silicate on geopolymerization rate mainly depends on crystallinity of the source [51]. In general, the inclusion of calcium has a positive impact on the mechanical properties of the geopolymeric binder. GGBFS in this work was sourced from Sweden.

The reactivity of GGBFS depends primarily on two key properties: its chemical composition and its amorphous content. Higher ratios of Ca/SiO_2 or $(CaO+MgO+Al_2O_3)/SiO_2$ leads to higher reactivity of GGBFS [52]. Table 1 shows the chemical composition of GGBFS used in this study. The GGBFS contains minor crystalline content (on average, 5 to 10% of slag [53]); therefore, no clear XRD reflections was observed. Morphology of the GGBFS is also shown in Figure 7, indicating irregular and rough particles.

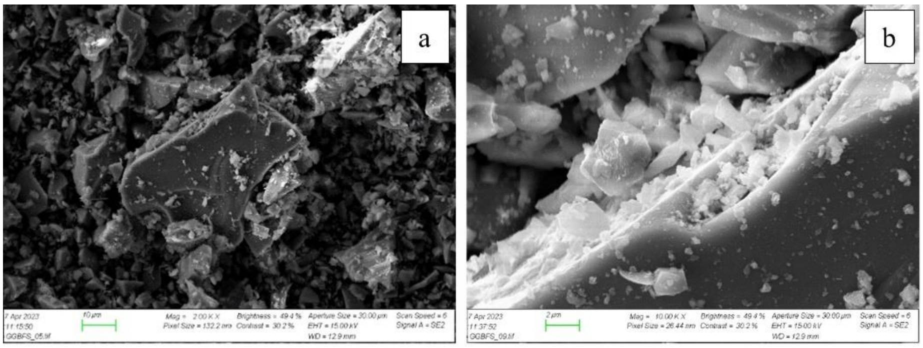

Figure 7 : SEM images of GGBFS (a) 2K X magnitude (b) 10K X magnitude

3.3 Microsilica

To achieve a balanced Si/Al ratio in the geopolymer mix design, highly reactive microsilica (from Elkem Norway) with a purity of 95.5 wt% was employed. Detailed chemical composition is shown in Table 1. This reactive pozzolan has the benefit of reducing permeability and enhancing strength development and stability. It can also reduce fluid-loss by optimizing particle packing [54]. In cement, microsilica can prevent strength retrogression in HPHT wells (temperature higher than 110 ℃). The microsilica used in this study has ultrafine and perfectly spherical SiO2 particles as shown in SEM image (Figure 8). Same as the GGBFS, XRD pattern of the microsilica did not show clear trend since it is highly amorphous.

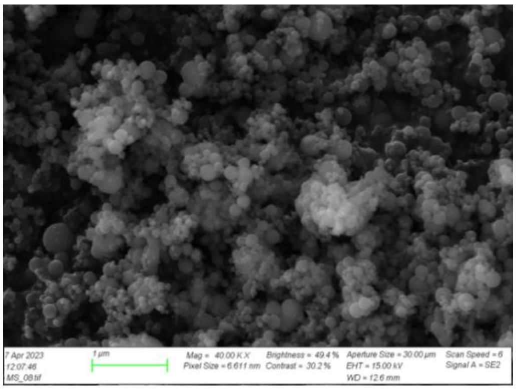

Figure 8 : SEM image of microsilica at 40K X magnitude

3.4 Mix Design of Geopolymer

The geopolymer was formulated by combining a liquid phase (hardener) with a solid phase (precursor). Solid phase was combination of granite, GGBFS, and microsilica. A hardener, consisting of a potassium silicate solution with a molar ratio of 2.49, was utilized. The liquid-to-solid ratio for this specific mix design was set at 0.51 by mass. Mix design of the geopolymer for contamination study is shown in Table 3. This specific mix design was developed by Chamssine [55]. Chemical admixtures were incorporated into the slurry in the liquid form by first dissolving in water.

Table 3 : Mix design of geopolymer used in this study (W201)

Component of the Geopolymer	Description	Weight (g)
Solid precursors	Granite	700
	Ground granulated blast furnace slag (GGBFS)	
	Microsilica	
Liquid activator	Potassium silicate solution	311
Retarder and strength booster	Zinc salts	6
	Potassium salt	1.5
	Water	47
Density (s.g.)	1.98	-

3.5 Mix Design of Drilling Fluid

Two different mix designs of drilling fluid (OBDF, WBDF) were chosen by consulting a service company and were used to contaminate the geopolymer. Table 4 and Table 5 show the mix design, mixing time, and function of each component for WBDF and OBDF respectively. The OBDF had an oil/water ratio of 74/26.

Table 4 : Mix design of lab formulated WBDF

Ingredients	Concentration by Weights (g)	Mixing time (min)	Function
Water	340	-	Base fluid
KCl	40	5	Shale inhibitior
Na_2CO_3	0.52	5	Treatment
PAC-ELV	4	15	Viscosity and Fluid loss
Starch	1.75	10	Fluid loss
Xanthan gum	1	10	Viscosity
Ethylene glycol	14.5	5	Antifreeze
Barite	127	25	Weighting agent
Bentonite	10	10	Solid particles
Density (s.g.)	1.27	-	-

Table 5 : Mix design of lab formulated OBDF

Ingredients	Concentration by Weights (g)	Mixing time (min)	Function
Water	75	-	Internal phase
$CaCl_2$	16.6	5	Wellbore stability
$Ca(OH)_2$	2	5	Emulsion stablizer
Mineral oil	174	15	Base fluid
Emulsifier	11.9	10	Primary and Secondary
Organophilic clay	8	10	viscosity
Barite	138	25	Weighting agent
Density (s.g.)	1.16	-	-

3.6 Mix Design of Spacer

The base spacer mix design that was used for further development of hardening fluid is shown in Table 6.

Table 6 : Mix design of base hardening spacer

Component	Mass fraction	Mixing time (min)	Description
Water	46.95	-	Base fluid
NaCl	1.41	5	Strength booster
Na_2CO_3	0.94	5	
GGBFS	30.36	10	Solid precursor
Granite	15.65	10	
KOH solution(12M)	1.56	5	Activator
Potassium silicate solution	3.13	5	
Density (s.g.)	1.52	-	-

3.7 Geopolymer, Drilling Fluid, and Spacer Preparation

The geopolymer slurries were prepared using a commercial Constant Speed Blender (OFITE Model 20), following the API 10B-2 standard [56]. Chemical admixtures pre-mixed with distilled water were introduced into the alkali solution and blended for 10 seconds at 4000 RPM. Subsequently, the solid precursor, rich in aluminosilicate, was introduced to the liquid hardener within a 15-second duration at 4000 rpm. Subsequently, the slurry underwent further mixing for 35 seconds at 12000 rpm. Instantly after that, various volumes of drilling fluids, and spacer (5, 10, 15 and 20% by volume of geopolymer) were added to the geopolymer slurry and mixed for 10 seconds. The neat and contaminated slurries were then conditioned at a Bottom-Hole Circulating Temperature (BHCT) of 50°C in an atmospheric consistometer before the main tests. This BHCT best describes the temperature that geopolymer experiences in intermediate and production casing while being pumped.. In the context of well cement testing, 'conditioning' is a term referring to the simulation of conditions that the slurry experiences during pumping into the downhole. Drilling fluids were prepared using a Silverson L4RT-A high-speed mixer and subsequently hot-rolled for 16 hours at a temperature of 90°C. Spacer fluids were mixed with Hei-TORQUE mixer.

4. Methods

4.1 Drilling Fluid Contamination Methodologies

The testing methodology employed for the drilling fluid contamination study throughout this project is illustrated in Figure 9. Firstly, drilling fluids were prepared in the lab. Thereafter, the neat geopolymer was contaminated with different volume of prepared drilling fluid. In first step, rheological behavior of contaminated slurries was studied. The contaminated geopolymers were also cured under elevated temperature and pressure up to 7 days and mechanical and microstructural analysis were performed on the cured samples. The majority of properties were assessed following API Recommended Procedure 10B-2 [56] originally established for well cements, but this time used in evaluating the performance of the geopolymer after contamination.

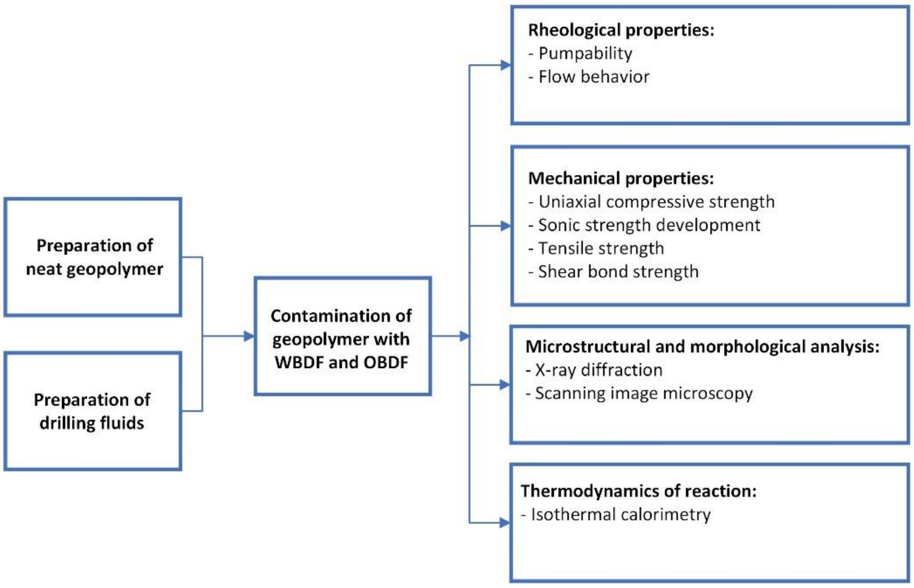

Figure 9 : Testing methodology for drilling fluid contamination of geopolymer

4.1.1 Pumpability

The thickening time of geopolymer slurries was monitored using a pressurized consistometer in accordance with API RP 10-B2 [56]. The measurement was conducted at 50 °C BHCT and 13.8 MPa pressure. In oil well cementing operations, as per the operator's criteria, a value of 30-40 BC is considered a threshold beyond which the slurry is risky of being pumped since it is too thick.

4.1.2 Flow Curve

Flow curve of the slurries was measured using rotational viscometer which is available tool in the field. Shear stress readings (lb/100 ft^2) were recorded in ascending order from 3 to 300 RPM (5.11 to 511 1/s), followed by a ramp-down from 300 to 3 RPM. For drilling fluids, the upper limit of shear rate was 600 RPM (1022 1/s) [56]. The tests were performed at 50 °C BHCT and atmospheric pressure unless otherwise specified.

For further investigation of flow behavior, a scientific rheometer was used that has the advantage of the higher resolution of measurements at extremely lower shear rates. The test program had pre-shear, rest, ramp-up and ramp-down intervals. Ramp-up interval consist of shear stress measurements (21 measurement points and logarithmic duration from 5 to 50 s) from 0.01 to 1000 s^{-1}. Ramp-down had the same profile but in reverse order. It is worth mentioning that slurries were conditioned before measurements.

4.1.3 Oscillatory Shear Measurement

This test was done to characterize the viscoelastic behavior of the slurries. The shear strain amplitude was varied from 0.01 to 100 % while keeping the frequency constant at 10 rad/s. Mainly, two geometries of concentric cylinder and plate-plate were used for this test. Concentric cylinder geometry had bob and cup radius of 13.327 mm and 14.455 mm and gap length of 40.032 mm. Plate-plate geometry had a radius of 21.949 mm and a gap size of 1 mm.

4.1.4 Density

The density of slurries was measured at ambient temperature and elevated pressure by use of pressurized mud balance.

4.1.5 Isothermal Calorimeter

TAM isothermal calorimeter was utilized to monitor heat evolution of geopolymer samples. Immediately after mixing the geopolymer, 5 g of slurry was poured into a plastic ampoule and afterward, it was transferred into the calorimeter. The heat flow rate was measured for up to seven days at 70 ℃.

4.1.6 Uniaxial Compressive Strength (UCS)

Geopolymer samples were poured into cylindrical molds and they were cured in autoclaves under 13.8 MPa and 70℃ BHST for one, three, and seven days. For testing, both ends of hardened specimens were flattened. Specimens followed 1 < slenderness ratio (l/d) < 2. Uniaxial compressive strength (UCS) tests were measured using a hydraulic press machine with a loading rate of 30 kN/min. UCS is defined as the maximum axial compressive stress that a sample of material can endure before reaching failure. It is alternatively referred to as the unconfined compressive strength since the confining stress is set to zero in this testing scenario. UCS can be determined as follows:

$$\sigma = \frac{F}{A} \tag{1}$$

where F is the maximum axial load (N) and A is the sample surface area (mm^2).

4.1.7 Indirect Tensile Strength(Brazilian Test)

For this test, circular disc samples with thickness-to-diameter ratio between 0.5 and 0.6 were used. These specimens were placed between two curved jaws (Figure 10) and a loading rate of 3 kN/min (in accordance with ASTM [57]) was applied. The tensile strength, determined using the Brazilian method for curved platens, can be calculated as follows:

$$\text{Tensile strength } (\mathrm{N/mm^2}) = 1.272\,\frac{\mathrm{F}}{\pi \mathrm{tD}} \qquad (2)$$

where F is the maximum applied force when the cracks propagate through the sample (N), D is the diameter of the sample (mm), t is thickness of sample (mm).

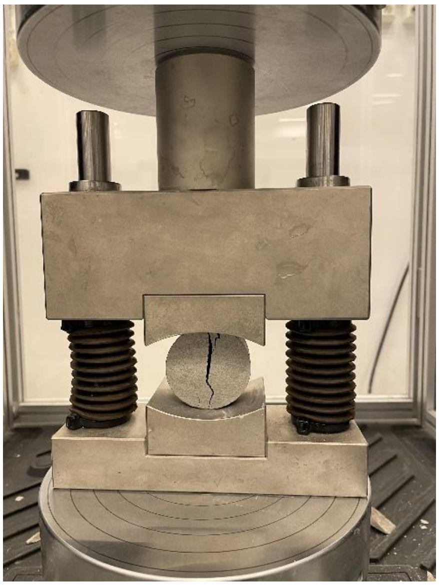

Figure 10 : Schematic of Brazilian test apparatus for measuring tensile strength

4.1.8 Sonic Strength Development-Nondestructive

To assess the early strength of the geopolymer in a nondestructive way, an Ultrasonic Cement Analyser (UCA) was employed. The measurement was conducted at 70 °C and 13.8 MPa to replicate downhole conditions. The ultrasonic cement analyser monitors the transit time of ultrasonic energy passing through a cementitious sample as it hardens. Then, an empirical correlation is used to estimate the compressive strength. The built-in UCA correlation is derived for OPC based materials. Thus, custom correlation for geopolymer was derived by fitting polynomial equations to transit time vs destructive compressive strength (UCS) data measured after 1, 3, and 7 days.

4.1.9 Shear Bond Strength

This test evaluates the bonding of well barrier material to the casing. Shear bond strength is the maximum force which initiates the movement of casing steel at the interface (with cement/geopolymer). It was measured by performing push-out test. Firstly, the geopolymer sample was poured in a pipe and cured for seven days at 70°C BHST and 3.45 MPa pressure in autoclave filled with water. Two pipes with an inner diameter of 110 mm were utilized for the experiment, one exhibiting a rusty inner surface and the other covered with OBDF (Figure 11). After curing, MTS hydraulic press was utilized to apply load and push out the specimens with loading rate of 50 N/s. The shear bond strength can then be determined with:

$$\tau = \frac{F_{max}}{A} \tag{3}$$

where F_{max} (N) is the maximum load when debonding happens and A (mm^2)is the geopolymer-pipe area of contact.

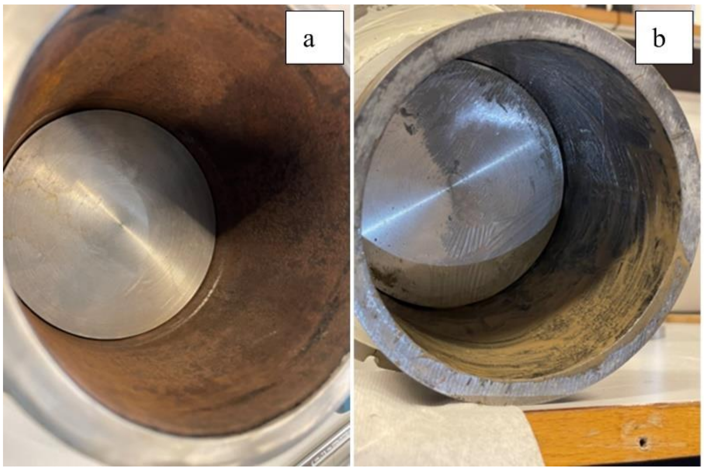

Figure 11 : Steel pipes used for shear bond strength measurement. (a) rusty surface (b) covered with OBDF

4.1.10 Triaxial test

Triaxial test was conducted in accordance with the recommended practice for assessing the mechanical behavior of well cement (API TR 10TR7 [58]). Axial stress was applied by a load piston and radial stress was exerted by oil pressure in the chamber. Radial and axial strain was monitored by extensometer and linear variable differential transformer respectively. The test was performed at 70℃ and 13.8 MPa confining pressure. First, to reach the confining pressure, the radial and axial stress were increased simultaneously with a loading rate of 5 MPa/min and allowed to reach equilibrium for 3 hr. Afterward, water was injected into the sample with a constant rate while monitoring the inlet pressure (the outlet pressure was atmospheric). The permeability of the samples were determined using Darcy’s law by measuring the differential pressure. After one week of injecting and monitoring permeability, the axial load was raised with constant rate of 10 MPa/min to allow measurement of compressive strength.

4.1.11 X-Ray Diffraction (XRD)

XRD method was used to provide insights into the mineral composition, crystallography of the material, and the alterations in solid composition that occur after contamination. In X-ray diffraction, a beam of X-rays is directed toward a sample, and the scattered intensity is measured as a function of the outgoing direction. The angle between the incoming and outgoing beam directions is referred to as 2θ. When the X-ray beam interacts with the three-dimensional arrangement of atoms in a crystal, most of the X-rays undergo destructive interference, cancelling each other out. However, in certain specific directions, the X-ray beams undergo constructive interference. In the case of a sample, composed of sheets of charge separated by a distance d, constructive interference is observed when Bragg's Law is satisfied:

$$\lambda = 2 \times d \times sin\theta \tag{4}$$

In this study, a Bruker-AXS Micro-diffractometer D8 Advance was utilized, featuring a 2θ range of 5-70 degrees with a 0.8 s time/step and a 0.015° step size. Before analysis, samples were manually grounded into a fine powder and dried overnight at 40 °C.

4.1.12 Scanning Electron Microscopy (SEM)

Scanning Electron Microscopy (SEM) technique was employed to investigate the morphology of cured geopolymer and the chemical composition of particles. The analysis was performed using a Supra 35VP ZEISS. All samples were dried in the oven overnight and coated with 10 nm palladium (Pd) or copper (Cu) to reduce the surface charging effect. The samples were cut into small and thin pieces for analysis.

4.2 Spacer Design Methodologies

Figure 12 shows the design process of the spacer for the granite-based geopolymer which consisted of three stages.

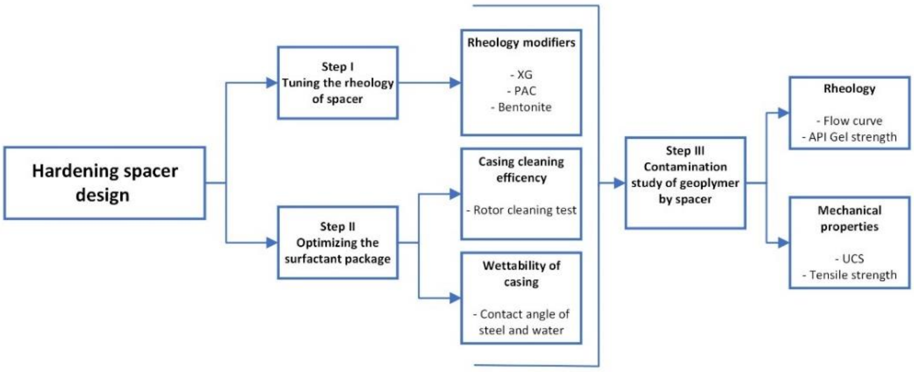

Figure 12 : Test methodology for developing spacer

Stage 1: Selection and optimization of viscosifiers. During this stage, viscosifiers such as xanthan gum, PolyAnionic Cellulose, and bentonite were incorporated with different concentrations (by wt% of water) to the base spacer design (Table 6). This was done to modify the viscosity and have a viscosity hierarchy with both the geopolymer and drilling fluid. For bentonite, a prehydration step in water was carried out, lasting 30 minutes.

Stage 2: Pre-screening and optimization of surfactant content. During the second stage, first, a fixed concentration of three different surfactants were added to spacer and the best one was selected based on performance. Afterward, varying concentrations (by wt% of water) of the best surfactant were introduced to the spacer. The aim was to determine the most effective concentration capable of cleaning the casing surface and reversing its wettability.

Stage 3: Compatibility study of optimized spacer, geopolymer, and drilling fluid. In the last stage, geopolymer and drilling fluid were mixed with the optimized spacer mix design from stages 1 and 2 with the mixture ratio recommended by API (95/5,75/25,50/50,25/75 and 5/95), and rheological properties were measured at 50℃ and atmospheric pressure. The geopolymer was contaminated by 10 and 20% by volume with the optimized spacer and cured for 1 day and 7 days at 70°C and 13.8 MPa. Afterward, the mechanical properties of the cured geopolymer were measured. Mix identification (Id) and concentration of admixtures in each spacer sample are presented in Table 7.

Table 7: Concentration of admixtures used in each design stage to optimize the base spacer fluid along with mix Id

	Mix Id	Admixtures and percentages (wt% of water)
Base spacer	SP	None (Solid/Water=0.98)
Stage 1	SP-XG1	Xanthan gum-0.1%
	SP-XG2	Xanthan gum-0.2%
	SP-XG3	Xanthan gum-0.5 %
	SP-XG4	Xanthan gum-1 %
	SP-PAC1	PolyAnionic Cellulose-0.2%
	SP-PAC2	PolyAnionic Cellulose-0.5%
	SP-PAC3	PolyAnionic Cellulose-1%
	SP-B1	Bentonite-1%
	SP-B2	Bentonite-2%
	SP-B3	Bentonite-4%
	SP-B4	Bentonite-6%
Stage 2	SP-S1	Surfactant package-0.83%
	SP-S2	Surfactant package-1.66 %
	SP-S3	Surfactant package-8.33%
Stage 3	SP-O1	Solid/Water=0.98 Granite/GGBFS=0.52
	SP-O2	Solid/Water=0.98 Granite/GGBFS=0
	SO-O3	Solid/Water=1.96 Granite/GGBFS=0.52

4.2.1 Rotor Cleaning Test

Rotor cleaning test aims to assess the ability of the surfactant or spacer in cleaning the casing surface. In the initial stage, the weight of a clean and dry sleeve was measured (Wcs), and 200 ml of OBDF was poured into the viscometer cup. The viscometer then started rotation at 100 (51.1 s^{-1}) RPM for 5 minutes. The weight of the sleeve covered with OBDF was measured (Wms). Subsequently, OBDF was replaced with 200 ml of spacer, and the viscometer was rotated at 100 RPM for 10 minutes. A glass beaker filled with 200 ml of water was positioned at the base of the viscometer, and the sleeve was rotated at the same shear rate for 5 minutes. Finally, the weight of the washed sleeve was measured (Wws), and a photo of the viscometer sleeve was taken, with any remaining mud on the surface noted. The cleaning efficiency of the spacer was then calculated using the following formula:

$$\text{Cleaning percentage} = \frac{\text{Wms} - \text{Wws}}{\text{Wms} - \text{Wcs}} \times 100\% \qquad (5)$$

4.2.2 Contact Angle

Contact angle measurment assesses the ability of the spacer to promote water-wetting of the surface of the casing. In first step, steel coupon, which represented casing, was dipped in a container filled with OBDF for 10 min. After that, the coupon was dipped in the container filled with spacer and subsequently a mixer was placed inside the container to shear the fluid for 10 min at 100 RPM. Afterward, the coupon was removed from the container and the contact angle of water droplet on the surface was measured. A Kruss drop shape analyser that photographs a sessile drop was used for contact angle measurements.

4.2.3 Electrical Stability Test

The Fann electrical stability tester was employed to assess the capability of surfactant in the spacer design to reverse the water-in-oil (W/O) emulsion. This is achieved by measuring the electrical stability of OBDF while introducing a spacer to it. The electrical stability tester has pair of parallel electrodes that records the maximum voltage that induces coalescence of internal water droplets in the fluid, thereby initiating conduction between the two electrodes.

4.2.4 Displacement of OBDF by Spacer

To replicate fluid displacement in annular space, a simple laboratory setup was designed comprising a tube with dimensions of 278 mm in length, 15 mm of inner diameter, and 23.7 mm of outer diameter (Figure 13). Utilizing a pump, fluids were pumped from storage tanks to the concentric annular tube at a constant rate of 2.33ml^3/s. Initially, the test section was filled with OBDF while ensuring the absence of air bubbles in the system, and afterward the fluid was isolated by closing the valve. Subsequently, the spacer was pumped through a rubber hose connected to the tube's inlet. The test was started by opening the inlet valve, initiating the displacement of OBDF by the spacer. The tube also featured an outlet valve on top, enabling the collection of outlet fluid at various times. The density of the outlet fluid was collected and then measured with an Anton Paar DSA 5000 M densitometer that assisted the assessment of mud displacement. Mud displacement in large scale in the annular space is a complex process. The test methodology used here is simplified with the aim of understanding the role of surfactant in displacement and best works for the fluids that have density contrast.

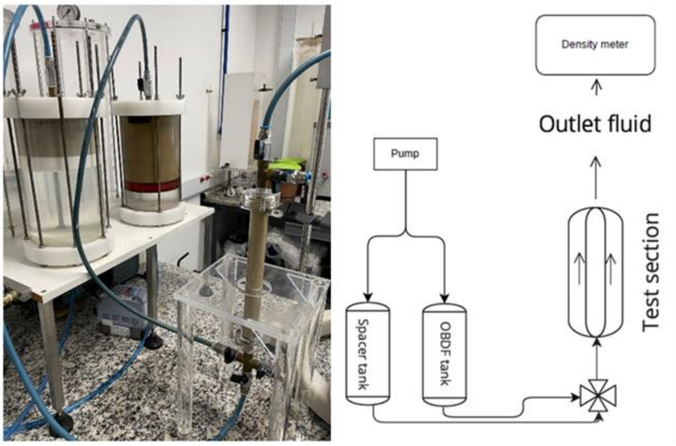

Figure 13: Drilling fluid displacement apparatus (Paper IV)

4.2.5 R-index

ELF design rule for avoiding the fluid channelling suggest that frictional pressure of displacing fluid should be 20% higher than displaced fluid [29, 59]. This frictional pressure hierarchy can be correlated with viscosity hierarchy. The intermixture of fluids (drilling fluid/spacer/geopolymer) should also be taken into account. If the resulting mixture is thicker than the displacing fluid, channelling through the wide side which has less resistance is likely to happen. In cementing practices, R-index is an empirical factor to determine allowable flow behavior of the mixture. Therefore, assessing the compatibility of fluids can be done beforehand in the laboratory. R-index (lb/100ft^2) can be calculated as:

$$R_{@RPM}= \theta_m - \theta_p \tag{6}$$

where θ_m is the highest shear stress (lb/100ft^2) of mixture recorded at given shear rate, and θ_p is the highest shear stress of bulk fluids. θp can be translated to shear stress of displacing fluid since usually it is more viscous). A guideline then is used to determine the compatibility of displaced and displacing fluid (Table 8). For instance, for fluids to be considered as fully compatible, R should be less than zero which means the shear stress of mixture should be smaller than the displacing fluid at the displacement relevant shear rates. The guideline is designed for the measurements taken with V-G meter. Thus, a conversion factor is needed to make it applicable to other types of viscometers.

Table 8 : Guideline for determination of compatibility of fluids during displacement

R-index (lb/100ft2)	Comment
R<0	Compatible
0<R<40	Compatible (Check friction pressure)
41<R<70	Slightly incompatible (test for better formulation)
R>71	Incompatible

5. Results and Discussions

5.1 Impact of Drilling Fluid Contamination on the Performance of Geopolymer

Primary cementing involves replacement of drilling fluid by cementitious material with the aim of providing permanent formation isolation behind the casing. This makes the subject of mud removal of great importance since it has direct connection with the quality of set cement/geopolymer. Mud channelling and residual mud layers on the walls of casing or formation, and mixing/contamination are some of the instance of consequences that poor mud removal can have [12]. Intermixture of drilling fluid with cementitious slurry can impact the flow behavior while pumping into downhole making placement process harder. Thickening time of the neat slurry also can be changed, resulting in acceleration or retardation of reaction. This contamination impact also is extended to after setting by deteriorating the mechanical properties of the slurry which are essential for providing well integrity of the well during production and to isolate a source of inflow for eternity. Consequently, the impact of drilling fluid contamination on geopolymer as an alternative material to OPC needs to be carefully studied before extensive field application.

5.1.1 Pumpability and Thickening Time

Thickening time of neat and contaminated geopolymer were performed at BHCT of 50 °C and 13.8 MPa using HPHT consistometer. Figure 14 shows the consistency curve of neat and contaminated geopolymer with 5% (by volume of geopolymer) OBDF and WBDF. In the following we consider 40 Bc as the maximum consistency value, beyond which the slurry is risky to pump, the neat geopolymer exhibited a pumpability of 5.5 hours. In the case of contamination with 5% OBDF, the pumpability increased to approximately 8 hours, causing a slight retardation impact.

Additionally, the 'right-angle-set' profile of neat geopolymer was also negatively affected with 5% OBDF. The consistency curve of the geopolymer when contaminated with 5% WBDF remained low and flat throughout the entire 8-hour duration of the test. This shows that WBDF contaminated geopolymer did not go through gelation during this period.

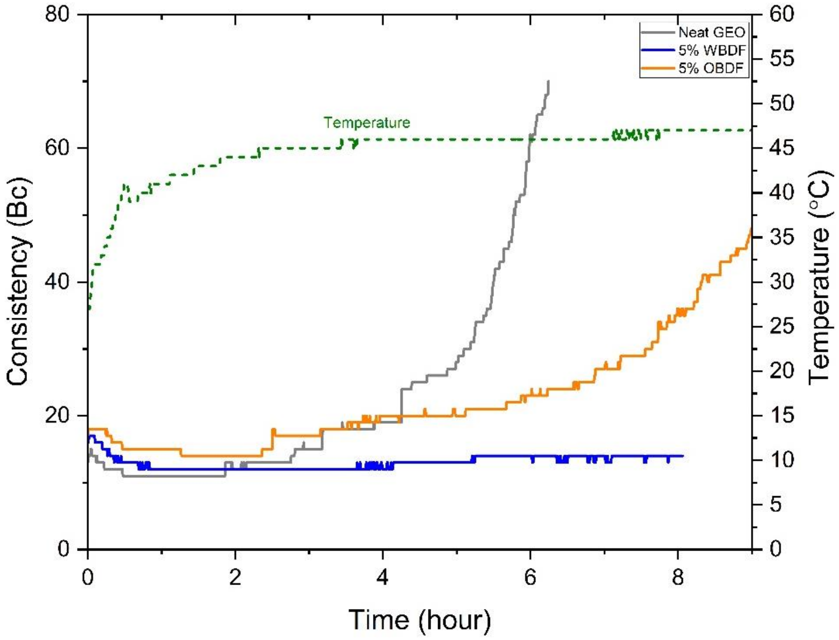

Figure 14 : Thickening time of neat and contaminated geopolymer

5.1.2 Flow Behavior and Viscoelasticity

5.1.2.1 Contamination with WBDF

The undesired comingling of drilling fluid and geopolymer as displacing fluid is possible in the annulus specially if the mud removal program is not designed properly. Therefore, it is crucial to assess the rheological compatibility of these two fluids in the downhole conditions. This is important because the ease of pumping the slurry into the wellbore and placement in the annulus during the cementing job is influenced by mixture rheological properties. Moreover, if the mixture viscosity rises unexpectedly, there is chance of fracturing the formation in open hole.

Geopolymer slurries were contaminated with 5, 10, 15, 20 % (by volume of geopolymer) OBDF and WBDF and flow curve of slurries were measured at 50 °C BHCT and atmospheric pressure. Ramp down shear stress measurement was used for plotting the flow curve. The flow curve containing average of ramp up and ramp down measurements can be found in Paper I. Thus, any conclusion on thixotropy should be made carefully. Figure 15 shows that by increasing the WBDF contamination dosage, the viscosity profile of geopolymer declines. This can be justified by changes in the phase volume (ϕ) of geopolymer after contamination. Geopolymer has higher solid to liquid ratio compared to WBDF. When these two suspensions are mixed, the resulting mixture has fewer particles suspended in the liquid. As a result, particles need to bounce off each other less, leading to reduced resistance or viscosity in the mixture [60].

From flow curve it can be observed that WBDF had shear-thinning behavior for the shear rates ranges tested. Geopolymer exhibited shear-thinning fluid in lower shear rate ranges, and shear stress vs rate relation became linear in higher shear rates. Thus, geopolymer slurry was non-Newtonian fluid. A local peak in shear stress (around 10 1/s shear rate) was observed for geopolymer sample that was diminished by increasing the WBDF contamination concentration. This peak is associated with viscoelasticity and colloidal interaction between the particles of geopolymer slurry [61]. When the stress is below the peak, geopolymer exhibits a gel-like structure, and beyond that point, it demonstrates viscous behavior.

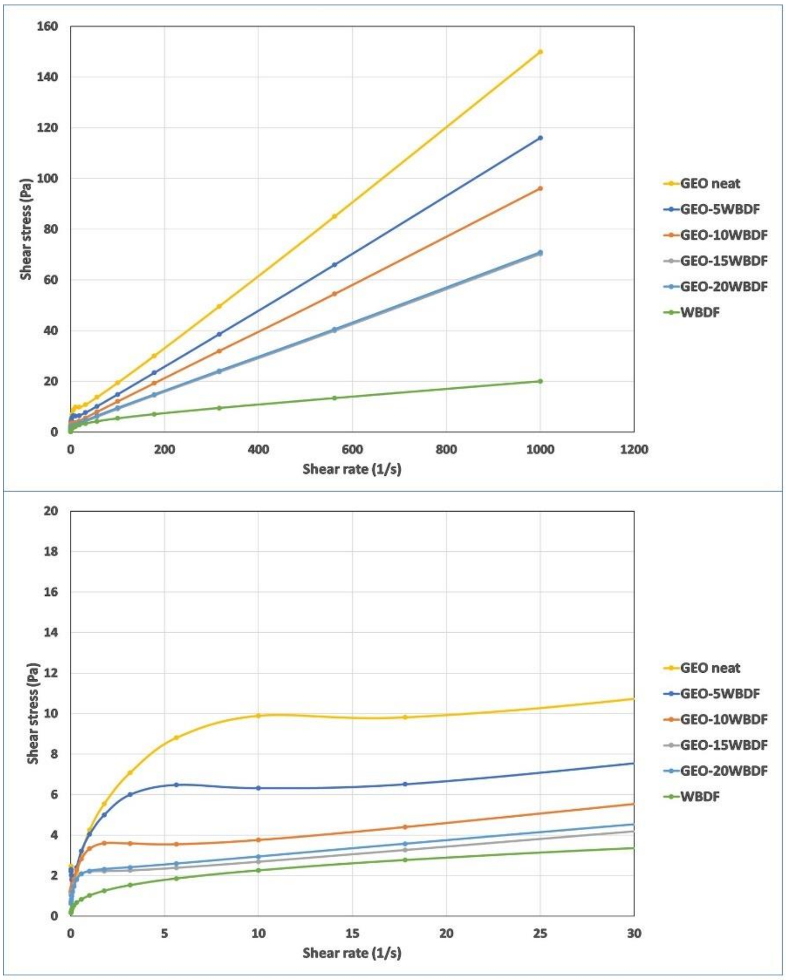

Figure 15 : Flow curve of WBDF contaminated geopolymer (a) full shear rate ranges (b) lower shear rates (Paper I)

Shear stress vs shear rate ramp down measurements were used to calculate the rheological parameters (shown in Table 9). Usually, Bingham Plastic model, Herschel-Bulkley (H-B) model, and Power law model are used to characterize fluid flow of drilling fluids and cements. The Bingham Plastic model is straightforward method that represent a fluid that exhibits yield stress. Due to simplicity and lack of need for complex regression, this method is useful for monitoring and treating the fluids during drilling which is normally only valid at higher shear rates However, it exhibits a significant error when predicting lower shear rate ranges that are more of interest in annular flow [62]. It is expressed as:

$$\tau = \tau_y + \mu_p \dot{\gamma} \tag{7}$$

where τ is the shear stress, τ_y is the Bingham yield stress, μ_p is the plastic viscosity and $\dot{\gamma}$ is the shear rate. The H-B model is a three-parameter viscosity model that applies to shear-dependent fluids that have a yield stress. It can be expressed as:

$$\tau = \tau_y + k\dot{\gamma}^n , \tau > \tau_y \tag{8}$$

where τ_y is the yield stress, k is the consistency index, and n is H-B flow behavior index. k-values of different fluids cannot be compared as the dimension of this parameter depends heavily on n. Thus, we used surplus stress for this purpose which can be found in Paper I. This model can be converted to Power law model assuming no yield stress is present. H-B is reduced to the Bingham model whenever n=1.

Table 9 shows that by increasing the dosage of WBDF contamination, H-B yield stress of geopolymer was reduced and approached to pure WBDF yield stress. Same trend was observed for yield stress obtained with Bingham model. However, the flow behavior index of geopolymer relatively remained constant after contamination with WBDF. Different flow behavior such as shear-thinning, shear-thickening, and Bingham behavior leads to n<1, n>1, and n=1 accordingly. Pure geopolymer and WBDF showed behavior close to Bingham plastic and shear-thinning behavior, respectively.

Table 9 : Rheological parameters of WBDF contaminated geopolymer obtained by curve-fitting method (Paper I)

Model parameters		GEO	GEO-5WBDF	GEO-10WBDF	GEO-15WBDF	GEO-20WBDF	WBDF
Bingham	$\boldsymbol{\tau_y}$(Pa)	5.87	5.56	3.91	2.84	2.30	1.66
	$\boldsymbol{\mu_p}$(Pa.s)	0.15	0.11	0.09	0.07	0.07	0.02
HB	$\boldsymbol{\tau_y}$(Pa)	5.29	5.53	3.90	2.79	2.02	0.52
	$\boldsymbol{k}$(Pa.s^n)	0.27	0.12	0.09	0.08	0.13	0.44
	n	0.90	0.99	1.00	0.98	0.90	0.55

Figure 16 illustrates API gel strength of both neat and WBDF contaminated geopolymer slurries. It indicates that intermixture of geopolymer with WBDF could significantly reduce the 10-s and 10-min gel strength which is an essential property of slurry to suspend the solid particles.

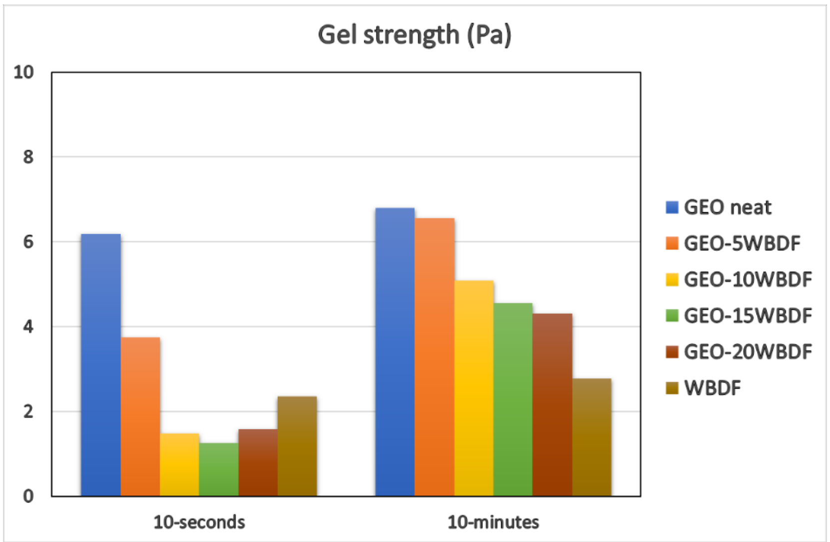

Figure 16 : API gel strength measured for WBDF contaminated geopolymer (Paper I)

Figure 17 shows the storage and loss modulus of geopolymer mixed with WBDF and measured with amplitude sweep test. The storage modulus

(G') reflects the energy stored by a material upon deformation, indicating its elastic behavior, while the loss modulus (G") represents the energy dissipated as internal friction during deformation, indicating its viscous behavior. In Figure 17, the values of G' is higher than G" for the geopolymer, suggesting a gel-like behavior within the linear viscoelastic (LVE) range. Within this range, the material retains its internal structure. However, beyond a strain of approximately 2.5%, irreversible changes occur in the structure as it exits the LVE range where particles within the slurry may begin to leapfrog each other. The stress experienced at this strain level is termed as the static yield stress. At the point where the loss modulus becomes equal to or higher than the storage modulus (known as the flow point), the material's structure undergoes a change significant enough for it to begin flowing. Contamination with WBDF resulted in a decrease in both the storage and loss modulus. After contamination, the termination of the LVE range decreased from 2.5% to below 1% strain, and the corresponding yield stress decreased as contamination increased. The G' and G" profiles of contaminated geopolymer with WBDF exhibited a similar pattern to that of pure geopolymer, indicating compatibility between the two fluids. WBDF appeared to act as a dilutant for the geopolymer slurry. The termination of LVE in WBDF occurred around 6.3% strain, corresponding to a yield stress of 0.217 Pa.

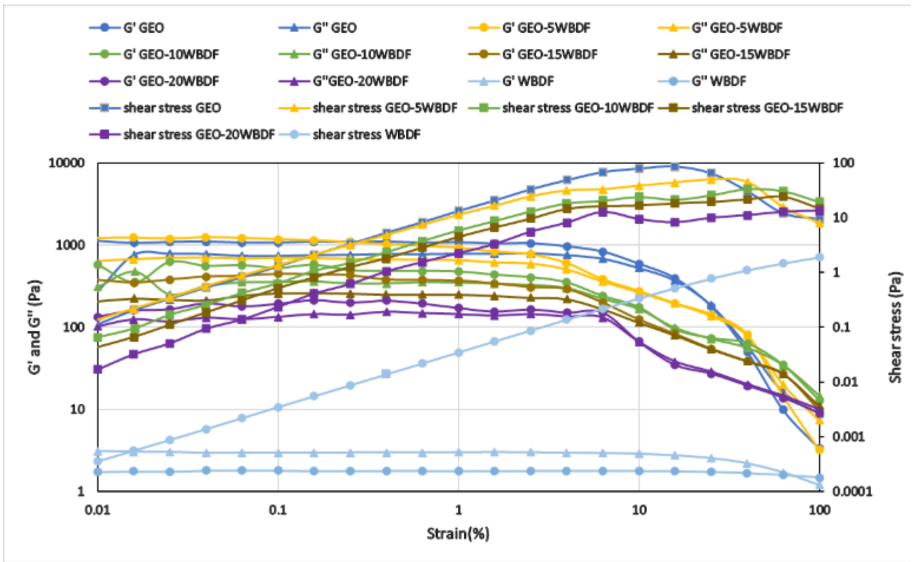

Figure 17 : Storage and loss modulus measured for WBDF contaminated geopolymer slurries (Paper I)

5.1.2.2 Contamination with OBDF

Figure 18 illustrates the flow curve of the geopolymer when contaminated with OBDF. Lower shear stresses were observed at higher shear rates OBDF contaminated geopolymer compared to neat slurry. Conversely, higher shear stresses were noted at lower shear rates. It is speculated that oil droplets transform the water continuous geopolymer into an oil-in-water (O/W) emulsion. Consequently, when at rest or close to rest, it leads to the development of colloidal interactions and gel strength in the fluid [60]. However, at higher shear rates, due to deformability, oil droplets transition from a spherical to an ellipsoidal shape, causing the viscosity of the contaminated slurry to drop below that of the neat geopolymer. This was also manifested in the peak in stress mentioned earlier due to formation of stronger gel.

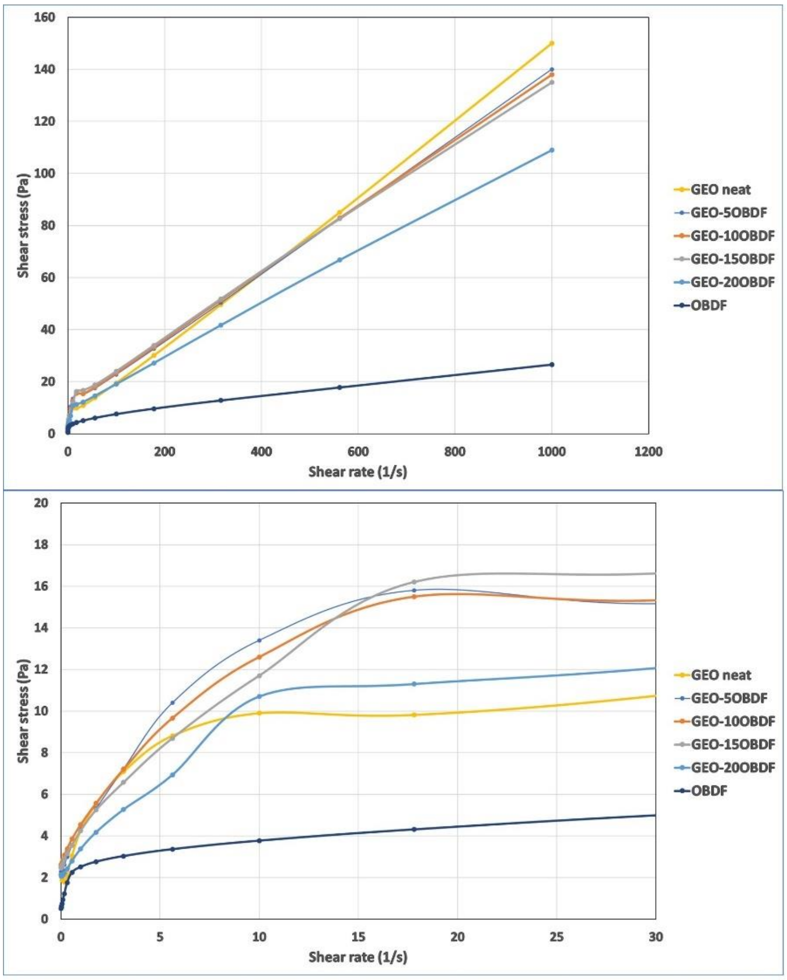

Figure 18 : Flow curve of OBDF contaminated geopolymer (a) full shear rate ranges (b) lower shear rates (Paper I)

Table 10 shows that by increasing the dosage of OBDF contamination, H-B yield stress of geopolymer slightly reduced and the changes were not as extreme as WBDF case. However, yield stress predicted by Bingham model was increased with contamination (Table 10). Additionally, the flow behavior index was reduced with higher content of OBDF that might be due to deformability of oil droplets, leading to more shear thing fluid.

Table 10 : Rheological parameters of OBDF contaminated geopolymer obtained by curve-fitting method (Paper I)

Model parameters		GEO	GEO-5OBDF	GEO-10OBDF	GEO-15OBDF	GEO-20OBDF	OBDF
Bingham	τ_y(Pa)	5.87	6.49	6.57	6.66	5.22	2.35
	μ_p(Pa.s)	0.15	0.14	0.14	0.14	0.12	0.03
HB	τ_y(Pa)	5.29	4.48	4.51	4.03	3.40	0.86
	k(Pa.s^n)	0.27	0.75	0.78	1.05	0.70	0.59
	n	0.90	0.73	0.73	0.68	0.71	0.54

API gel strength of geopolymer slightly increased when it was mixed with OBDF (Figure 19). Although, gel strength is an essential property of slurry to suspend the particle, having excessive gel strength can lead to difficulties in re-starting pumping operation after a period of halt because of operational reasons.

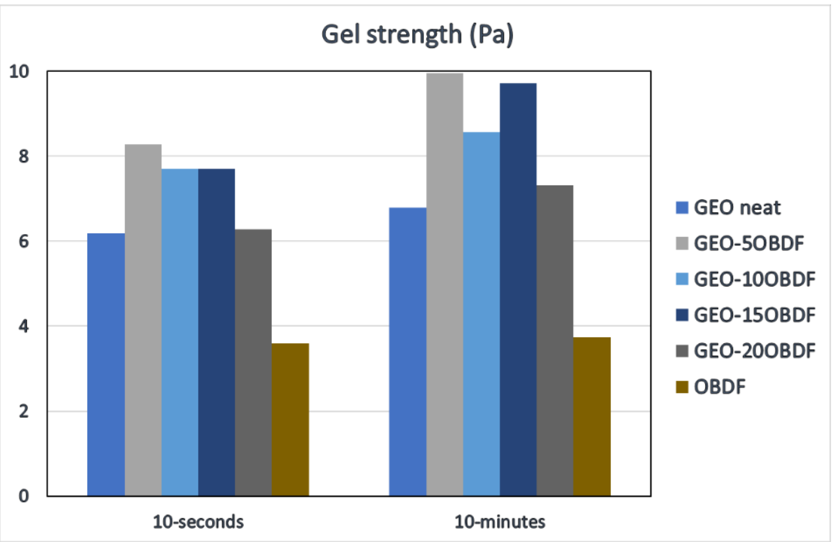

Figure 19 : API gel strength measured for OBDF contaminated geopolymer (Paper I)

When contamination with OBDF occurred, both the storage modulus (G') and loss modulus (G") of the slurry decreased (Figure 20). Furthermore, the difference between these two values increased within the LVE range. Increasing the percentage of OBDF from 5% to higher concentrations did not notably affect the G' and G" values. The contaminated material exited the LVE range around 0.04% strain, and the flow point (G' = G") shifted from 25% to below 10%.

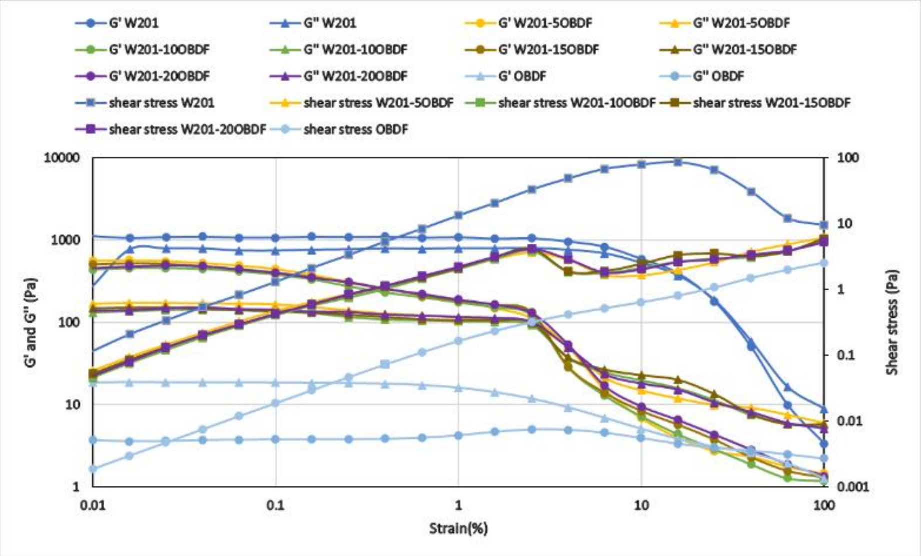

Figure 20 : Storage and loss modulus measured for OBDF contaminated geopolymer slurries (Paper I)

5.1.3 Mechanical Properties and Strength Development

5.1.3.1 Impact of WBDF on Mechanical Properties of Geopolymer

Figure 21 shows the compressive strength of geopolymer after contamination with 5 and 10 % WBDF and curing for 1, 3, and 7 days. The neat geopolymer had approximately 6 MPa strength after 1 day and reached 7 MPa after 7 days. In case of contamination, 5% WBDF reduced the geopolymer strength to less than 4 MPa after 1 day and remained constant after 7 days. When the contamination increased to

10%, the geopolymer was not able to develop strength after 1 day. After 7 days, the 10% contaminated geopolymer exhibited less than 3 MPa UCS. The results implicate that contamination of geopolymer with WBDF during placement should be avoided through a quality mud removal program and a compatible spacer should be pumped in between these two fluids. The tensile strength of neat and contaminated geopolymer with WBDF measured with the Brazilian method is illustrated in Figure 22. The neat sample showed approximately 0.5 MPa tensile strength after 1 and 7 days. The tensile strength dropped to less than 0.4 MPa with 5% WBDF contamination. 10% WBDF contamination led to a geopolymer slurry without any tensile strength after 1 day. After 7 days the strength increased to roughly 0.3 MPa.

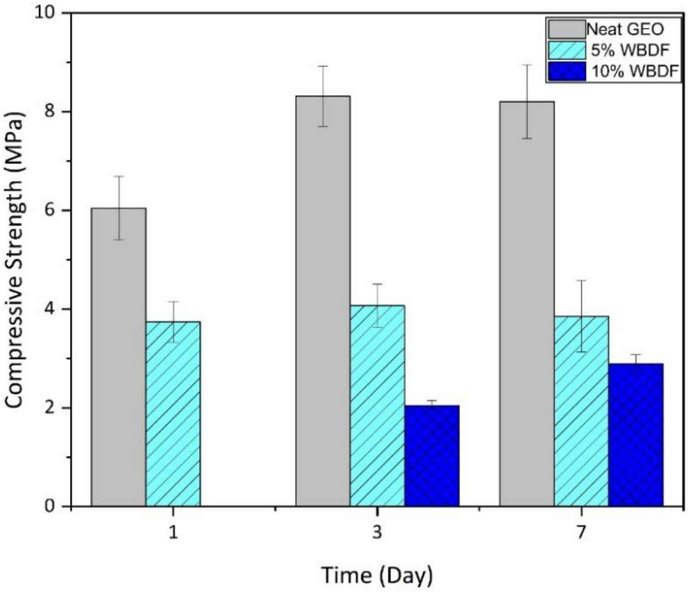

Figure 21 : Compressive strength of WBDF contaminated geopolymer (Paper II)

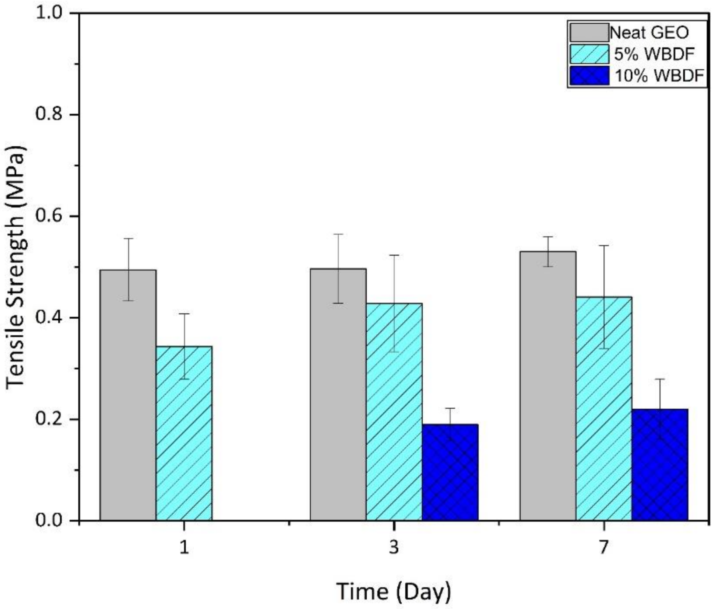

Figure 22 : Tensile strength of WBDF contaminated geopolymer measured with Brazilian method (Paper II)

UCA functions by measuring the transit time of ultrasonic energy through a cementitious sample during its curing process, which can be conducted under high temperature and pressure. The sonic strength was determined through an empirical relationship that was initially established using data from mechanical compressive strength tests and transit time measurements for geopolymer slurries. It is important to note that the compressive strength values obtained from the UCA are specifically applicable to geopolymer under uniaxial loading conditions. The empirical correlation developed, as shown in Table 11, provides a means to estimate the sonic strength development for both neat geopolymers and those contaminated. For the neat geopolymer it took approximately 10 hr to develop strength as illustrated in Figure 23. In cases of contamination with WBDF, the development of strength was observed to be delayed to 20 and 26 hours for mixture dosages of 5 and 10%, respectively. This suggests that an excess WBDF mixture may interfere with the polymerization process in geopolymers. A delayed setting increases WOC which in turn can be costly due to the rig daily rates. The sample contaminated with 10% WBDF exhibited a secondary period of strength increase after five days.

Table 11 : Empirical correlation driven for determination of sonic strength based on transit time and UCS up to 7 days (Paper II)

Sample	**Empirical Correlation**	**R^2**
Neat GEO	$y=0.1441x^2-9.7593x+106.12$	0.9935
5% OBDF	$y=-4.024x^2+103.9x-663.92$	0.9979
10% OBDF	$y=-6.1398x^2+170.44x-1177.7$	0.9831
5% WBDF	$y=-24.097x^2+648.8x-4362.6$	0.9682
10% WBDF	$y=0.4331x^2-14.893x+124.05$	0.7803

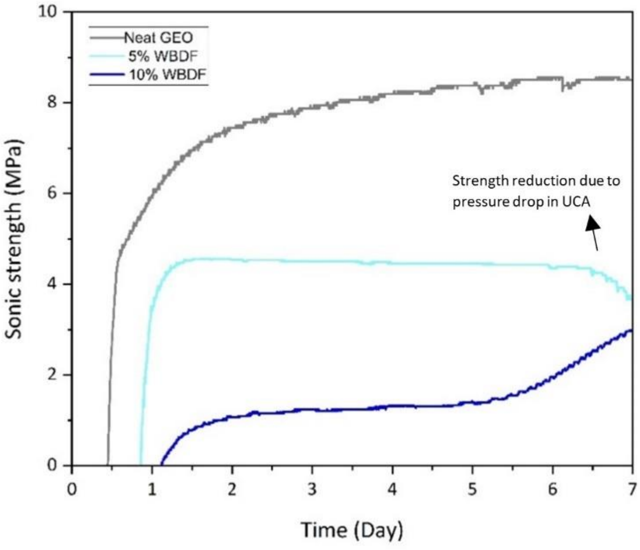

Figure 23 : Sonic strength development of WBDF contaminated geopolymer samples (Paper II)

5.1.3.2 Impact of OBDF on Mechanical Properties of Geopolymer

The UCS of neat and contaminated geopolymer samples with 5 and 10% OBDF are shown in Figure 24. 5% OBDF slightly reduced the strength to less than 6 MPa after 1 day and 6.5 MPa after 7 days. Increasing the contamination dosage to 10%, the UCS after 1 day dropped to 4 MPa which could reach 5 MPa after 7 days. In general, OBDF was less detrimental to the compressive strength of geopolymer compared to WBDF.

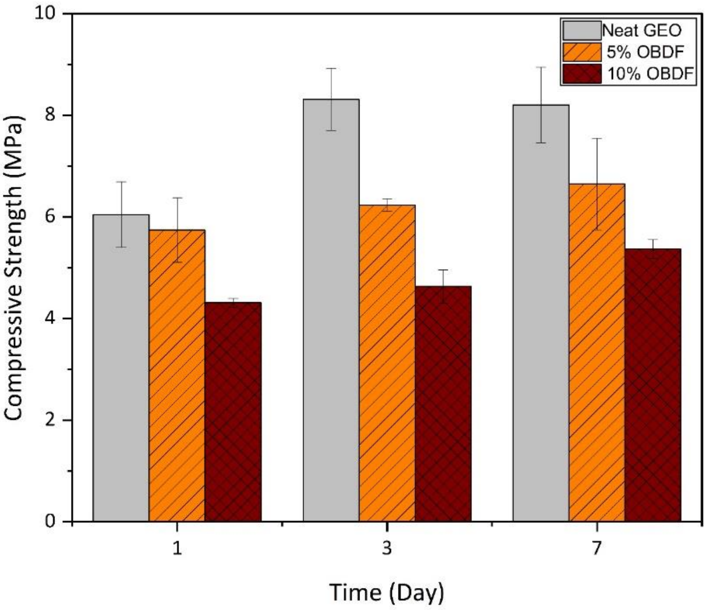

Figure 24 : Compressive strength of OBDF contaminated geopolymer (Paper II)

The tensile strength of the geopolymer after 1 and 7 days was slightly reduced when contaminated with 5% OBDF as shown in Figure 25. The changes were more noticeable in case of 10% OBDF contamination and the tensile strength dropped to less than 0.4 MPa after 1 and 7 days of curing.

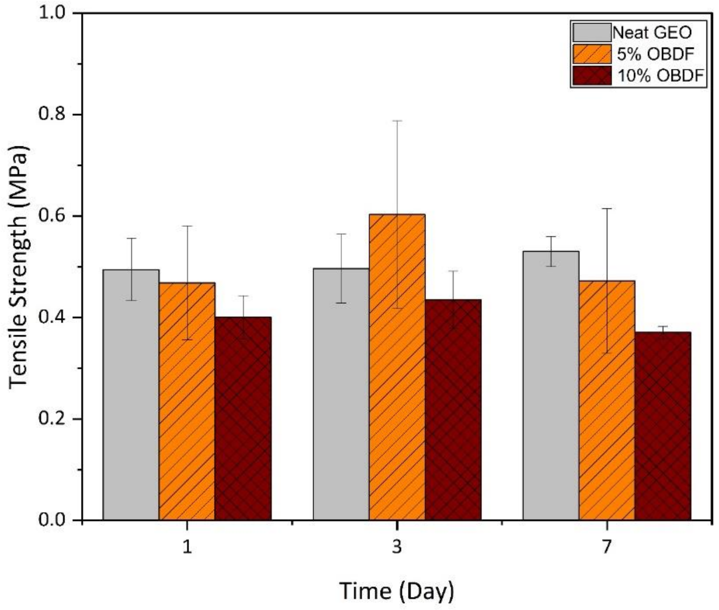

Figure 25 : Tensile strength of OBDF contaminated geopolymer measured with Brazilian method (Paper II)

Sonic strength measurements in Figure 26 show that the contaminated geopolymer (5% OBDF) begins to exhibit strength development after 18 hours which is delayed for 8 hours compared to the neat one. When contamination increased to 10%, the beginning of strength development was after 13 hr that can be translated to 3-hour delay compared to neat geopolymer. This earlier starting point of 10% OBDF strength compared to 5% OBDF could be attributed to statistical variation. However, as later demonstrated with isothermal calorimetry, the UCA results are supported.

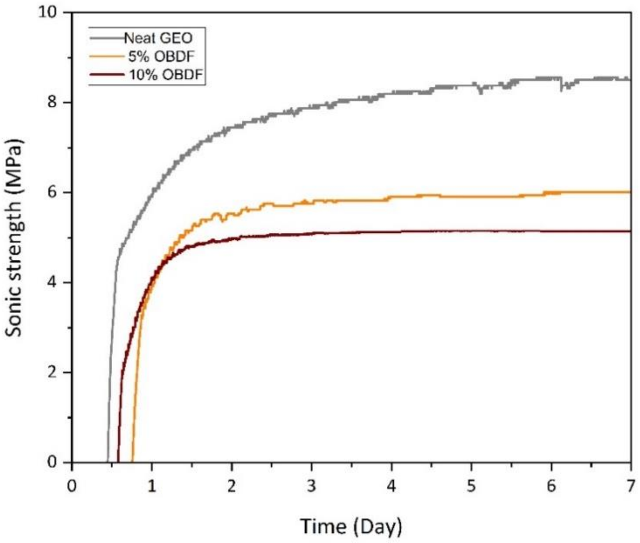

Figure 26 : Sonic strength development of OBDF contaminated geopolymer samples (Paper II)

5.1.4 Triaxial Test — Permeability and Confined Mechanical Properties

The neat and contaminated geopolymer samples were cured at 70℃ BHST and 13.8 MPa for 7 days. Afterward, the water was injected into the samples and inlet pressure was measured which allowed measurement of permeability. Figure 27 shows the permeability of WBDF and OBDF contaminated samples after 7 days of injection and reaching steady flow. 5% OBDF contamination negatively impacted the permeability of geopolymer by increasing it from 0.0823 µD to 0.3516 µD (327% increase). 5% WBDF was more severe and increases the permeability to 0.4954 µD (502% increase). Although the percent increase is high, the value is still very low and should not introduce risk of leakage through the geopolymer matrix. After injection, confined compressive strength (with confining pressure of 2000 psi) and Young’s modulus was also measured with tri-axial test. Figure 27 shows that WBDF contamination at equivalent concentrations resulted in a greater reduction in compressive strength compared to OBDF. However, the Young modulus which is a measure of flexibility of material shows that WBDF contamination leaded to a more ductile material. This is due to the contamination and strength reduction.

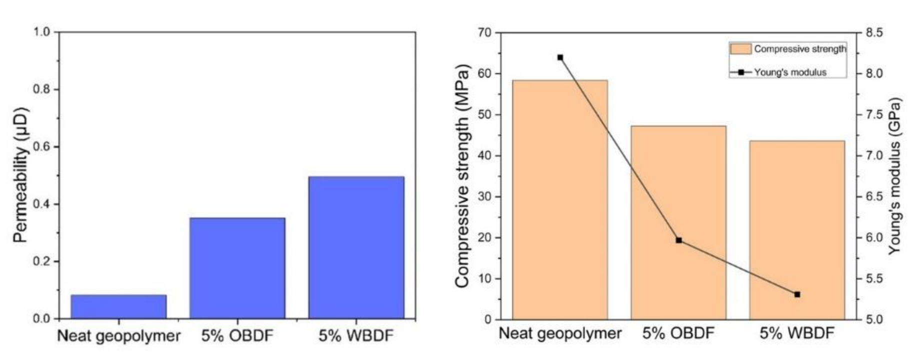

Figure 27: Impact of drilling fluid contamination on (Left) Permeability of geopolymer samples (Right) Confined compressive strength and Young's modulus

5.1.5 *Microstructure and Crystallography of Contaminated Geopolymer*

5.1.5.1 SEM and EDS Analysis

Microstructure of neat and contaminated geopolymer samples were studied by performing SEM analysis on crushed samples after UCS measurements. Figure 28 illustrates the microstructure of 7-day cured geopolymer sample contaminated with 5 and 10% WBDF. For comparison, SEM image of neat geopolymer is also shown in the same figure. The neat geopolymer displayed a compact structure with enhanced bonding between the unreacted particles and the surrounding matrix, directly influencing its mechanical strength. However, when WBDF was introduced into the geopolymer, the amorphous gels became less condensed, resulting in the formation of a cloud-like structure. This structure loosely encapsulated the particles within the surrounding matrix, leading to a significant decrease in the compressive strength of the geopolymer. Unlike the hydration process observed in OPC-based binders, where water is consumed, in geopolymerization, water is produced as by-product during the polycondensation phase. Therefore, the presence of excess water from WBDF in the geopolymer slurry can hinder the geopolymerization process, resulting in the formation of loose and disconnected precipitated gels. Figure 29 illustrates neat and 10% WBDF contaminated geopolymer at higher magnification. Upon closer examination, an increase in unreacted particles and a more porous structure becomes evident.

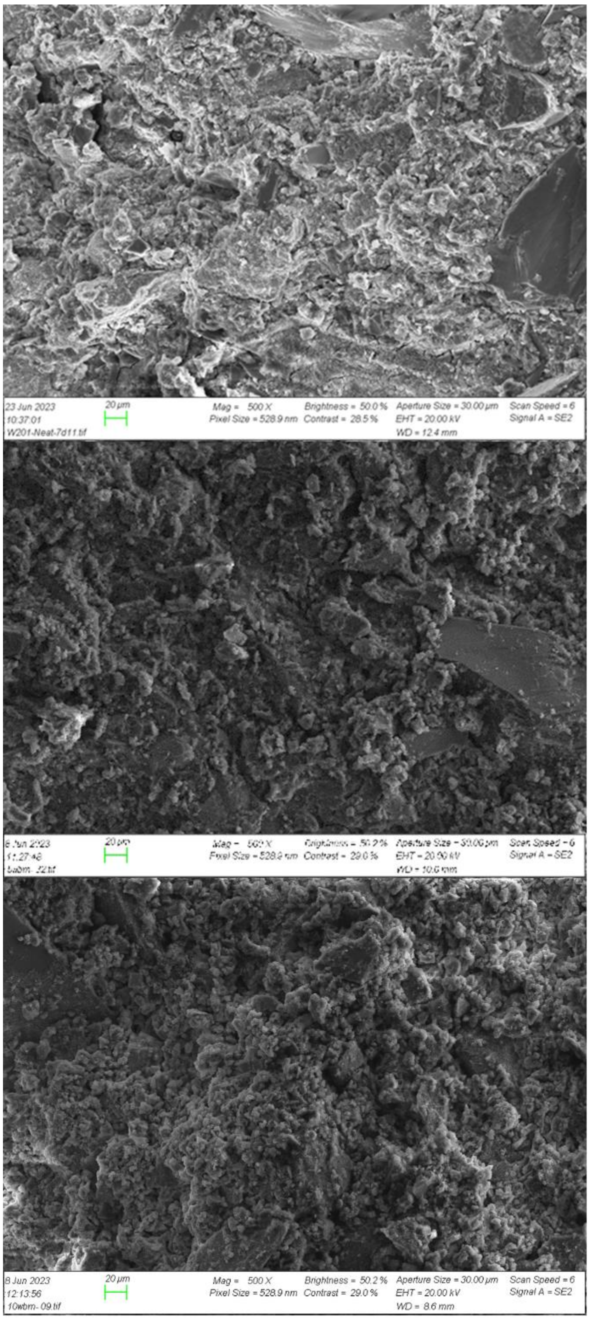

Figure 28 : SEM images of neat and WBDF contaminated geopolymer (a) neat geopolymer (b) geopolymer contaminated with 5% WBDF (c) 10% WBDF (Paper II)

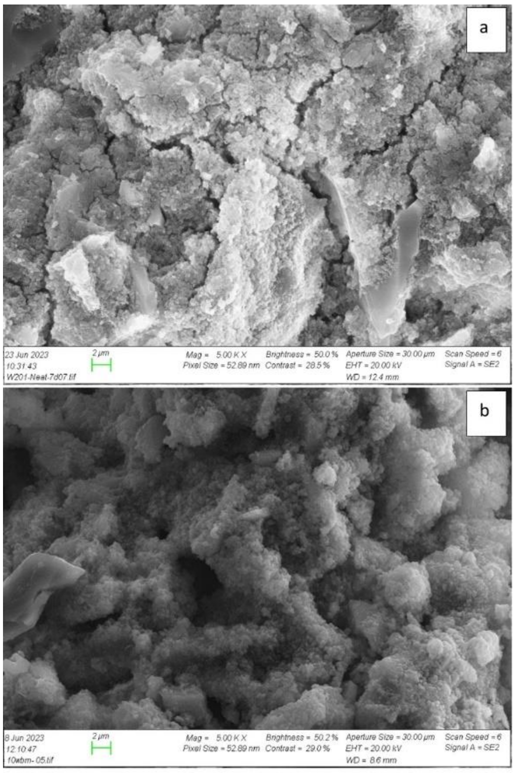

Figure 29 : SEM images of (a) neat geopolymer (b) 10% WBDF contaminated geopolymer at 5K X magnitude

Figure 30 shows the microstructure of OBDF contaminated geopolymer. Microstructural analysis reveals that when geopolymer was contaminated with 5% OBDF, small voids appeared (biggest observed was 20 µm in diameter), converting the geopolymer into an oil-in-water emulsion. With an increase in contamination to 10%, both the number and diameter of these voids increased (biggest observed was 80 µm in diameter). The increase in OBDF contamination has certain impact on porosity due to formation of microcavities. However, it appears to have less influence at low OBDF concentrations on the permeability of the geopolymer, as these voids do not seem to be interconnected.

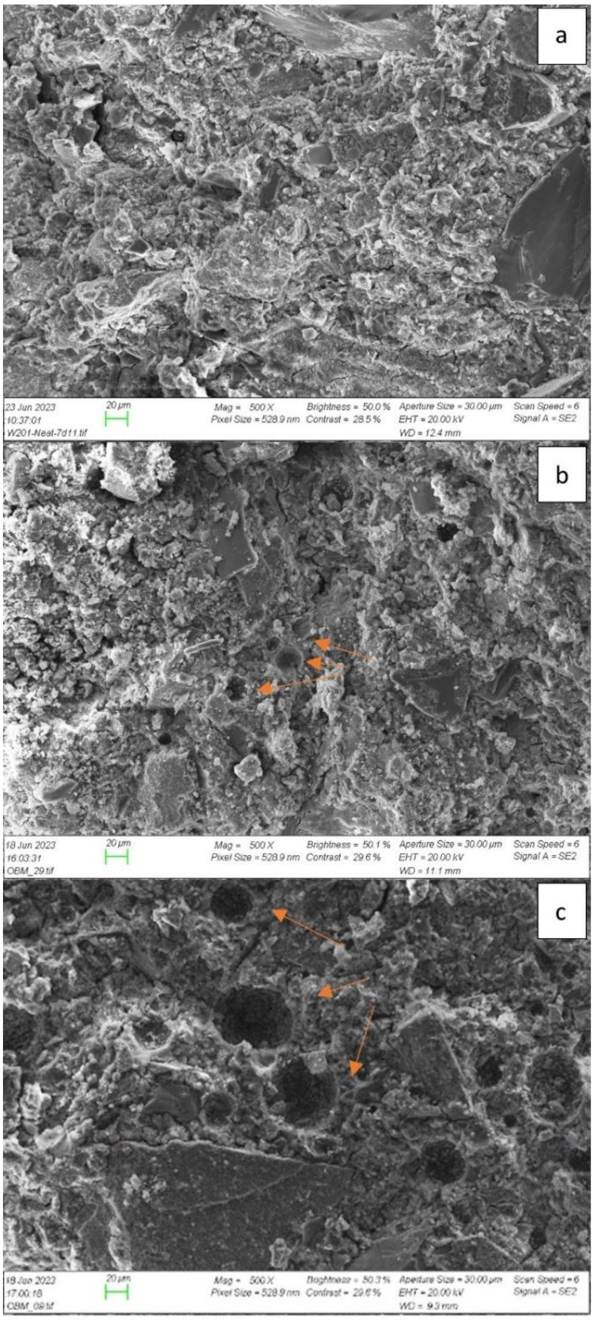

Figure 30 : SEM images of neat and OBDF contaminated geopolymer (a) neat geopolymer (b) geopolymer contaminated with 5% OBDF (c) 10% OBDF (Paper II)

Figure 31 shows one of the voids created by OBDF in higher magnitudes. It can be observed that gel precipitation stopped right at the interface of two immiscible phases. It suggests that these two systems coexisted primarily on a physical basis with minimal chemical interactions between them. An interesting property of geopolymers is their ability to generate an in-situ surfactant through a saponification reaction when an oil source is combined with the highly alkaline environment of the geopolymer [63, 64]. The in-situ surfactant then stabilizes the oil droplets by reducing the interfacial tension aided by high viscosity of continuous phase (geopolymer). As a result, oil droplets do not coalesce, leading to the prevention of phase separation when the geopolymer is in its curing process. Longer setting time also can increase the chance of coalescence. Research has demonstrated that geopolymers have the capability to incorporate high volumes of organic liquids, such as waste materials, into their structures [65].

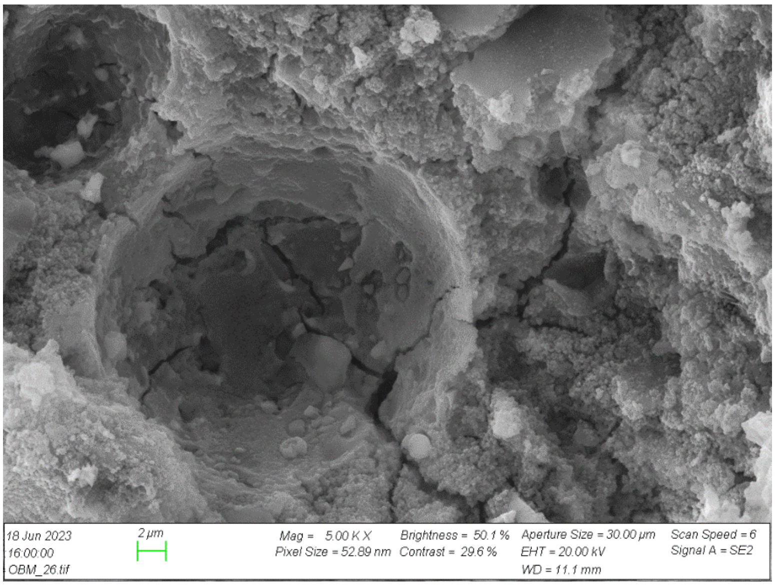

Figure 31 : SEM image of a void created by OBDF

Figure 32 shows images of 10% OBDF samples captured using a Backscattered Electron Detector (BSD), where brighter colors indicate heavier elements and darker colors represent lighter elements. An accumulation of heavier elements, primarily barium, was observed within the voids created by oil droplets. This barium accumulation can be attributed to barite, a weighting agent present in the OBDF mix design. The secondary emulsifier utilized in the preparation of OBDF serves to oil-wet solid particles and drill solids, thereby regulating rheological properties and controlling fluid loss. Consequently, barite, which is oil-wet, remains within the oil phase and does not migrate to the geopolymer slurry.

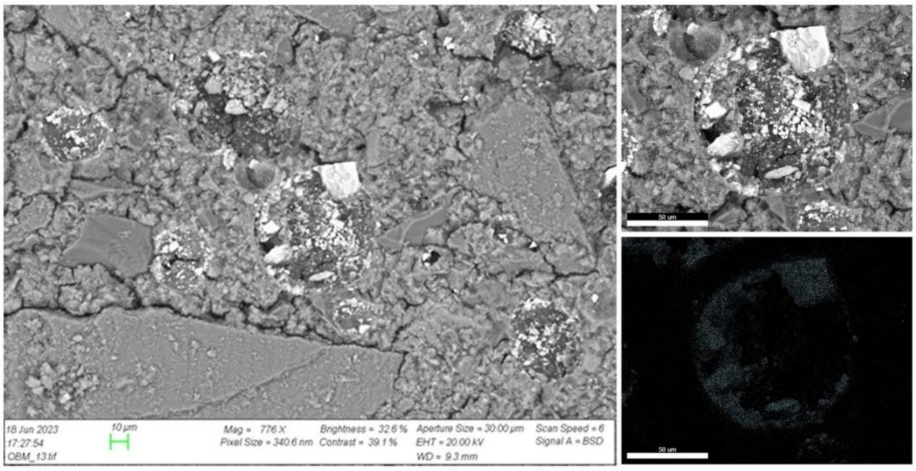

Figure 32: EDS analysis performed on 10% OBDF contaminated geopolymer (Paper II)

5.1.5.2 XRD Analysis

The powder X-ray diffraction (XRD) technique was employed to investigate the crystallography and phases present in the cured geopolymer. This analysis aimed to elucidate any possible phase changes and correlate them with the impact of drilling fluid on geopolymerization. After taking the UCS measurments, the crushed samples were grinded into powder and prepared for XRD test. The XRD patterns of neat and WBDF contaminated samples are shown in Figure 33. The presence of quartz was identified as the major phase in the cured geopolymer, which is expected considering that granite was the main solid precursor used in the mix design. The minor detactable phases were albite (Alb), microcline (Mic), biotite (Bio) and chlorite (Cl). The analysis of the contaminated samples did not reveal the formation of any new phases, indicating that there was no reaction between the spacer and geopolymer resulting in the formation of new minerals. The peaks intensities however namely quartz peak was increased by increasing the WBDF contamination dosage. WBDF can impair the ability of highly alkaline medium of hardner phase to dissolve the crystaline phase of the solid precursure. Thus, faster-dissolving minerals such as Bio and Cl phases were more noticible for 10% WBDF contaminated samples. Figure 34 shows the XRD patterns of OBDF cotaminated geopolymer which indicates that it has less impact on dissoultion ability of geopolymer. From Table 12, it can be observed that the geopolymer containing 10% WBDF exhibited the highest crystallinity, whereas the geopolymer with 10% OBDF had the lowest crystallinity.

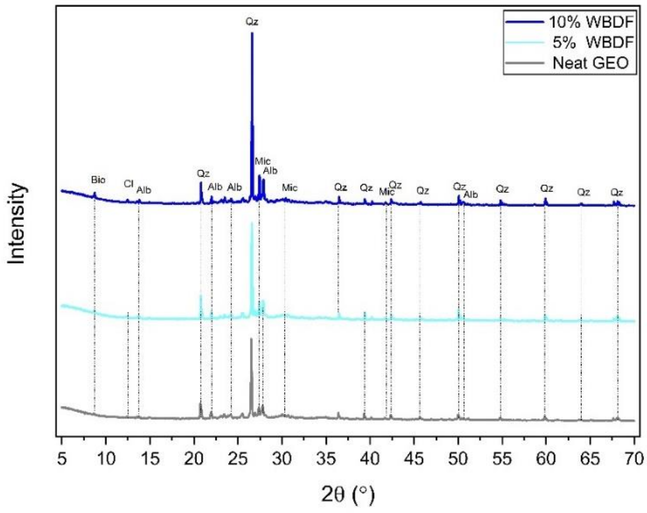

Figure 33 : XRD pattern of WBDF contaminated geopolymer

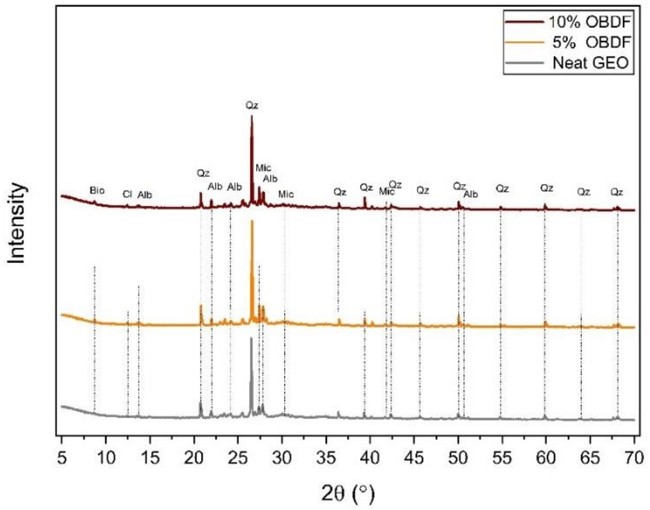

Figure 34 : XRD pattern of OBDF contaminated geopolymer

Table 12 : Quantification of amorphous and crystalline content in contaminated samples based on XRD pattern

Sample	Crystalline content (wt.%)	Amorphous content (wt.%)
Neat geopolymer	65.6	34.4
5% WBDF	66.4	33.6
10% WBDF	68.7	31.3
5% OBDF	66.4	33.6
10% OBDF	64.8	35.2

5.1.6 Kinetics of Reaction

The heat release of geopolymer was monitored with isothermal calorimeter at 50 °C. Figure 35 shows the heat evolution of neat and WBDF contaminated geopolymer. It displayed exothermic reactions characterized by two peaks, one occurring at an early stage and the other after several hours. Upon contact with an alkali medium, the aluminosilicate precursor undergoes dissolution, while simultaneously, geopolymer gel begins to precipitate on the surface of the particles. This initial process leads to a rise in heat release, followed by a rapid decrease as further dissolution is impeded by the gel layer formed on the particles and super saturated aluminosilicate solution [66-68]. Second peak is regarded as main geopolymerization peak where continuous network structure of aluminosilicate gel is formed. Figure 35 shows that the WBDF contamination both hindered and delayed the geopolymerization reaction correlated with deteriorated mechanical properties of contaminated geopolymer. Although drilling fluid is complex system with multiple components in the design, these impacts primarily attributed to the excessive water content introduced by the WBDF as we discuss in next chapter.

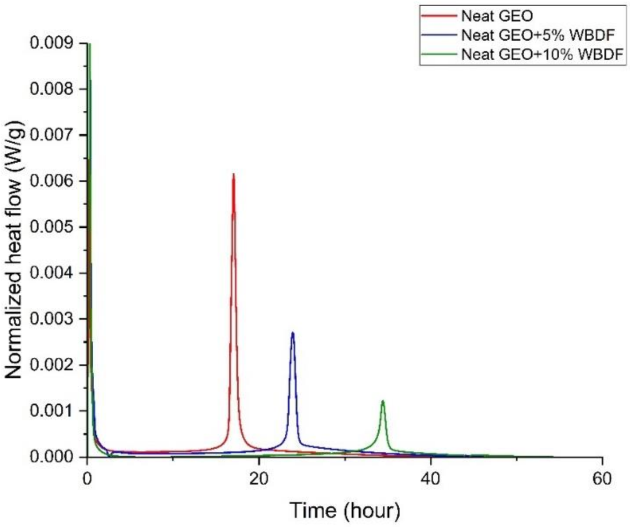

Figure 35 : Heat evolution of WBDF contaminated geopolymer

By addition of 5% OBDF to geopolymer, the polymerization peak shifts to the right, indicating of minimal delay in the process (Figure 36). The intensity of the peak was also marginally reduced, likely due to the presence of the oil phase, which could potentially diminish the volume available for gel precipitation due to immiscibility. As the OBDF content in the geopolymer increased, the oil phase occupied a greater volume, leading to a more pronounced decrease in the intensity of the main peak. From a comparison of the mechanical properties and heat of reaction, it can be concluded that OBDF primarily influences the microstructure with minimal impact on the geopolymerization process. An interesting observation was the occurrence of GEO-10% OBDF peak earlier than GEO-5% OBDF peak that matched the UCA results. The faster setting time might be attributed to the $CaCl_2$ and $Ca(OH)_2$ present in the internal phase of OBDF.

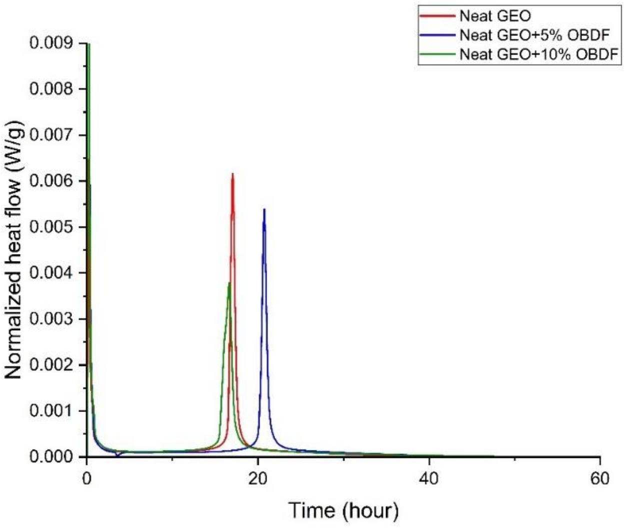

Figure 36 : Heat evolution of OBDF contaminated geopolymer

5.1.7 Bond Strength of Geopolymer to Casing with OBDF on the Surface

Shear bond strength of geopolymer to the rusty and OBDF covered surface of pipe was measured after curing for seven days. Table 13 shows the shear bond strength of geopolymer to the different surfaces. When a layer of OBDF was present on the pipe surface, the shear bond strength exhibited a reduction of 48%. This reduction can be attributed to two reasons: wettability alteration and reduction in the contact area between the geopolymer and the pipe. Thus, the residual drilling fluid layer on the wall of casing should be avoided with practices such as mechanical removal and/or well-designed spacers.

Table 13: Shear bond strength of geopolymer to the steel pipe

Surface of Pipe	Rusty	Covered with OBDF
Shear Bond Strength	0.105 MPa	0.055 MPa

5.2 Spacer Design for Geopolymer

This section describes the process design of spacer fluid for the in-house geopolymer. This would mitigate the risks associated with drilling fluid contamination as discussed in chapter 5. We used the concept of solidification (geopolymerization) of filter cake and drilling fluid [69] to design a spacer that can harden with time and contribute to the zonal isolation. It has enough pumpability time which allows it to be placed in the annulus before setting. Properties of base spacer design that was selected for the further development is shown in Table 14.

Table 14: Properties of hardening spacer (base spacer) (Paper III)

	Density(s.g.)	pH	Free fluid (%)	Compressive strength (MPa)		Pumpability
				1d	7d	
Hardening spacer	1.52	11.47	16	8.78	10.86	Minimum 7 hr

5.2.1 Tuning the Flow Behavior of Spacer

The rheological properties of downhole fluids play a critical role in determining the effectiveness of mud displacement in the annulus. Given that the properties of drilling fluid and cement/geopolymer are often difficult to alter due to various limitations, the properties of the spacer fluid become particularly significant. It is important for the spacer to have a tuneable viscosity and yield stress to maintain the viscosity hierarchy among the pumped fluids which improves displacement efficiency [70]. Three common viscosifiers used in drilling fluids, namely xanthan gum, PAC (PolyAnionic Cellulose), and bentonite, were added to the spacer fluid to assess their impact on the flow behavior. Figure 37 shows the flow curve of the spacer with different concentration of xanthan gum (0.1, 0.2, 0.5, and 1% by weight of water). The viscosity of the spacer was increased by increasing the concentration of xanthan gum in the system. The decline in viscosity with increasing shear rate suggests a shear-thinning characteristic across all fluids. This phenomenon arises from diminished intermolecular interactions and the disentanglement of polymer networks, resulting in decreased frictional forces and partial alignment of macromolecules parallel to the direction of shear flow [71]. Upon shear removal, the network structure quickly reforms through Brownian motion, leading to almost instantaneous recovery of viscosity. This explains the analogy observed between the ramp-up and ramp-down shear stress measurements. The high shear viscosity observed at low shear rates or during rest is attributed to the hydrogen bonding between long chains and polymer entanglement of xanthan gum's large molecules [72].

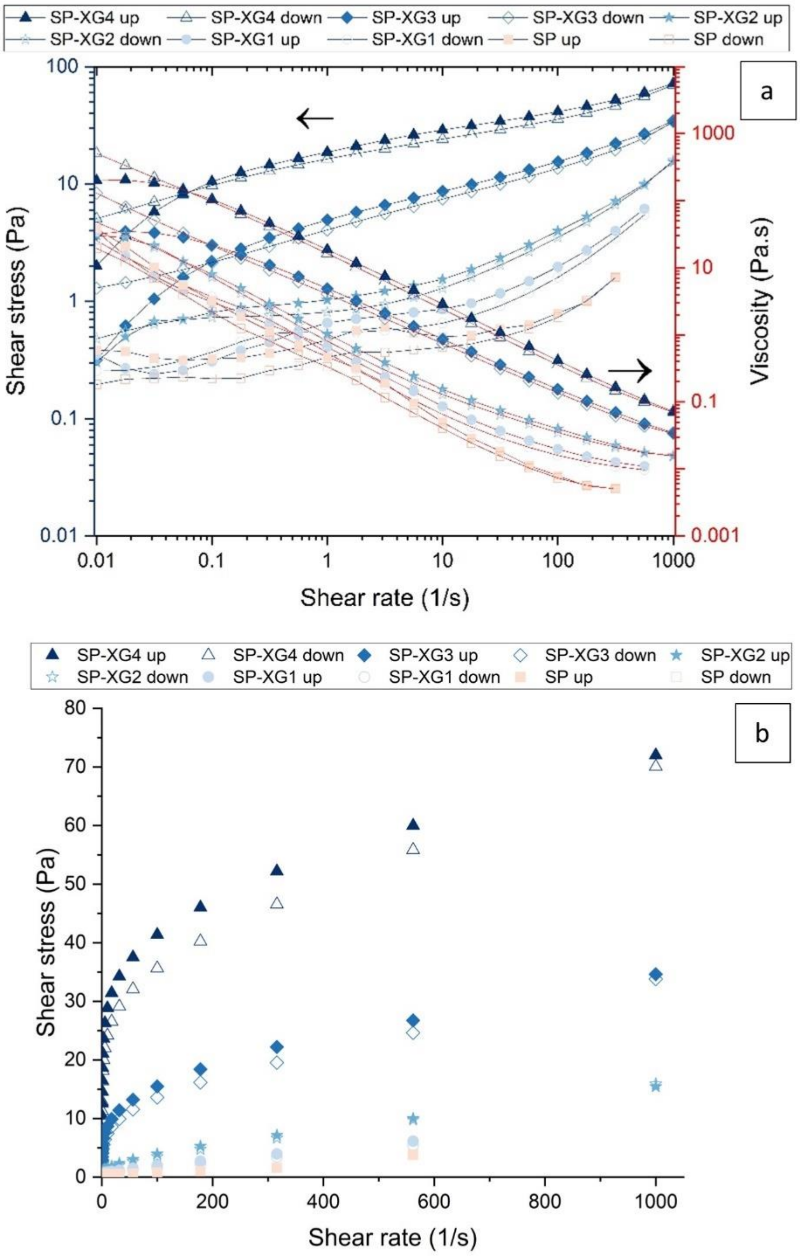

Figure 37 : Flow curve of spacer with different concentration of XG (for information regarding the concentrations refer to Table 7). (a) logarithmic scale (b) linear scale (Paper III)

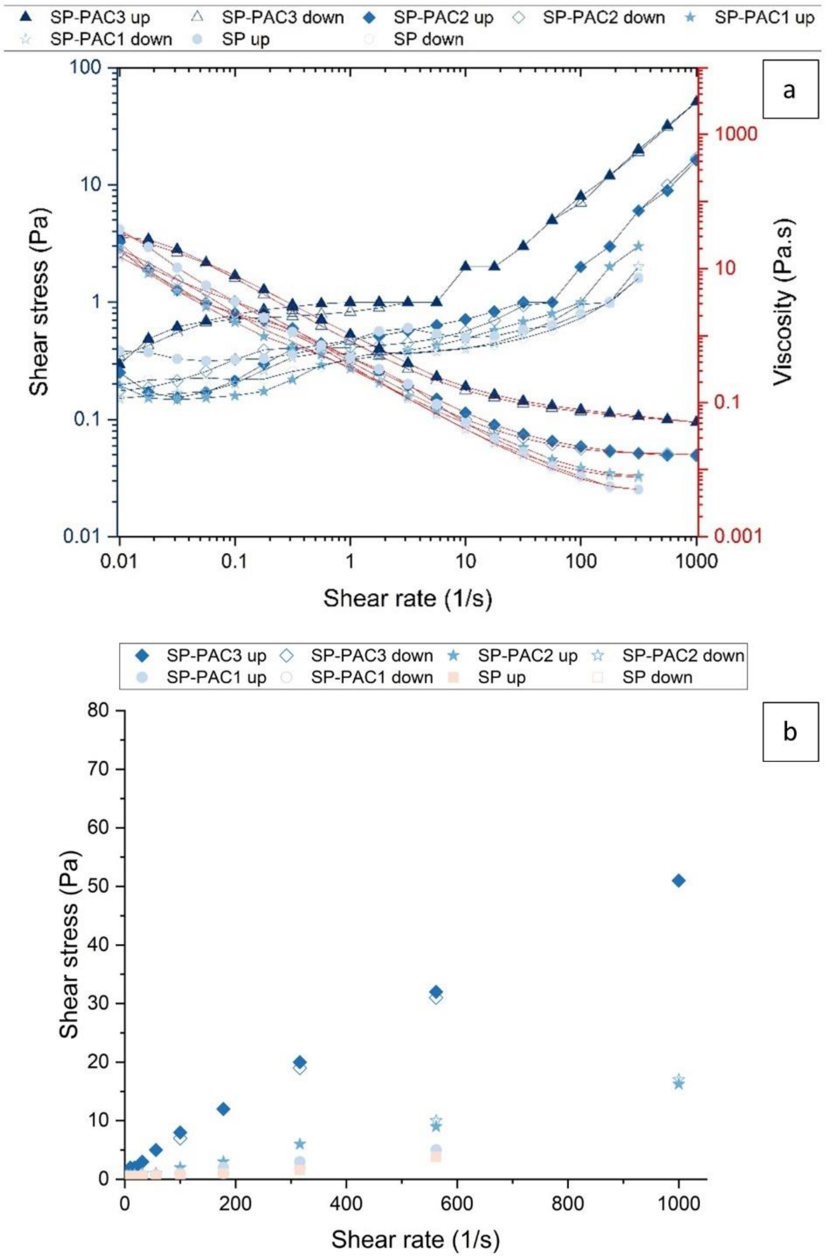

Figure 38 : Flow curve of spacer with different concentration of PAC (for information regarding the concentrations refer to Table 7). (a) logarithmic scale (b) linear scale (Paper III)

Figure 38 shows the impact of the different concentration of PAC on the flow curve of spacer fluid. The viscosity of spacer was increased with the addition of PAC. However, less shear thinning profile was observed compared to XG.

To obtain the rheological parameters, two different models: Bingham plastic and Herschel Bulkley commonly used for downhole fluid characterization are used (Table 15). Base spacer fluid exhibited behavior similar to that of a Bingham plastic characterized by a low yield stress calculated using curve fitting. As the concentration of xanthan gum in the spacer was increased, the value of ‘n’ decreased significantly, indicating a higher degree of shear-thinning behavior of the fluid. This resulted in a coefficient of determination (R^2) closer to 1 for H-B model. Additionally, the yield stress was increased with the addition of XG. It is noteworthy that the Bingham model predicted a higher yield stress compared to the H-B model. Table 15 also displays the viscosity model parameters for the spacer containing PAC. Relative to XG at the same concentration, PAC resulted in a lesser decrease in ‘n’, suggesting behavior closer to that of a Bingham fluid. This could potentially benefit the spacer fluid by enhancing its displacement performance in horizontal section, as indicated by a study by [73]. Furthermore, the lower yield stress observed with the addition of PAC compared to XG at equivalent concentrations may stem from differences in their molecular weights and chain length.

Table 15 : Rheological parameters of spacer with XG and PAC as rheology modifier (Paper III)

		Rheological model								
		Bingham				H-B				
Additive	Concentration (wt% of water)	**τ_y(Pa)**	**μ_p(Pa.s)**	**R^2**	**SSE**	**τ_y(Pa)**	**k(Pa.s^n)**	**n**	**R^2**	**SSE**
- (base spacer fluid)	-	0.36	0.004	0.9982	0.0027	0.36	0.003	1.03	0.9984	0.002
XG	0.1	0.49	0.01	0.9875	0.3798	0.42	0.03	0.83	0.9951	0.1569
	0.2	1.05	0.02	0.9837	4.817	0.74	0.07	0.77	0.9974	0.7601
	0.3	5.20	0.03	0.8568	213.5	1.62	2.05	0.39	0.9917	12.34
	0.4	17.65	0.06	0.7648	1422	4.3	10.2	0.26	0.9865	81.38
PAC	0.2	0.34	0.006	0.9991	0.0037	0.35	0.004	1.07	0.9999	0.0003
	0.3	0.4018	0.01646	1	0.01176	0.3911	0.01711	0.9943	1	0.009934
	0.4	1.51	0.05	0.9963	10.27	0.63	0.12	0.87	1	0.0485

Figure 39 illustrates the flow curve of the base spacer with varying concentrations of bentonite added, tested at a temperature of 50°C. A peak in shear stress was observed between shear rates of 0 to 100 1/s for the fluids containing bentonite, indicative of viscoelastic behavior. This phenomenon can be attributed to the plate-like shape of bentonite particles, which tend to form a structure resembling a house of cards due to electrostatic charges present on the surface and edges of these clay platelets [74]. As the concentration of the clay was increased, a continuous gel structure was formed under conditions close to rest. This structure can be broken at a certain shear rate, leading to a peak in shear stress. This peak in shear stress tended to increase as the concentration of the clay was increased. Accuracy of fit and R^2 was low for Bingham and H-B models due to viscoelasticity. Therefore, it was decided to determine the yield stress using the oscillatory method, despite knowing that it may yield different approximations compared to the rotational method. Figure 40 depicts the shear strain amplitude sweep conducted on the base spacer and the spacer with bentonite as a rheology modifier at 50℃, measured using the oscillatory method. G’ for base spacer was increased from approximately 100 Pa to close to 5500 Pa with 6 wt% bentonite. G’’ was decreased with the addition of bentonite up to 2 wt%, while 4 and 6 wt% bentonite increased the G’’.

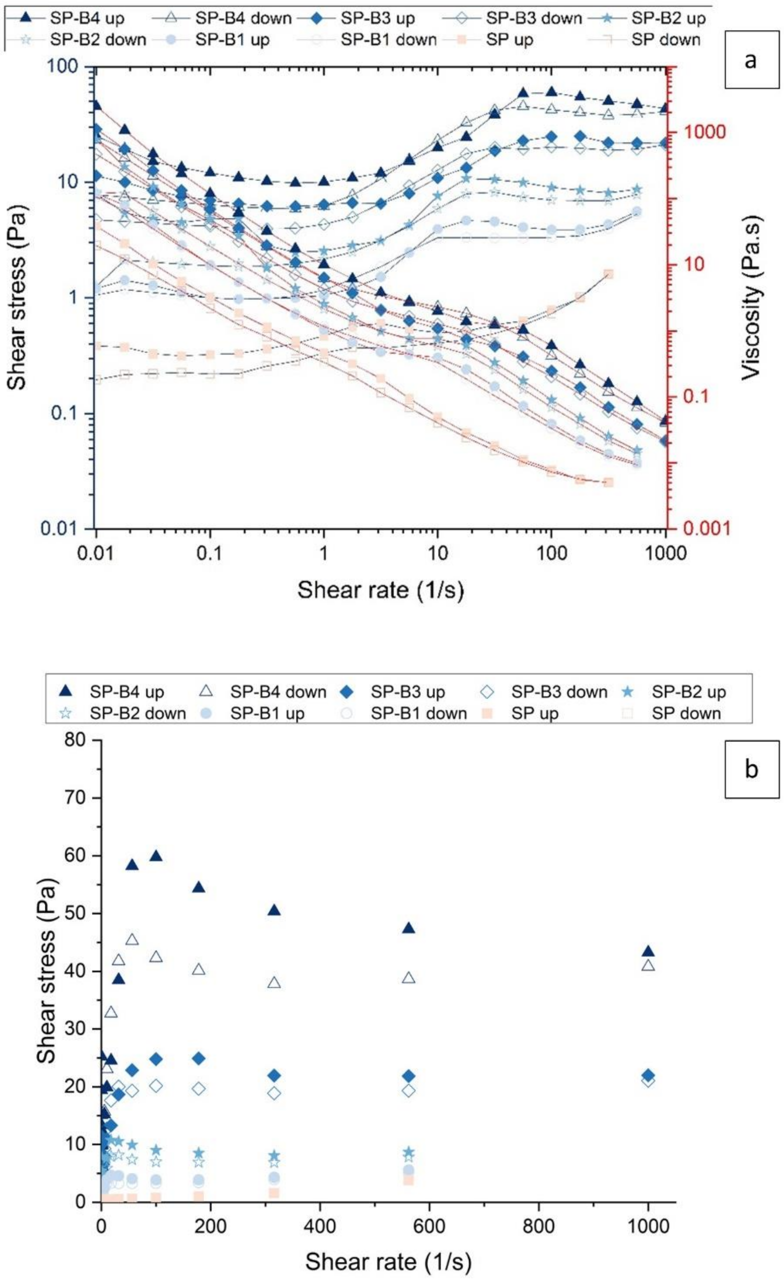

Figure 39 : Flow curve of spacer with different concentration of bentonite (for information regarding the concentrations refer to Table 7). (a) logarithmic scale (b) linear scale (Paper III)

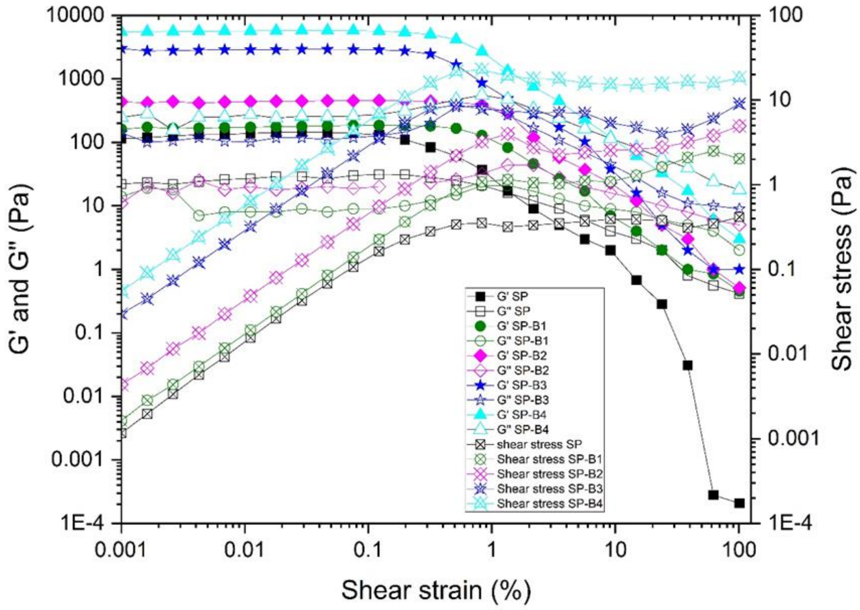

Figure 40 : Strain amplitude sweep of spacer with different concentration of bentonite (for information regarding the concentrations refer to Table 7) (Paper III)

When the loss modulus matches or surpasses the storage modulus, it signifies a substantial alteration in the material's structure, causing it to transition into a flowing state, which is referred to as the flow point. The measured flow points for the spacer with varying concentrations of bentonite are presented in Table 16. The incorporation of bentonite elevated the flow point of the spacer.

Table 16 : Flow point of spacer with different concentration of bentonite (Paper III)

Fluid	SP	SP-B1	SP-B2	SP-B3	SP-B4
Flow point (G’=G’’, Pa)	0.3	1.0	2.6	9.1	15.3

5.2.2 Preliminary Tests for Surfactant Selection

The strategy involved considering surfactants known for their wetting and oil-in-water emulsifying abilities and comparing them to a conventional surfactant typically used in cement spacers. This comparison aimed to identify a surfactant of interest for further investigation. Three nonionic surfactants (two sourced from VWR and one from Baker Hughes) were chosen for initial testing and to determine the most effective option. Table 17 provides details of these surfactant.

Table 17 : General information of surfactants used in pre-screening

Name	Chemical Composition	Description	HLB	Concentration (by the weight of water)
Surfactant A	Polyoxyethylene (10) tridecyl ether	Nonionic	17.4	1.66 %
Surfactant B	Secondary C12-14 Alcohol ethoxylate	Nonionic	14	1.66 %
Surfactant C	Fatty alcohol (Commercial product from Baker Hughes)	Nonionic	-	1.66 %

One of the important criteria for the selection of the surfactant is the ability to clean the surface of the casing while the spacer is displacing mud in the annulus. Spacer fluids with different surfactants at the same concentration were prepared and the rotor cleaning test was performed at room temperature. Figure 41 shows pictures of the viscometer rotor after being washed with spacer fluids. Surfactants A and C exhibited the best performance by visual inspection, although the difference between them is not significant. Washing the rotor with surfactant B resulted in a small layer of OBDF on the surface of the sleeve.

Figure 41 : Pictures of viscometer rotor after washing with (a) spacer with no surfactant (b) spacer with surfactant A (c) spacer with surfactant B (d) spacer with surfactant C

In the next stage, the impact of surfactants on the spacer flow behavior was evaluated (Figure 42). The surfactant C had lowest impact on the flow curve measured at 50 °C. Addition of surfactant A and B to the spacer resulted in increased shear stress at equivalent shear rates.

Since the spacer is pumped ahead of geopolymer slurry during primary cementing, there is a possibility of mixtures of these fluids. It is important to check the compatibility of the surfactant used in the spacer with the geopolymer, to avoid unexpected retardation or acceleration caused by this component. Figure 43 shows the thickening time of neat geopolymer (without retarder in the design) with different surfactants as a contaminant. Neither of the surfactants resulted in a significant change in the thickening time of the geopolymer. However, high initial consistency values were observed for the geopolymer containing surfactant A and B. This indicates the viscosifing effect of these surfactant on the geopolymer slurry.

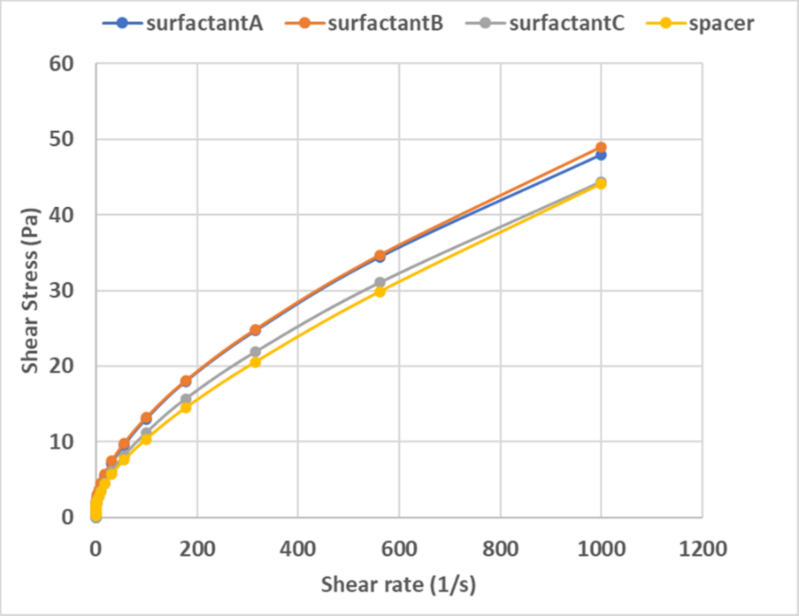

Figure 42 : Impact of surfactants on the flow behavior of spacer

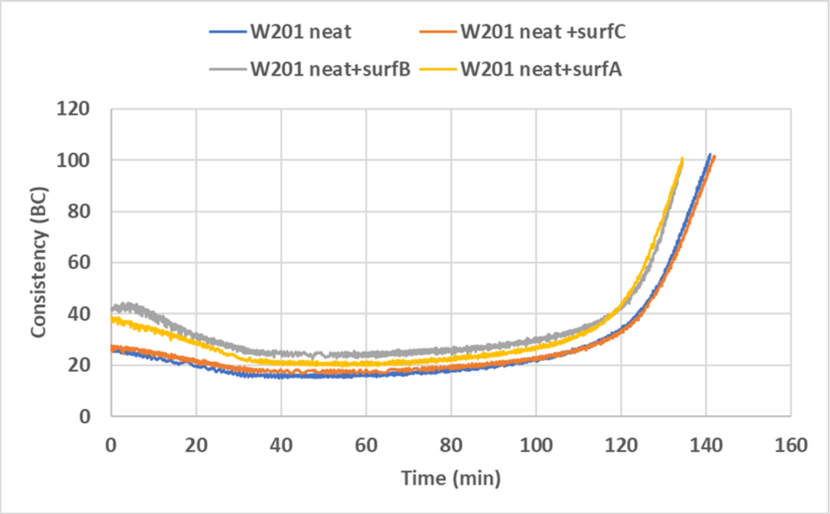

Figure 43 : Impact of surfactants on the thickening time of gepolymer

5.2.3 Optimizing Surfactant Concentration

Due to less impact on spacer flow behavior and being less contaminant to geopolymer and economical aspects, it was decided to continue with surfactant C for further testing. To adjust the concentration of the surfactant, three different concentrations were tested (Table 7), and their impact on casing cleaning ability and casing wettability (contact angle) was measured.

5.2.3.1 Casing Cleaning Ability of Spacer

The efficacy of the spacer fluid in cleaning the casing surface was evaluated through rotor cleaning tests. Figure 44 depicts the viscometer sleeve covered with OBDF before and after washing with a surfactant-free spacer. Some mud traces were still visible on the sleeve's surface after washing. Incorporating surfactant (8.33% by weight of water) into the spacer formulation led to improved cleaning of the viscometer sleeve, as shown in Figure 45. For comparison, the same test was conducted using water as the spacer, revealing significant OBDF residue on the surface, as depicted in Figure 46. This suggests that the particles in the spacer contribute to the cleaning of the casing wall. The cleaning efficiency, calculated using the formula (4.2.1), is provided in Figure 47. It can be observed that the spacer without surfactant exhibited a cleaning efficiency of 72%, while the addition of 0.83 wt% (by water) surfactant enhanced the cleaning efficiency to 94%. Once a certain concentration of the surfactant package was reached, the cleaning efficiency plateaued, indicating that further increases in concentration do not yield additional improvements. Using water as the spacer fluid resulted in a cleaning efficiency of 37.5%, highlighting the inadequacy of water as a preflush in cementing operations.

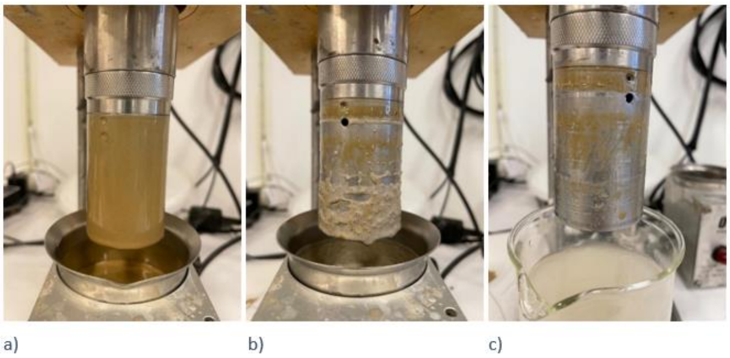

Figure 44 : Rotor cleaning test with surfactant-free spacer after rotating in (a) in OBDF (b) spacer (c) water (Paper III)

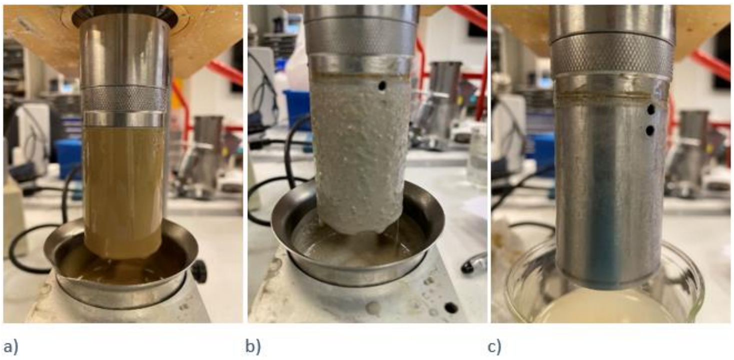

Figure 45 : Rotor cleaning test with spacer (SP-S3) after rotating in (a) in OBDF (b) spacer (c) water (Paper III)

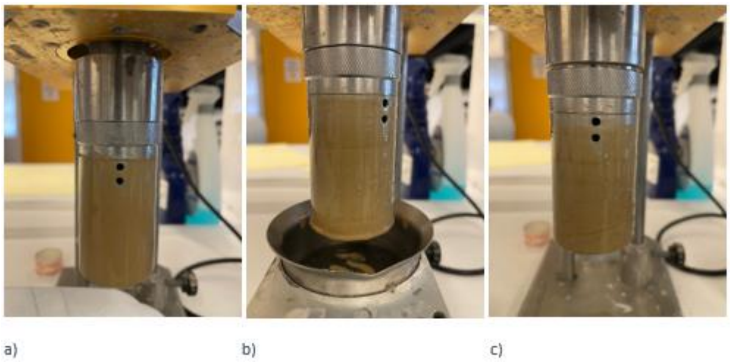

Figure 46 : Rotor cleaning test with water as spacer after rotating in (a) in OBDF (b) spacer (c) water (Paper III)

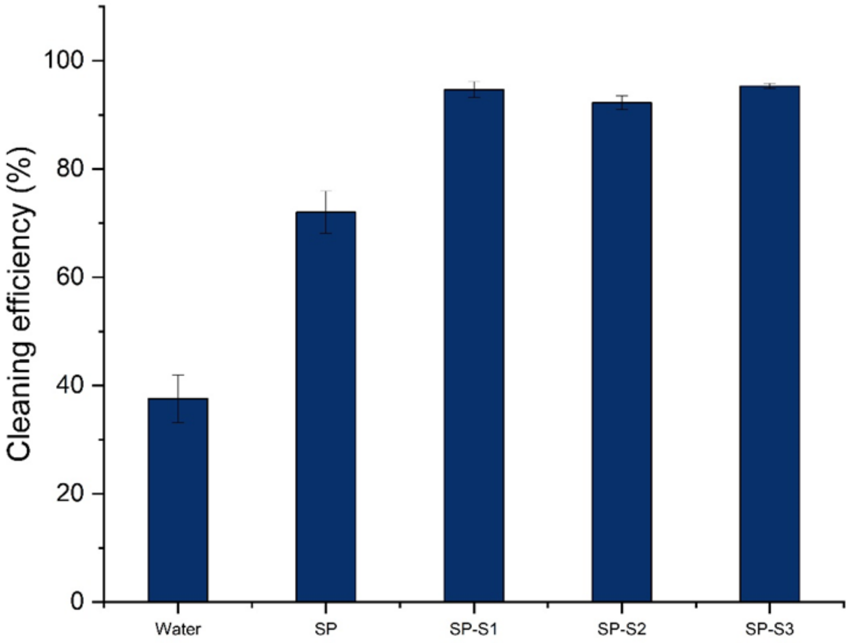

Figure 47 : Casing cleaning efficiency of spacer with different concentration of surfactant (Paper III)

5.2.3.2 Contact Angle Measurement

Figure 48 and Figure 49 depict the contact angle of water droplets on the surface of steel treated with different fluids. The procedure for this test is explained in 4.2.2. The clean surface of the steel coupon with a neat surface exhibited a contact angle of 72 degrees, indicating intermediate wettability [75]. After immersion in the OBDF, the contact angle remained almost unchanged. However, washing the mud-covered steel with the spacer-containing surfactant (SP-S1) with 0.83 % concentration significantly reduced the contact angle, resulting in a strongly water-wet surface. The lipophilic tails of the surfactant molecules attach to the steel surface, causing it to become water-wet and allowing water droplets to spread almost completely. Further increasing the concentration of surfactant reduced the contact angle to 5 degrees.

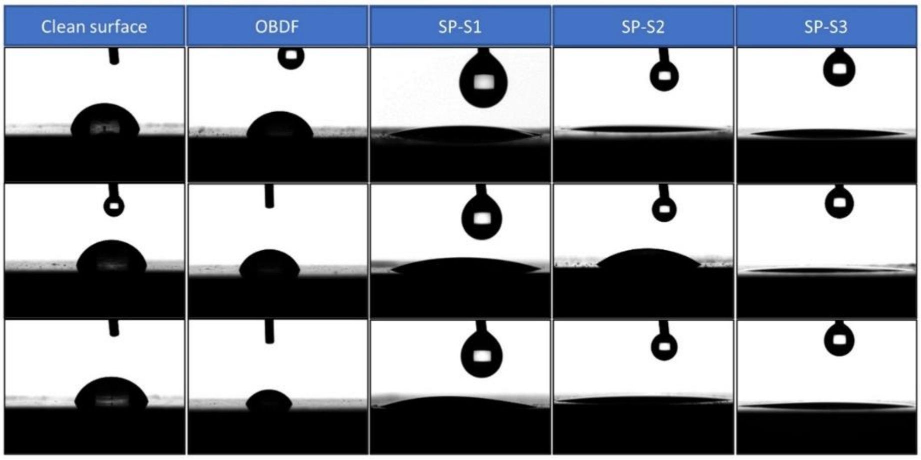

Figure 48 : Images of water droplet on the steel coupon treated with different fluids (Paper III)

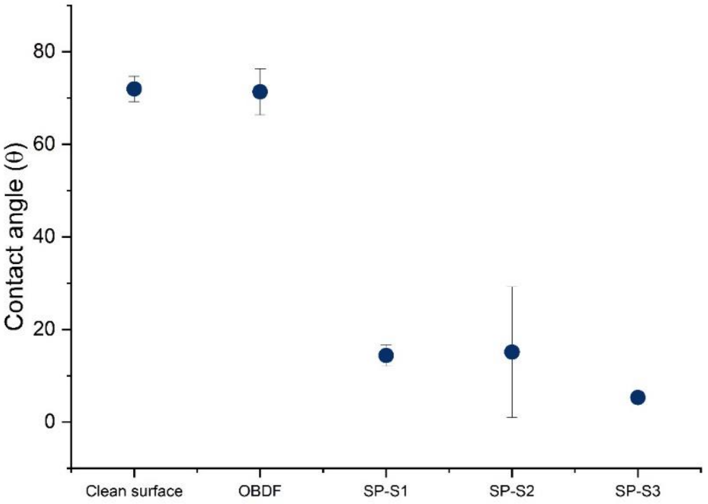

Figure 49 : Contact angle of water droplet on the steel coupon treated with different fluids (Paper III)

5.2.3.3 Emulsion Stability Test

This test examines the capability of the spacer to invert OBDF emulsion. It is evident that with an increase in the volume of titrated spacer, the stability of the emulsion was compromised (Figure 50). Finally, when the voltage showed zero, the emulsion was completely broken. This occurs because the spacer increases the water content, leading to the formation of larger and additional water droplets within the emulsion. As a consequence, this leads to a reduced voltage required for internal phase coalescence and the initiation of current. Surfactant (8.33% by weight of water) also proved to be effective in breaking the emulsion faster and at lower concentrations of added spacer. The surfactant diffuses into water/oil interface and promote the water droplets destabilization.

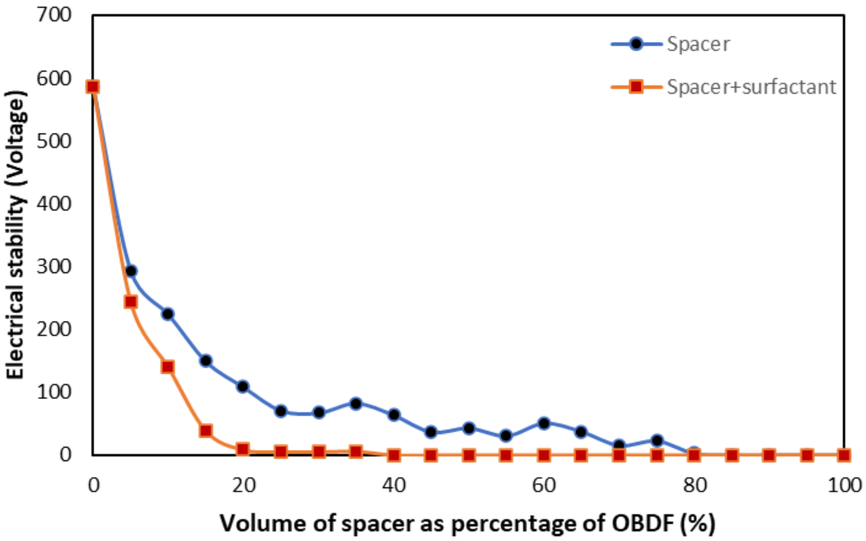

Figure 50 : Electrical stability of OBDF upon mixing with spacer (Paper IV)=

5.2.4 Compatibility of Spacer and Drilling Fluid

Spacers play pivotal roles in cementing operations by serving two essential functions: firstly, they are responsible for cleaning and removing drilling fluid from the wellbore, and secondly, they work to minimize cement contamination caused by the drilling fluid. Laboratory testing of the spacer should incorporate procedures to assess compatibility with drilling fluid and geopolymer as it is in direct contact with them.

First, the rheological compatibility of the spacer and OBDF was investigated by measuring the flow curve of mixtures (95/5, 75/25,50/50, 25/75, and 5/95 by volume of spacer/OBDF) at 25℃. The role of surfactant in the flow behavior of mixture fluid was also examined by comparing two cases of spacer (with and without surfactant). Figure 51 illustrates the ramp down flow curve of spacer (without surfactant) and OBDF mixture. 50/50 mixture had the highest viscosity profile. A reason for that might be the attraction of water from spacer to the internal phase of OBDF by osmotic pressure mechanism [41]. As result a thick separate layer of spacer is formed along the OBDF which is better illustrated in Figure 53.

On the other hand, when surfactant was incorporated in the spacer design, 75/25 (spacer/OBDF) mixture had a high viscosity profile with pronounced change at lower shear rates as shown in the Figure 52. The huge viscoelastic behavior observed is attributed to a strong network of structures formed by bridging surfactants [76]. Moreover, unexpected reduction for 25/75 mixture was observed which indicates that OBDF emulsion is broken by the spacer. R-factor for the assessment of the degree of compatibility of the fluids are provided in the appendices.

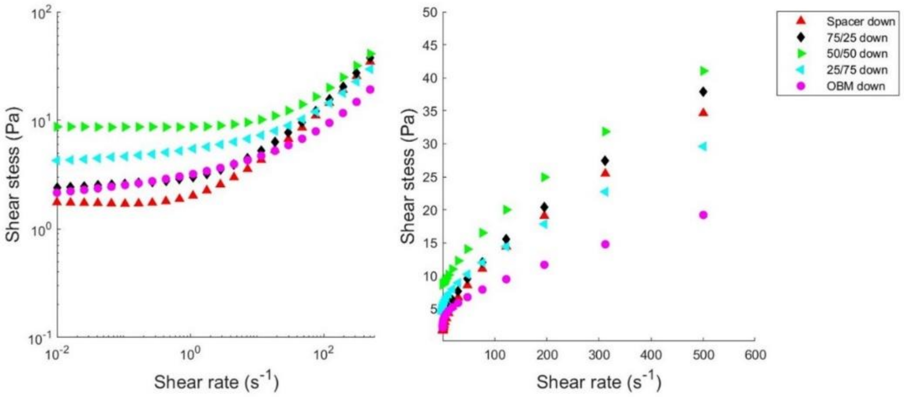

Figure 51 : Flow curve of OBDF and spacer (without surfactant) mixture. (Left) Logarithmic scale. (Right) Linear scale (Paper IV)

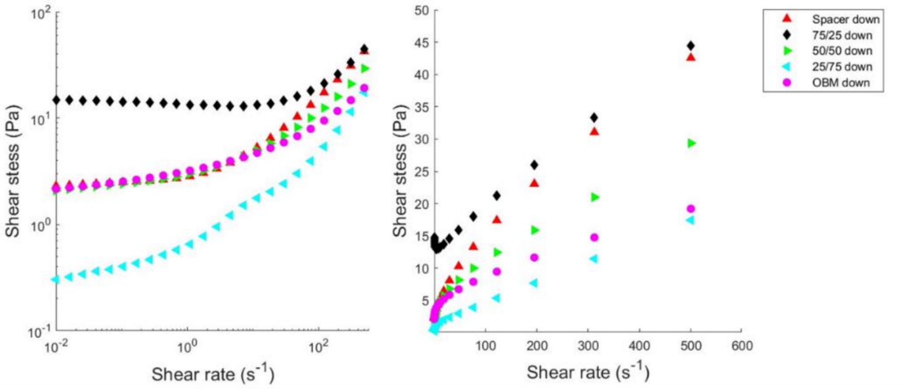

Figure 52: Flow curve of OBDF and spacer (with surfactant) mixture. (Left) Logarithmic scale. (Right) Linear scale (Paper IV)

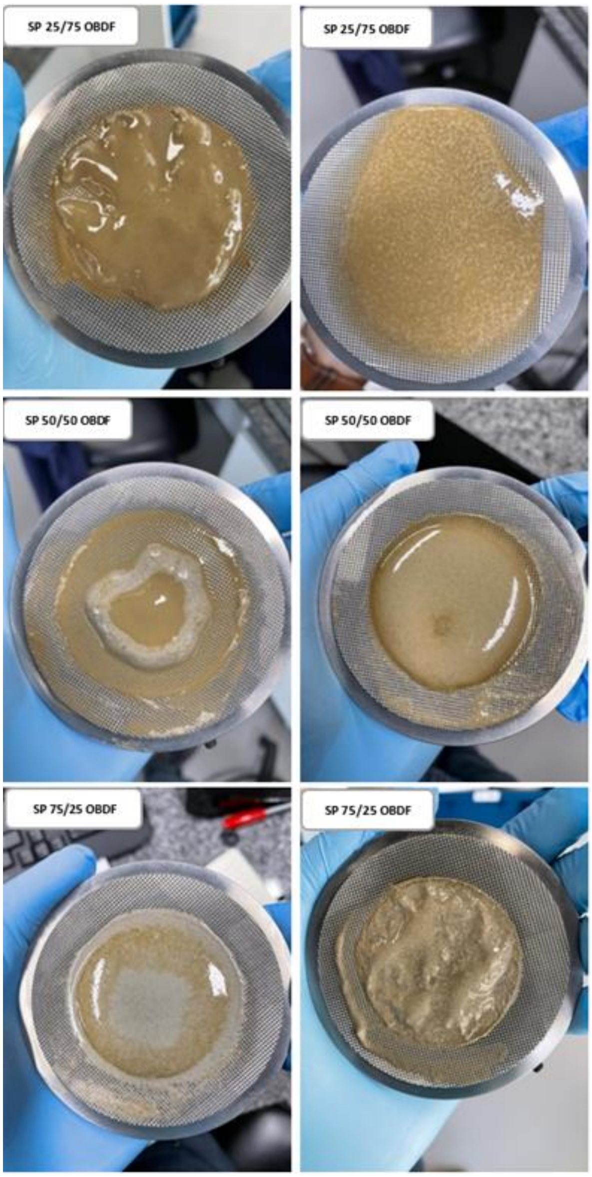

Figure 53 : Images of spacer/OBDF mixtures (Left) surfactant-free spacer (Right) spacer with surfactant (Paper IV)

5.2.5 *Impact of Surfactant on the Displacement of OBDF*

Two experimental scenarios were conducted to observe the displacement of OBDF aimed at analysing the impact of the surfactant on displacement. In Figure 54, the outlet fluid density collected at different time points after initiating the displacement. In the beginning, as the OBDF was exiting the tube, the measured density closely resembled that of the OBDF itself. After a certain period, once the spacer began exiting the tube, the outlet density matched the density of the spacer. The normalized outlet density, (ρ_1 - ρ) / (ρ_1 - ρ_2), provides a clearer understanding for the comparison of fluids with different densities. Simply put, the normalized outlet density ideally ranges between 0 and 1, depending on whether the lighter fluid (OBDF) or the heavier fluid (spacer) is being displaced out of the tube. If we consider the normalized outlet density as a qualitative measure of effective displacement, it can be concluded that the surfactant did not have a significant impact on the bulk displacement process. Nevertheless, Surfactant was effective in cleaning the annulus walls covered with OBDF, as indicated by Figure 55, where the yield stress was not exceeded on the walls. The mechanism involves alteration of wettability, aiding the solubilization of the oil.

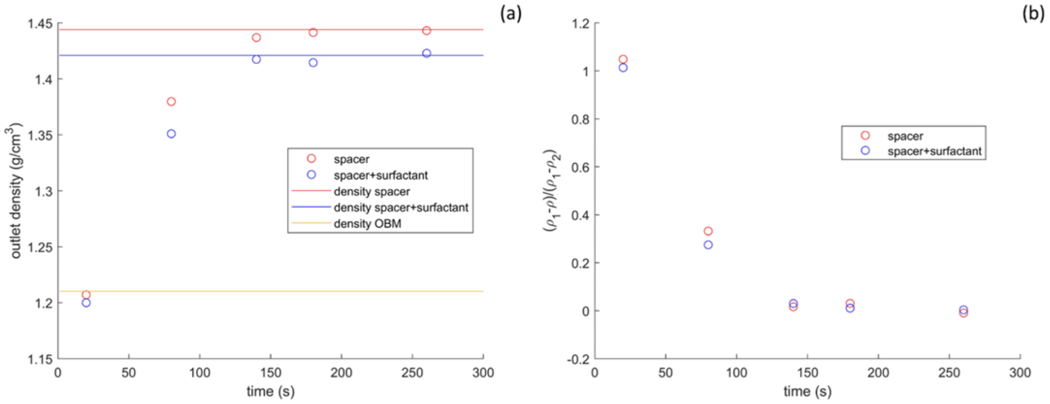

Figure 54 : (a) Outlet density and (b) normalized outlet density of the displacement tube (solid lines represent the density of pure fluids) (Paper IV)

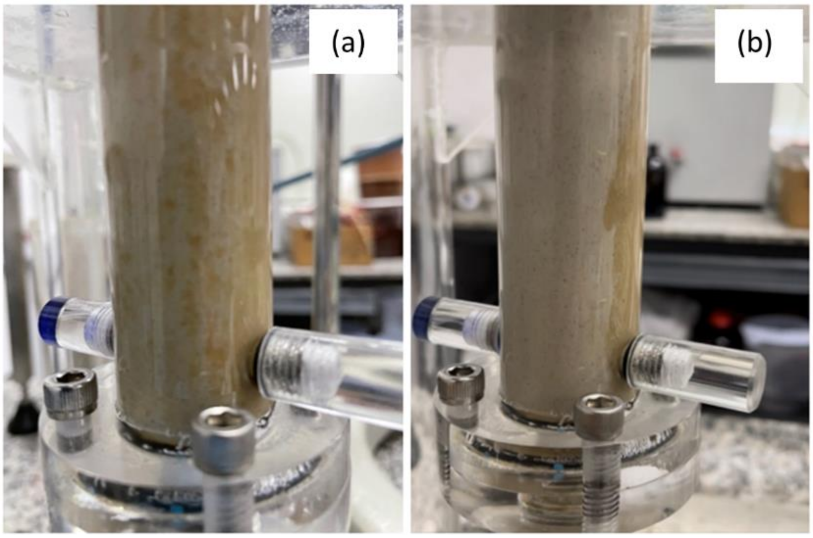

Figure 55 : Images of the displacement tube after the test. OBDF (brown color) was displaced by (a) spacer without surfactant (b) spacer with surfactant (Paper IV)

5.2.6 Compatibility of Spacer and Geopolymer

In the next step, compatibility of spacer and geopolymer was assessed by measuring the flow behavior of the mixture and mechanical properties of geopolymer after intermixture. This ensures that the spacer does not compromise the essential properties of the geopolymer that are crucial for its zonal isolation functionality.

5.2.6.1 Rheological Compatibility

The rheological compatibility of the optimized spacer (SP-O1) and geopolymer was conducted at 50℃ with a rotational viscometer. Spacer and geopolymer were mixed at different ratios recommended by API 10B-2 [56] (95/5, 75/25, 5/95, 25/75, and 50/50 by volume geopolymer/spacer), and the viscosity profile of the mixtures was measured (Figure 56).

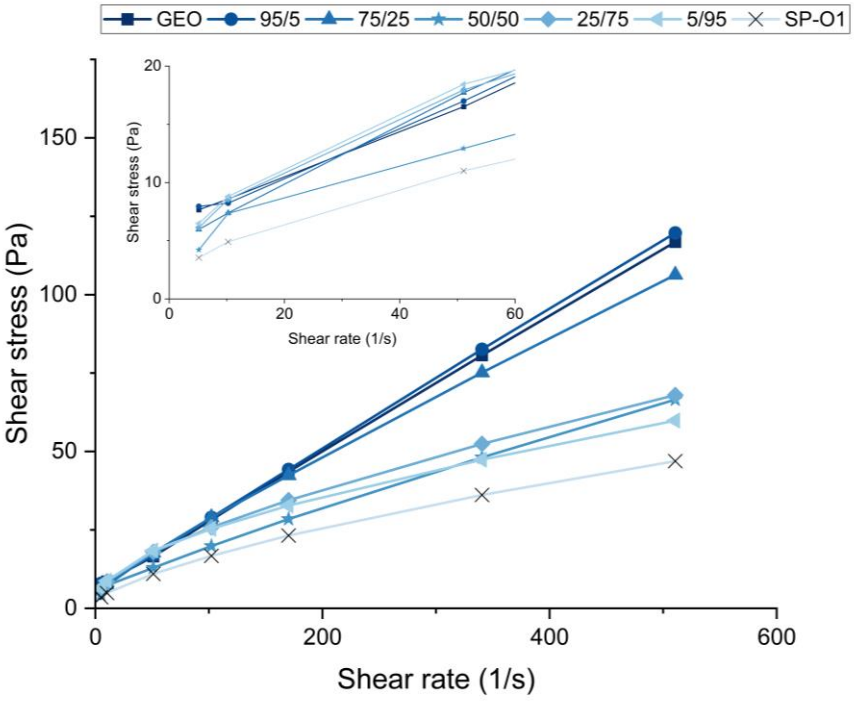

Figure 56 : flow curve of different mixtures ratios between spacer and geopolymer (Paper III)

It is evident that the spacer exhibited a higher degree of shear-thinning behavior compared to the geopolymer slurry. The lower viscosity profile of the spacer compared to the geopolymer is necessary to maintain the viscosity hierarchy during displacement. As the spacer was introduced into the geopolymer, the measured shear stress decreased. This is expected since the spacer contains a higher water content, diluting the geopolymer and resulting in a lower particle fraction and viscosity. The R-index, calculated using the formula (4.2.5) presented in Table 18. To use the guideline, R-index needs to be converted from Pa to lb/100ft (2.084 conversion factor). According to the criteria, the fluids demonstrated rheological compatibility within the studied shear rate range. In other words, the rheological properties of the mixtures remained relatively consistent compared to those of the individual fluids.

Table 18 : R-index calculated for the mixtures of spacer and geopolymer (Paper III)

Shear rate (s^{-1})	Shear stress (Pa)							R-index (Pa)
	GEO 100/0	95/5	75/25	50/50	25/75	05/95	Spacer 0/100	
510.9	124.7	127.8	113.4	71.0	72.6	63.9	50.1	3.1
340.6	86.1	88.2	80.2	51.4	56.0	50.6	38.6	2.0
170.3	46.5	47.2	45.2	30.4	36.8	35.0	24.8	0.8
102.2	30.2	30.9	30.9	21.2	27.6	27.1	17.9	0.8
51.1	17.6	18.1	18.9	13.8	19.2	19.7	11.8	2.0
10.2	9.2	8.8	7.9	7.8	9.2	9.4	5.2	0.2
5.1	8.2	8.5	6.4	4.5	6.5	6.9	3.8	0.3

Furthermore, gel strength measurements were conducted. As depicted in Figure 57, the mixture with a ratio of 25/75 (geopolymer/spacer) unexpectedly exhibited higher 10-s and 10-min gel strengths. It is hypothesized that the high pH of the geopolymer accelerates the gelation of the spacer, which contains a notable amount of GGBFS. Gelation can potentially complicate the pumping process or lead to high friction pressure, which is undesirable as it may cause damage to the formation.

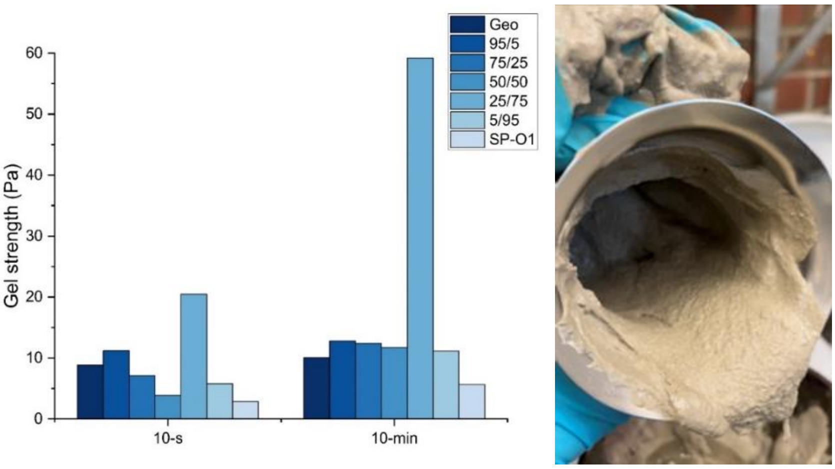

Figure 57 : (Left) API gel strength of the mixtures of geopolymer and spacer at 50℃ (Right) strong gel observed for 25/75 mixture (Paper III)

5.2.6.2 Impact of Spacer Contamination on Mechanical Properties of Geopolymer

The compressive strength of geopolymer when contaminated with 10 and 20 % (by volume of geopolymer) spacer was measured after 1 and 7 days of curing at 70°C BHST. Three spacer mix designs (Table 19) with different solid/water and granite/GGBFS ratios were investigated (Table 7). The findings indicate that the spacer with a higher content of GGBFS (SP-O2), had a slightly lower impact on the compressive strength of the geopolymer compared to SP-O1 (Figure 58). When contaminated with 10% SP-O2, the compressive strength of the geopolymer was decreased from approximately 6 MPa to less than 3 MPa after one day of curing. In comparison, contamination with 10% SP-O1 reduced the strength to approximately 2 MPa. This difference in performance can be attributed to the reactive nature of GGBFS, which serves as a source of calcium, facilitating chemical binding of water in the geopolymer matrix [21, 50]. The tensile strength of the geopolymer contaminated with spacer is illustrated in Figure 59. After one day, the tensile strength of the geopolymer was decreased from approximately 0.5 MPa to less than 0.35 MPa and 0.25 MPa with 10% contamination by SP-O2 and SP-O1, respectively.

Table 19 : Spacer mix designs for compatibility study

Component	SP-O1	SP-O2	SP-O3
Water	300	300	150
NaCl	9	9	9
Na_2CO_3	6	6	6
GGBFS	194	294	194
Granite	100	0	100
KOH solution(12M)	10	10	10
Potassium silicate solution	20	20	20
PAC-RE	0.5	0.5	0.5
Xanthan gum	1	1	1
Surfactant	25	25	25

The comparison between the SP-O1 and SP-O3 spacer designs reveals a notable enhancement in both compressive and tensile strength of the contaminated geopolymer over one and seven days of curing. This improvement is attributed to the higher solid/water ratio in the SP-O3 design, indicating the importance of optimizing this ratio for enhancing the mechanical properties of the geopolymer if intermixture happens. The water content significantly influences the strength of the geopolymer, and exceeding a threshold water-to-solid ratio may lead to complete deterioration of the strength [77, 78]. Water primarily serves as a reaction medium, and the geopolymerization process may generate additional water, which, combined with the initial mixing water, is present in the form of evaporable water within small pores [23]. Hence, careful monitoring of the water content of the spacer fluid is essential.

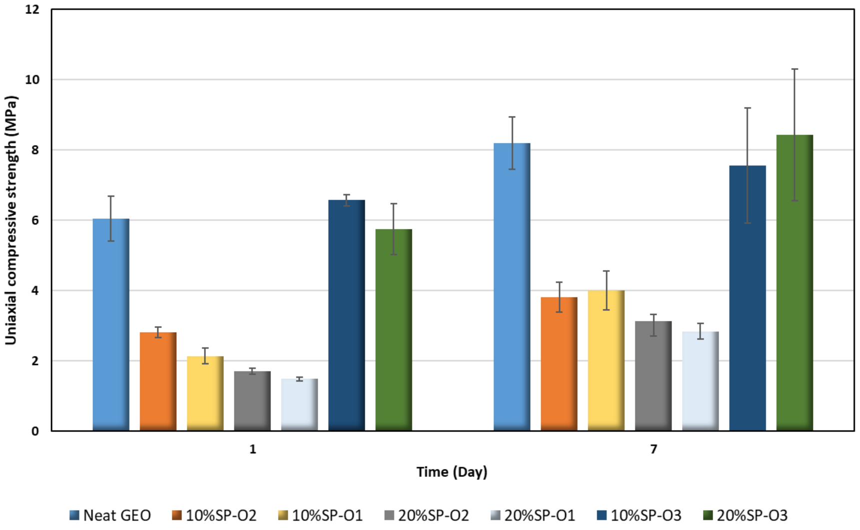

Figure 58 : UCS of geopolymer mixed with different designs of spacer (Paper III)

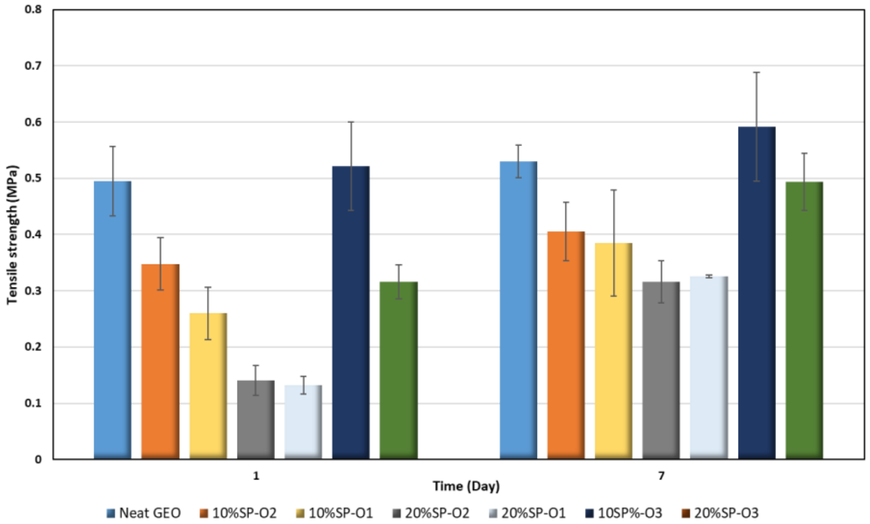

Figure 59 : Tensile strength of geopolymer mixed with different designs of spacer (Paper III)

5.2.6.3 Impact of Spacer Contamination on Crystallography

Phase changes provide a valuable opportunity to analyse alterations in the mineralogy of geopolymer material and examine the formation of new components. These changes can have a significant impact on the properties of mix designs, potentially enhancing or deteriorating their performance. Figure 60 illustrates the XRD patterns of the seven days cured samples of both neat geopolymer and geopolymer contaminated with spacer. The predominant phase in both neat and contaminated geopolymer was Quartz (Qz), attributed to the use of granite as the main solid precursor. Additionally, minor phases of albite (Alb), microcline (Mic), and biotite (Bio) were identified. Analysis of the contaminated samples did not reveal the formation of any new phases, suggesting no reaction occurred between the spacer and geopolymer to form new minerals. However, the intensity of peaks altered with spacer intermixture. Specifically, the addition of 10 and 20% SP-O1 to geopolymer increased the intensity of the quartz phase. These changes in intensity were less pronounced for the SP-O3 contamination case. The highly alkaline environment induces the dissolution of crystalline phases in the precursors, which subsequently undergo geopolymerization process and forms amorphous gels in mid-term [79]. Table shows the crystalline content of the geopolymer samples that were mixed with different spacer. It can be observed from Table 20 that geopolymer contaminated with 20% SP-O2 which had only GGBFS as precursor in the design exhibited the highest amorphous content in line with observations made by Omran et al. [79].

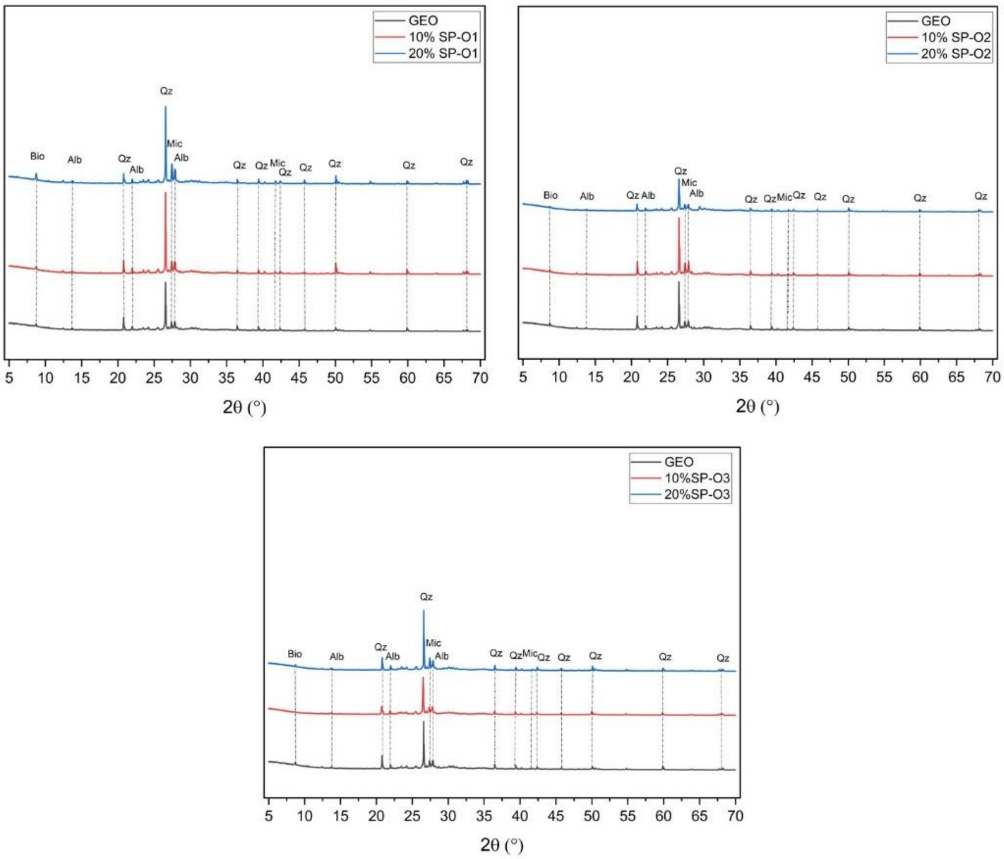

Figure 60 : XRD pattern of geopolymer mixed with different designs of spacer (Paper III)

Table 20 : Quantification of amorphous and crystalline content in geopolymer mixed with different designs of spacer based on XRD pattern

Sample	Crystalline content (wt.%)	Amorphous content (wt.%)
Neat geopolymer	65.6	34.4
10% SP-O1	66.3	33.7
20% SP-O1	69.5	30.5
10% SP-O2	67.9	32.1
20% SP-O2	63.2	36.8
10% SP-O3	66.2	33.8
20% SP-O3	65.2	34.8

5.2.6.4 Impact of Water on Kinetics of Geopolymer

After observing the impact of solid/water ratio of spacer on the mechanical strength of geopolymer, it was decided to further investigate the role of additional water on the reaction kinetics of geopolymer. Varying amounts of water, specifically 2.5% and 5% (by volume of geopolymer), were incorporated into the geopolymer slurry, and the heat evolution of these slurries was monitored. Normalized heat flow for slurries is shown in Figure 61. The first exothermic peak, observed within less than 10 minutes of initiating the reaction, is primarily attributed to the dissolution process of the solid precursor in the alkali activator. This initial stage involves the breakdown of the solid components by OH^- attack, allowing reaction products to precipitate on the surface of solid particles, resulting in the liberation of heat. However, as the amount of water in the system was increased, this exothermic peak diminished in intensity. When extra water is introduced into the mixture, the concentration of hydroxide ions in the activator solution decreases due to the dilution effect. This reduction in OH- concentration diminishes the activator's efficacy in breaking down the Si-O and Al-O bonds [67, 80, 81]. Second exothermic peak attributed to polymerization of alumina and silica species was also observed for all slurries which was after about 17 hours for neat geopolymer. When 2.5% and 5% water were introduced into the geopolymer mixture, the time taken to reach the exothermic peak increased to 23 and 32 hours, respectively. This indicates that the presence of additional water delayed the polymerization process. The intensity of the peak was also reduced with the increase in water content. During the polymerization phase, water acts as a byproduct, and an excess of it can potentially hinder the reaction kinetics [80].

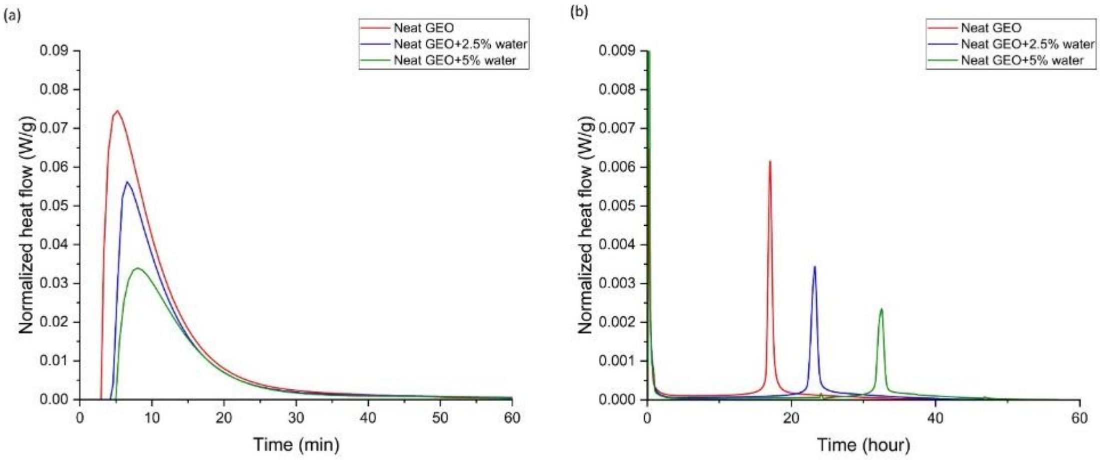

Figure 61: Heat evolution of geopolymer with extra water (a) first hour (b) total duration of test (Paper III)

5.3 Drilling Fluid Displacement and Geopolymer Placement

In previous sections, the detrimental impact of drilling fluid contamination both on the fluid state and after-setting properties were discussed. In this section, we explore the dynamics of drilling fluid displacement/placement of geopolymer in the well, highlighting the critical factors that must be comprehended to effectively manage contamination. The simulation work was conducted in collaboration with a research team from The University of British Columbia, while the input experimental data was produced by the PhD candidate. 2D-gap averaged displacement simulation was performed using one of North Sea platform wells data that had a depth of 2811 m TVD and was completed with four casings. Here, the displacement in surface and intermediate casing with setting depth of 522 m and 1374 m TVD are discussed. Table 21 provide dimensions for these casing respectively. Two different geopolymer design for these particular casings were used (Table 22). For the surface casing, spud mud, a common mud used in upper sections of the well, was chosen as the displaced fluid. In the case of intermediate casing, WBDF and OBDF were investigated as the displaced fluid (the mix design is shown in Table 4 and Table 5). Two generic spacer fluids were chosen, one exhibiting Newtonian behavior and the other showing the Power-law behavior (rheological parameters are represented in Table 23).

Table 21 : Dimensions of the casings as input for displacement simulation (Paper V)

		20’’ Surface casing	$13^{3/8}$ ’’ Intermediate casing
Hole size	$\hat{\boldsymbol{r}}_{\boldsymbol{o}}$	0.330 m	0.223 m
Casing size	$\hat{\boldsymbol{r}}_{\boldsymbol{i}}$	0.254 m	0.169 m
Mean radius	$\hat{\boldsymbol{r}}_{\boldsymbol{a}}$	0.292 m	0.1960 m
Mean half-gap width	$\hat{\boldsymbol{d}}$	0.0381 m	0.0265 m
Aspect ratio	$\boldsymbol{\delta} = \hat{\boldsymbol{d}}/\hat{\boldsymbol{r}}_{\boldsymbol{a}}$	0.130	0.1352
Inclination from the vertical	$\boldsymbol{\beta}$	0°	0°-65°
Simulated length	$\hat{\boldsymbol{\xi}}_{\boldsymbol{bh}}$	150.00 m	150.00 m

Table 22 : Mix design of geopolymer used for displacement simulation (Paper V)

Geopolymer design	Precursor	Hardener	Liquid to solid weight ratio	Target BHCT	Casing
W111	Granite-based precursor	4M KOH solution	0.434	25℃	Surface casing
W201	Granite-based precursor	Potassium silicate solution (molar ratio of 2.21)	0.506	50℃	Intermediate casing

Table 23 : Rheological parameters of fluids used as input for displacement simulation (Paper V)

	$\widehat{\boldsymbol{K}}$ (Pa · sn)	$\boldsymbol{n}$	$\hat{\boldsymbol{\tau}}_{\boldsymbol{Y}}$ (Pa)	$\hat{\boldsymbol{\rho}}$ (Kg/m3)
Newtonian spacer	0.001	1.0	0.0	-
Power-law spacer	0.35	0.50	0.0	-
Spud mud	0.126	0.6346	24.19	1150
WBDF	0.381	0.5656	0.5385	1270
OBDF	0.4975	0.5632	1.138	1160
Geopolymer (W111)	2.347	0.4955	11.9	1880
Geopolymer (W201)	0.1636	0.9824	4.118	1980

5.3.1 Displacement in the Surface Casing

Figure 62 shows the displacement scenarios in annulus where Newtonian spacer is displacing the spud mud with eccentricity of casing and density difference as variable parameters. By density difference we mean density of spacer since the density of the mud is constant. Each sub-figure in Figure 62 illustrates three time steps (t = 31, 45, 150) during the displacement process. The blue color indicates the concentration of the in-situ mud, while the red color represents the concentration of the displacing spacer. W stands for the wide side of annulus and N for narrow side. From figure, it can be noticed that density of spacer is major factor impacting the displacement efficiency. When the density difference was 5%, channelling of spacer toward the wide side is noticed irrespective of eccentricity. Increasing the density difference to 10%, with lower eccentricity (e=0.1, 0.3), the front was dispersed with more tendency toward the wide side. At higher eccentricity (e=0.6), the displacement became incomplete resulting in a layer of mud being left on the narrow side. By having higher than 20% density difference, the buoyancy force became dominate, causing a stable front and complete displacement even at higher eccentricities. Figure 63 shows displacement of spud mud by Power-law spacer. There wasn't a significant difference in this scenario compared to the Newtonian spacer, suggesting that the influence of viscous forces is less significant compared to buoyancy forces.

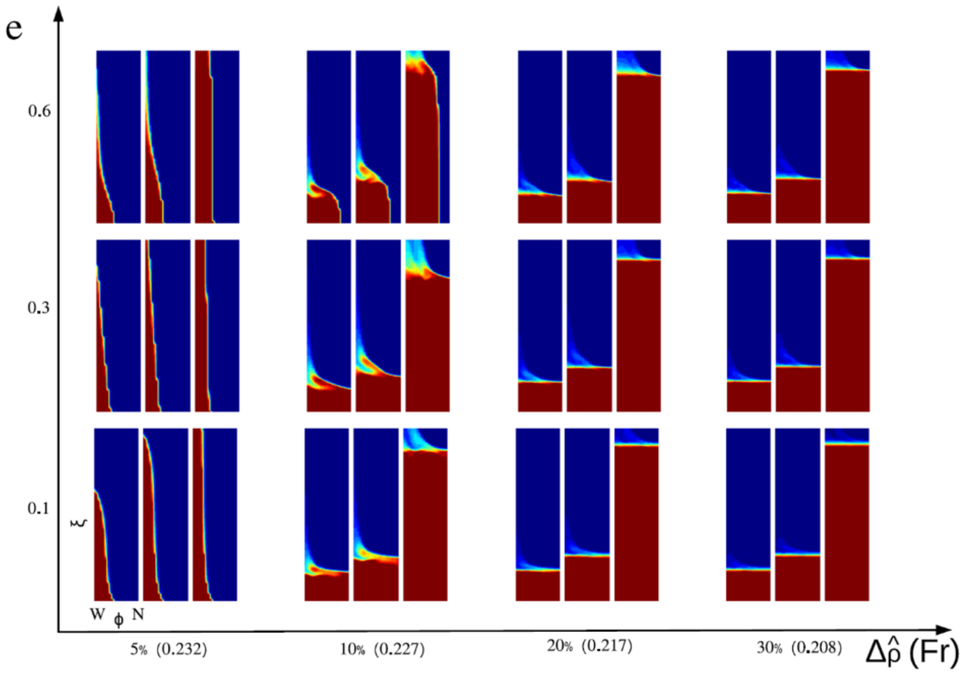

Figure 62 : Displacement of spud mud by Newtonian spacer fluid in surface casing. Horizontal axis represents density difference and vertical axis represents eccentricity (Paper V)

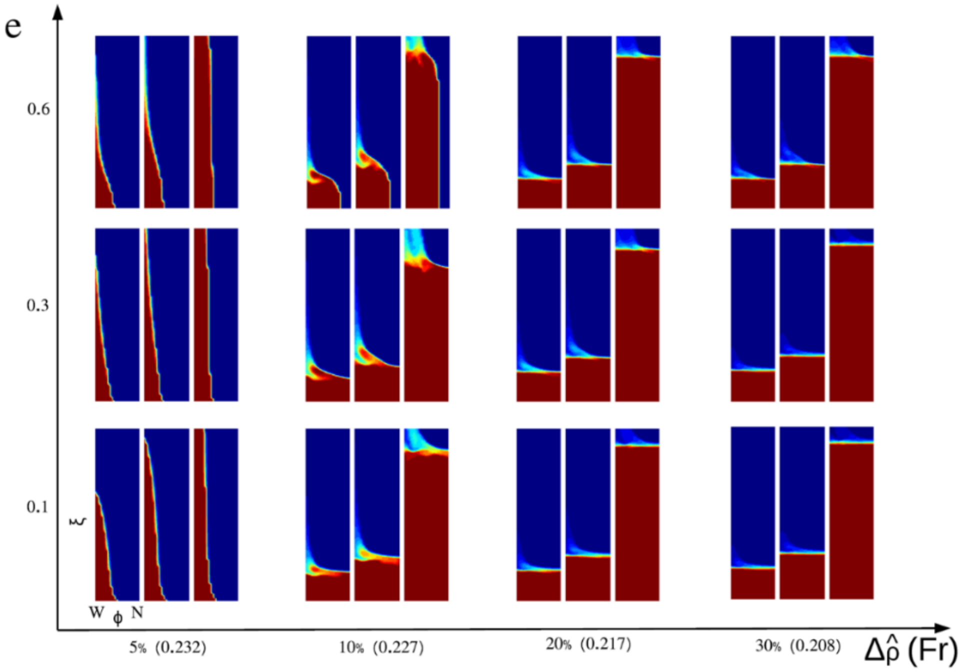

Figure 63 : Displacement of spud mud by Power-law spacer fluid in surface casing. Horizontal axis represents density difference and vertical axis represents eccentricity (Paper V)

5.3.2 Displacement in the Intermediate Casing

The Figure 64 depicts the displacement process in the intermediate casing, where a Newtonian spacer is displacing eighter WBDF or OBDF with a density difference of 5% and an eccentricity of e=0.6, followed by the final fluid, which is geopolymer. Irrespective of the type of the mud, the flow was inclined to wide side of the annulus and increased the volume of spacer/drilling fluid subjected to mixing. Channeling was more severe when OBDF is displaced fluid due to higher viscosity ratio between fluids. Figure 64 also shows the displacement in the annulus where Power-law spacer was used. This fluid had slightly better performance in removing the WBDF from annulus, although channeling of OBDF still was a problem. Despite the fact that channeling of spacer in drilling fluid column happened when the density difference was low between them, the high density of geopolymer helped to effectively remove the remaining fluids.

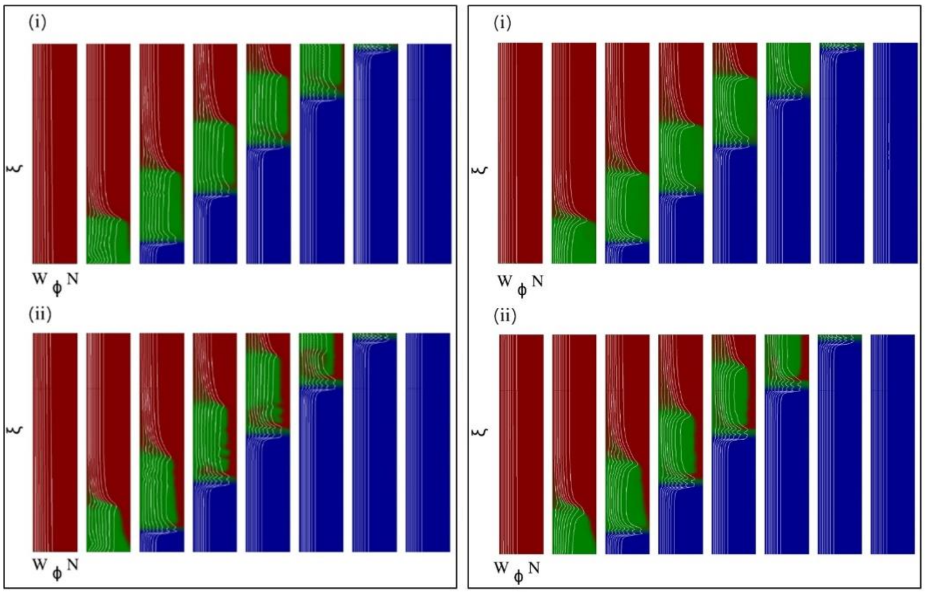

Figure 64 : (Left) Displacement of (i) WBDF and (ii) OBDF by Newtonian spacer (green) and geopolymer (blue) (Right) Displacement of (i) WBDF and (ii) OBDF by Power-law spacer (green) and geopolymer (blue) (Paper V)

Figure 65 provides a displacement map at high eccentricity of 0.8 with inclination of the well and flow rate as variable parameters. As the inclination increased and, to a lesser extent, with higher flow rates, the effectiveness of the spacer in displacing the narrow side diminished. This increased the chance of geopolymer contamination in the narrow side.

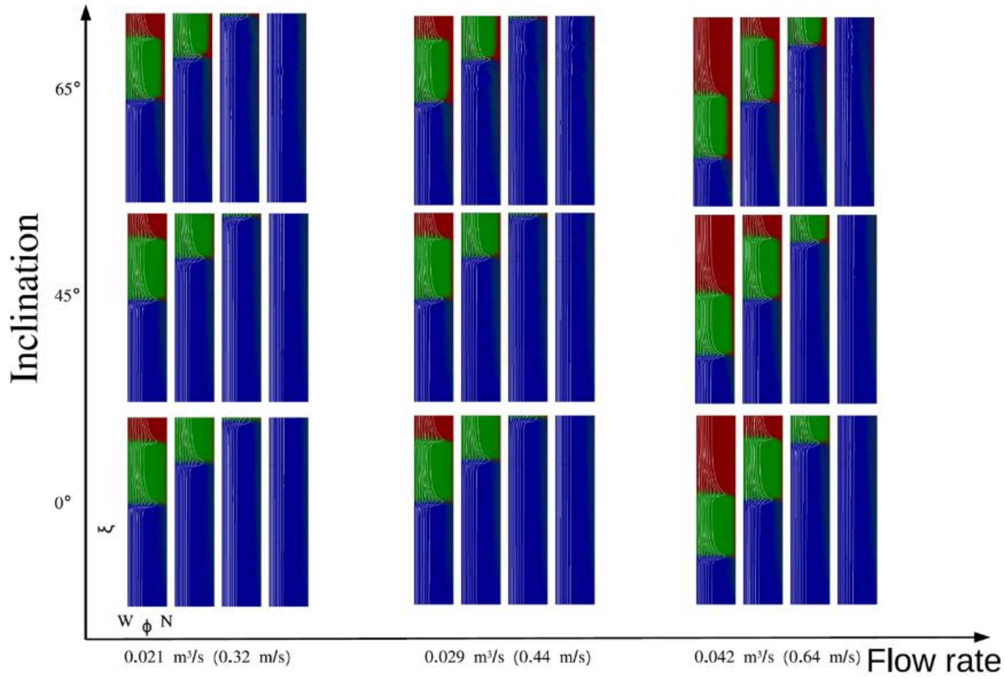

Figure 65 : Displacement of WBDF by spacer fluid in intermediate casing. Horizontal axis represents flow rate and vertical axis represents inclination of the well (Paper V)

6. Summary and Conclusions

6.1 Summary

Drilling fluid contamination of the rock-based geopolymer has been discussed. The fluid-state and solid-state properties of the geopolymer when contaminated with water-based drilling fluid (WBDF) and oil-based drilling fluid (OBDF) were investigated. The fluids exhibited different degree of contamination. The contamination mechanism by WBDF and OBDF was also discussed with the help of available tools and analysing the morphology, mineralogy, and kinetics of reaction.

Spacer fluids are essential part of cementing program by removing drilling fluid from annulus and cleaning and water-wetting of surface of casing and formation. They also minimize the contact of geopolymer, and mud given that displacement of mud by spacer is successful. After observing the poisonous impact of the drilling fluids on the UCS and tensile strength of the geopolymer, we developed a spacer fluid with the ability to harden. This characteristic may improve the wellbore integrity by providing a complementary material on top of the zonal isolation barrier material. The spacer design process consists of two stages of i) tuning the rheological parameters using rheology modifiers such as xanthan gum, PAC and bentonite ii) optimizing the surfactant content to clean the surface of casing. Finally, the compatibility test of optimized spacer/ drilling fluid and geopolymer/optimized spacer were performed.

Finally, the displacement of fluids in annular space were discussed. Several scenarios of drilling fluid being displaced by spacer and geopolymer in the surface and intermediate casing condition were simulated. The under investigated factors were density difference, eccentricity of casing, inclination, flow behavior of spacer and flow rate. The results provide key insight into best practices to avoid channelling and subsequent contamination of geopolymer in the annulus.

6.2 Conclusion

The following conclusions are made from this work:

- The presence of WBDF has a more pronounced impact on the geopolymer mechanical properties compared to presence of OBDF. Specifically, when exposed to WBDF, both the compressive and tensile strength of the geopolymer is significantly reduced to a greater degree than when exposed to OBDF.
- When the geopolymer was mixed with OBDF, microstructure analysis of the cured samples revealed the formation of voids within the geopolymer matrix. This phenomenon is attributed to the ability of the geopolymer to disperse and stabilize oil droplets.
- The oil droplets inclusion in the geopolymer slurry from OBDF forms a o/w emulsion, resulting in higher shear stress at higher shear rates compared to neat geopolymer and vice versa at lower shear rates.
- SEM images of the WBDF contaminated geopolymer revealed very loose network of gel formed in the matrix causing a compromised mechanical strength.
- It is important to design a compatible spacer fluid for the geopolymer considering harmful impact of drilling fluids.
- It was verified that Xanthan gum had more pronounced impact on the flow behavior index and yield stress of spacer compared to PAC.
- Non-ionic surfactant proved to be effective in the hardening spacer by enhancing rotor cleaning efficiency and improving the water wetting of the casing.
- A higher solid to water ratio in the hardening spacer correlates with increased compressive and tensile strength of the contaminated geopolymer.

- The excessive water from spacer and WBDF will reduce the dissolution and polymerization rate as indicated in heat evolution of the geopolymer.
- In the upper sections of the well, having a spacer-mud density difference for example higher than 20% helps creating more efficient displacement even in eccentric geometry.
- The high density of the geopolymer may benefit displacements in annulus of vertical and relatively inclined wells. It offers a wide density range for spacer design and generates necessary buoyancy for mud and spacer removal from narrow wellbore sides.

7. Recommendations

Full replacement of OPC in primary cementing and P&A by the geopolymer requires careful consideration of various aspects, including operational, technical, and engineering factors. Drilling fluid contamination is a major factor, impacting the quality of the geopolymer as well barrier. Improving displacement success should receive much attention as it is a major cause of the former problem. This study suggests the following recommendations:

- We studied the impact of two types of drilling fluids that are typical of North Sea operations on the geopolymer. Considering the various designs of WBDF and OBDF used worldwide, the compatibility study should be performed case by case before cementing job.
- Through thermochemistry analysis we found out that the water is blameable for hindering the geopolymerization reaction. This means that much attention should be paid when geopolymer is going to displace the WBDF in a particular section. Thus, optimizing the displacement process becomes even more fundamental. Moreover, the spacer should have the minimum functional level of water in the design.
- We also developed a spacer with components that allows it to harden. Although this feature can be beneficial to well integrity, it comes with operational and technical challenges. Future research can be directed toward setting time optimization and sealability. It is also interesting to investigate the possibility of mixing this spacer on the fly using the cement mixing tank. In this way, the spacer can be pumped just before the cement and avoid the long waiting time that can lead to the spacer being set in the tank.
- The geopolymer placement in annulus of top section with 2D simulation were covered in this study. Future research could

study the displacement in complex geometries such as enlarged borehole or horizontal sections to minimize the risk of utilizing a new material.

8. References

[1] *Well integrity in drilling and well operations*, Standard_Norway, 2021.

[2] B. Vignes, "Contribution to well integrity and increased focus on well barriers from a life cycle aspect," 2011.

[3] R. J. Davies *et al.*, "Oil and gas wells and their integrity: Implications for shale and unconventional resource exploitation," *Marine and Petroleum Geology*, vol. 56, pp. 239-254, 2014/09/01/ 2014, doi: 10.1016/j.marpetgeo.2014.03.001.

[4] O. A. Omosebi, M. Sharma, R. M. Ahmed, S. N. Shah, A. Saasen, and S. O. Osisanya, "Cement Degradation in CO2 - H2S Environment under High Pressure-High Temperature Conditions," in *SPE Bergen One Day Seminar*, 2017, vol. Day 1 Wed, April 05, 2017, D012S009R005, doi: 10.2118/185932-ms. [Online]. Available: https://doi.org/10.2118/185932-MS

[5] C. E. Agostini *et al.*, "Thermal Shock Transient Analysis for Well Integrity Through Operational Envelope," in *Offshore Technology Conference*, 2020, vol. Day 2 Tue, May 05, 2020, D022S002R002, doi: 10.4043/30719-ms. [Online]. Available: https://doi.org/10.4043/30719-MS

[6] Y. Zheng, B. Xu, J. Pu, N. Mu, B. Wang, and M. Li, "Mechanical behaviors of cement systems in different conditions," *Natural Gas Industry B*, vol. 4, no. 3, pp. 212-216, 2017/05/01/ 2017, doi: https://doi.org/10.1016/j.ngib.2017.07.022.

[7] R. Kimanzi, Y. Wu, S. Salehi, M. Mokhtari, and M. Khalifeh, "Experimental Evaluation of Geopolymer, Nano-Modified, and Neat Class H Cement by Using Diametrically Compressive Tests," *Journal of Energy Resources Technology*, vol. 142, no. 9, 2020, doi: 10.1115/1.4046702.

[8] B. Li, H. Li, F. Zhou, B. Guo, and X. Chang, "Effect of cement sheath induced stress on well integrity assessment in carbon sequestration fields," *Journal of Natural Gas Science and Engineering*, vol. 46, pp. 132-142, 2017/10/01/ 2017, doi: https://doi.org/10.1016/j.jngse.2017.07.014.

[9] M. Loizzo, O. A. P. A. P. Akemu, L. Jammes, J. Desroches, S. Lombardi, and A. Annunziatellis, "Quantifying the Risk of CO2

Leakage Through Wellbores," *SPE Drilling & Completion*, vol. 26, no. 03, pp. 324-331, 2011, doi: 10.2118/139635-pa.

[10] B. Miyazaki, D. J. Evans, and R. A. Chadwick, "Well integrity: An overlooked source of risk and liability for underground natural gas storage. Lessons learned from incidents in the USA," in *Underground Gas Storage: Worldwide Experiences and Future Development in the UK and Europe*, vol. 313: Geological Society of London, 2009, p. 0.

[11] D. Barreda, M. P. Shahri, R. Wagner, and G. King, "Impact of Cyclic Pressure Loading on Well Integrity in Multi-Stage Hydraulic Fracturing," in *SPE/AAPG/SEG Unconventional Resources Technology Conference*, 2018, vol. Day 2 Tue, July 24, 2018, D023S049R002, doi: 10.15530/urtec-2018-2902463. [Online]. Available: https://doi.org/10.15530/URTEC-2018-2902463

[12] E. B. Nelson and D. Guillot, *Well Cementing*. Schlumberger, 2006.

[13] T. Sasaki, K. Soga, and M. Abuhaikal, "Water absorption and shrinkage behaviour of early-age cement in wellbore annulus," *Journal of Petroleum Science and Engineering*, vol. 169, pp. 205-219, 2018/10/01/ 2018, doi: https://doi.org/10.1016/j.petrol.2018.05.065.

[14] M. Geiker and T. Knudsen, "Chemical shrinkage of portland cement pastes," *Cement and Concrete Research*, vol. 12, no. 5, pp. 603-610, 1982/09/01/ 1982, doi: https://doi.org/10.1016/0008-8846(82)90021-7.

[15] T. Vrålstad, A. Saasen, E. Fjær, T. Øia, J. D. Ytrehus, and M. Khalifeh, "Plug & abandonment of offshore wells: Ensuring long-term well integrity and cost-efficiency," *Journal of Petroleum Science and Engineering*, vol. 173, pp. 478-491, 2019/02/01/ 2019, doi: https://doi.org/10.1016/j.petrol.2018.10.049.

[16] M. B. Dusseault, M. N. Gray, and P. A. Nawrocki, "Why Oilwells Leak: Cement Behavior and Long-Term Consequences," in *International Oil and Gas Conference and Exhibition in China*, 2000, vol. All Days, SPE-64733-MS, doi: 10.2118/64733-ms. [Online]. Available: https://doi.org/10.2118/64733-MS

[17] A. A. Soares *et al.*, "Cement slurry contamination with oil-based drilling fluids," *Journal of Petroleum Science and Engineering,* vol. 158, pp. 433-440, 2017/09/01/ 2017, doi: https://doi.org/10.1016/j.petrol.2017.08.064.

[18] E. Benhelal, G. Zahedi, E. Shamsaei, and A. Bahadori, "Global strategies and potentials to curb CO2 emissions in cement industry," *Journal of Cleaner Production,* vol. 51, pp. 142-161, 2013/07/15/ 2013, doi: https://doi.org/10.1016/j.jclepro.2012.10.049.

[19] J. Davidovits, "Geopolymers," *Journal of thermal analysis,* vol. 37, no. 8, pp. 1633-1656, 1991/08/01 1991, doi: 10.1007/BF01912193.

[20] M. Khalifeh, H. Hodne, A. Saasen, O. Integrity, and E. I. Eduok, "Usability of Geopolymers for Oil Well Cementing Applications: Reaction Mechanisms, Pumpability, and Properties," in *SPE Asia Pacific Oil & Gas Conference and Exhibition*, 2016, vol. All Days, SPE-182354-MS, doi: 10.2118/182354-ms. [Online]. Available: https://doi.org/10.2118/182354-MS

[21] J. L. Provis and S. A. Bernal, "Geopolymers and Related Alkali-Activated Materials," *Annual Review of Materials Research,* vol. 44, no. 1, pp. 299-327, 2014, doi: 10.1146/annurev-matsci-070813-113515.

[22] P. Duxson, A. Fernández-Jiménez, J. L. Provis, G. C. Lukey, A. Palomo, and J. S. J. van Deventer, "Geopolymer technology: the current state of the art," *Journal of Materials Science,* vol. 42, no. 9, pp. 2917-2933, 2007/05/01 2007, doi: 10.1007/s10853-006-0637-z.

[23] S. Park and M. Pour-Ghaz, "What is the role of water in the geopolymerization of metakaolin?," *Construction and Building Materials,* vol. 182, pp. 360-370, 2018/09/10/ 2018, doi: https://doi.org/10.1016/j.conbuildmat.2018.06.073.

[24] J. L. Provis, "Geopolymers and other alkali activated materials: why, how, and what?," *Materials and Structures,* vol. 47, no. 1, pp. 11-25, 2014/01/01 2014, doi: 10.1617/s11527-013-0211-5.

[25] A. Bonett and D. Pafitis, "Getting to the Root of Gas Migration," Schlumberger, 1996.

[26] H. K. J. Ladva, B. Craster, T. G. J. Jones, G. Goldsmith, and D. Scott, "The Cement-to-Formation Interface in Zonal Isolation,"

SPE Drilling & Completion, vol. 20, no. 03, pp. 186-197, 2005, doi: 10.2118/88016-pa.

[27] D. J. Guillot, J. Desroches, and I. Frigaard, "Are Preflushes Really Contributing to Mud Displacement During Primary Cementing?," in *SPE/IADC Drilling Conference*, 2007, vol. All Days, SPE-105903-MS, doi: 10.2118/105903-ms. [Online]. Available: https://doi.org/10.2118/105903-MS

[28] C. F. Lockyear and A. P. Hibbert, "Integrated Primary Cementing Study Defines Key Factors for Field Success," *Journal of Petroleum Technology*, vol. 41, no. 12, pp. 1320-1325, 1989, doi: 10.2118/18376-pa.

[29] M. Couturler, D. Guillot, H. Hendriks, and F. Callet, "Design Rules And Associated Spacer Properties For Optimal Mud Removal In Eccentric Annuli," presented at the CIM/SPE International Technical Meeting, Calgary, Alberta, June 1990, 1990. [Online]. Available: https://doi.org/10.2118/21594-MS.

[30] S. R. Keller, R. J. Crook, R. C. Haut, and D. S. Kulakofaky, "Deviated-Wellbore Cementing: Part 1 - Problems," *Journal of Petroleum Technology*, vol. 39, no. 08, pp. 955-960, 1987, doi: 10.2118/11979-pa.

[31] S. H. Bittleston, J. Ferguson, and I. A. Frigaard, "Mud removal and cement placement during primary cementing of an oil well – Laminar non-Newtonian displacements in an eccentric annular Hele-Shaw cell," *Journal of Engineering Mathematics*, vol. 43, no. 2, pp. 229-253, 2002/08/01 2002, doi: 10.1023/A:1020370417367.

[32] S. Pelipenko and I. A. Frigaard, "On steady state displacements in primary cementing of an oil well," *Journal of Engineering Mathematics*, 2004.

[33] S. H. Bittleston and D. Guillot, "Mud removal: Research improves traditional cementing guidelines," Netherlands, 1991.

[34] D. H. O. S. O. National Commission on the B. P. , Drilling, "Deep water : the Gulf oil disaster and the future of offshore drilling : report to the President," [Washington, D.C.] : National Commission on the BP Deepwater Horizon Oil Spill and Offshore Drilling : For sale by the Supt. of Docs., U.S. G.P.O., [2011], 2011. [Online]. Available: https://search.library.wisc.edu/catalog/9910099441602121

[35] M. Allouche, I. A. Frigaard, and G. Sona, "Static wall layers in the displacement of two visco-plastic fluids in a plane channel," *Journal of Fluid Mechanics*, vol. 424, pp. 243-277, 2000, doi: 10.1017/S0022112000001956.

[36] K. M. Ravi, R. M. Beirute, and R. L. Covington, "Erodability of Partially Dehydrated Gelled Drilling Fluid and Filter Cake," in *SPE Annual Technical Conference and Exhibition*, 1992, vol. All Days, SPE-24571-MS, doi: 10.2118/24571-ms. [Online]. Available: https://doi.org/10.2118/24571-MS

[37] A. Saasen, B. Lund, and J. D. Ytrehus, "Theoretical Basis for Prediction of Drilling Fluid Removal in Annuli," in *ASME 2017 36th International Conference on Ocean, Offshore and Arctic Engineering*, 2017, vol. Volume 8: Polar and Arctic Sciences and Technology; Petroleum Technology, V008T11A058, doi: 10.1115/omae2017-61030. [Online]. Available: https://doi.org/10.1115/OMAE2017-61030

[38] M. Kremieniewski, M. Kędzierski, and S. Błaż, "Increasing the Efficiency of Sealing the Borehole in Terms of Spacer Pumping Time," *Energies*, vol. 14, no. 20, p. 6702, 2021. [Online]. Available: https://www.mdpi.com/1996-1073/14/20/6702.

[39] K. B. Jiménez, "Characterization of annulus well cement quality to estimate the leakage potential in cement well barriers," PhD, University of Stavanger, Stavanger 2022.

[40] Abdel-Alim and H. El-Sayed, "Effect of Drilling Muds Contamination on Cement Slurry Properties," presented at the Fourth Saudi Engineering Conference, Jeddah, Saudi Arabia, 5–8 November, 1995.

[41] M. Li, H. Ou, Z. Li, T. Gu, H. Liu, and X. Guo, "Contamination of cement slurries with diesel-based drilling fluids in a shale gas well," *Journal of Natural Gas Science and Engineering*, vol. 27, pp. 1312-1320, 2015/11/01/ 2015, doi: 10.1016/j.jngse.2015.08.010.

[42] E. Eid, H. Tranggono, M. Khalifeh, S. Salehi, and A. Saasen, "Impact of Drilling Fluid Contamination on Performance of Rock-Based Geopolymers," *SPE Journal*, vol. 26, no. 06, pp. 3626-3633, 2021, Art no. SPE-205477-PA, doi: 10.2118/205477-pa.

[43] A. Katende, Y. Lu, A. Bunger, and M. Radonjic, "Experimental quantification of the effect of oil based drilling fluid contamination on properties of wellbore cement," *Journal of Natural Gas Science and Engineering*, vol. 79, p. 103328, 2020/07/01/ 2020, doi: https://doi.org/10.1016/j.jngse.2020.103328.

[44] K. Aughenbaugh, S. Nair, M. Cowan, and E. van Oort, "Contamination of Deepwater Well Cementations by Synthetic-Based Drilling Fluids," in *SPE Deepwater Drilling and Completions Conference*, 2014, vol. Day 1 Wed, September 10, 2014, D011S003R003, doi: 10.2118/170325-ms. [Online]. Available: https://doi.org/10.2118/170325-MS

[45] X. Cheng, K. Liu, X. Zhang, Z. Li, and X. Guo, "Integrity changes of cement sheath due to contamination by drilling fluid," *Advances in Cement Research*, vol. 30, no. 2, pp. 47-55, 2018, doi: 10.1680/jadcr.16.00121.

[46] N. Opedal, J. Todorovic, M. Torsæter, T. Vrålstad, and W. Mushtaq, "Experimental Study on the Cement-Formation Bonding," presented at the SPE International Symposium and Exhibition on Formation Damage Control, Lafayette, Louisiana, USA, February, 2014. [Online]. Available: https://doi.org/10.2118/168138-MS.

[47] L. G. Carter and G. W. Evans, "A Study of Cement-Pipe Bonding," *Journal of Petroleum Technology*, vol. 16, no. 02, pp. 157-160, 1964, doi: 10.2118/764-pa.

[48] S. Saha and C. Rajasekaran, "Enhancement of the properties of fly ash based geopolymer paste by incorporating ground granulated blast furnace slag," *Construction and Building Materials*, vol. 146, pp. 615-620, 2017/08/15/ 2017, doi: https://doi.org/10.1016/j.conbuildmat.2017.04.139.

[49] P. Nath and P. K. Sarker, "Effect of GGBFS on setting, workability and early strength properties of fly ash geopolymer concrete cured in ambient condition," *Construction and Building Materials*, vol. 66, pp. 163-171, 2014/09/15/ 2014, doi: https://doi.org/10.1016/j.conbuildmat.2014.05.080.

[50] C. K. Yip, G. C. Lukey, and J. S. J. van Deventer, "The coexistence of geopolymeric gel and calcium silicate hydrate at the early stage of alkaline activation," *Cement and Concrete*

Research, vol. 35, no. 9, pp. 1688-1697, 2005/09/01/ 2005, doi: https://doi.org/10.1016/j.cemconres.2004.10.042.

[51] C. K. Yip, G. C. Lukey, J. L. Provis, and J. S. J. van Deventer, "Effect of calcium silicate sources on geopolymerisation," *Cement and Concrete Research*, vol. 38, no. 4, pp. 554-564, 2008/04/01/ 2008, doi: https://doi.org/10.1016/j.cemconres.2007.11.001.

[52] C. D. Lawrence, "4 - The Constitution and Specification of Portland Cements," in *Lea's Chemistry of Cement and Concrete (Fourth Edition)*, P. C. Hewlett Ed. Oxford: Butterworth-Heinemann, 1998, pp. 131-193.

[53] I. Garcia-Lodeiro, A. Palomo, and A. Fernández-Jiménez, "2 - An overview of the chemistry of alkali-activated cement-based binders," in *Handbook of Alkali-Activated Cements, Mortars and Concretes*, F. Pacheco-Torgal, J. A. Labrincha, C. Leonelli, A. Palomo, and P. Chindaprasirt Eds. Oxford: Woodhead Publishing, 2015, pp. 19-47.

[54] M. Grinrod, B. Vassoy, and E. O. Dingsoyr, "Development and Use of a Gas-Tight Cement," in *IADC/SPE Drilling Conference*, 1988, vol. All Days, SPE-17258-MS, doi: 10.2118/17258-ms. [Online]. Available: https://doi.org/10.2118/17258-MS

[55] F. Chamssine, "Instituting Retarders for Geopolymers Developed for Downhole Applications," PhD, Faculty of Science and Technology Institute of Energy and Petroleum Engineering, University of Stavanger, 2023.

[56] *API RP 10B-2, Recommended Practice for Testing Well Cements*, A. P. Institute, 2013.

[57] *Standard Test Method for Splitting Tensile Strength of Intact Rock Core Specimens.*, A. American Society for Testing and Materials, 2016.

[58] *MECHANICAL BEHAVIOR OF CEMENT API TR 10TR7*, A. P. Institute, 2017.

[59] B. E. Théron, D. Bodin, and J. Fleming, "Optimization of Spacer Rheology Using Neural Network Technology," in *IADC/SPE Drilling Conference*, 2002, vol. All Days, SPE-74498-MS, doi: 10.2118/74498-ms. [Online]. Available: https://doi.org/10.2118/74498-MS

[60] H. A. Barnes, J. F. Hutton, and K. Walters, *An introduction to rheology*, First ed. Netherlands: Elsevier, 1989.

[61] N. Roussel, G. Ovarlez, S. Garrault, and C. Brumaud, "The origins of thixotropy of fresh cement pastes," *Cement and Concrete Research*, vol. 42, no. 1, pp. 148-157, 2012/01/01/ 2012, doi: https://doi.org/10.1016/j.cemconres.2011.09.004.

[62] A. Saasen and J. D. Ytrehus, "Viscosity Models for Drilling Fluids—Herschel-Bulkley Parameters and Their Use," *Energies*, vol. 13, no. 20, p. 5271, 2020. [Online]. Available: https://www.mdpi.com/1996-1073/13/20/5271.

[63] D. Medpelli, J.-M. Seo, and D.-K. Seo, "Geopolymer with Hierarchically Meso-/Macroporous Structures from Reactive Emulsion Templating," *Journal of the American Ceramic Society*, vol. 97, no. 1, pp. 70-73, 2014, doi: https://doi.org/10.1111/jace.12724.

[64] M. S. Cilla, M. D. de Mello Innocentini, M. R. Morelli, and P. Colombo, "Geopolymer foams obtained by the saponification/peroxide/gelcasting combined route using different soap foam precursors," *Journal of the American Ceramic Society*, vol. 100, no. 8, pp. 3440-3450, 2017, doi: https://doi.org/10.1111/jace.14902.

[65] C. Reeb, C. Pierlot, C. Davy, and D. Lambertin, "Incorporation of organic liquids into geopolymer materials - A review of processing, properties and applications," *Ceramics International*, vol. 47, no. 6, pp. 7369-7385, 2021/03/15/ 2021, doi: https://doi.org/10.1016/j.ceramint.2020.11.239.

[66] C. Shi and R. L. Day, "A calorimetric study of early hydration of alkali-slag cements," *Cement and Concrete Research*, vol. 25, no. 6, pp. 1333-1346, 1995/08/01/ 1995, doi: https://doi.org/10.1016/0008-8846(95)00126-W.

[67] X. Yao, Z. Zhang, H. Zhu, and Y. Chen, "Geopolymerization process of alkali–metakaolinite characterized by isothermal calorimetry," *Thermochimica Acta*, vol. 493, no. 1, pp. 49-54, 2009/09/10/ 2009, doi: https://doi.org/10.1016/j.tca.2009.04.002.

[68] K. Scrivener, A. Ouzia, P. Juilland, and A. Kunhi Mohamed, "Advances in understanding cement hydration mechanisms,"

Cement and Concrete Research, vol. 124, p. 105823, 2019/10/01/ 2019, doi: https://doi.org/10.1016/j.cemconres.2019.105823.

[69] K. M. Cowan, A. H. Hale, and J. J. Nahm, "Conversion of Drilling Fluids to Cements With Blast Furnace Slag: Performance Properties and Applications for Well Cementing," presented at the SPE Annual Technical Conference and Exhibition, Washington, D.C., October 1992., 1992, SPE-24575-MS. [Online]. Available: https://doi.org/10.2118/24575-MS.

[70] A. Tehrani, J. Ferguson, and S. H. Bittleston, "Laminar Displacement in Annuli: A Combined Experimental and Theoretical Study," presented at the SPE Annual Technical Conference and Exhibition, Washington, D.C., October, 1992, 1992. [Online]. Available: https://doi.org/10.2118/24569-MS.

[71] K.-W. Song, Y.-S. Kim, and G.-S. Chang, "Rheology of concentrated xanthan gum solutions: Steady shear flow behavior," *Fibers and Polymers*, vol. 7, no. 2, pp. 129-138, 2006/06/01 2006, doi: 10.1007/BF02908257.

[72] G. Harrison, G. V. Franks, V. Tirtaatmadja, and D. V. Boger, "Suspensions and polymers - Common links in rheology," *Korea-Australia Rheology Journal*, 1999.

[73] D. Nguyen, M. Kagan, and S. S. Rahman, "Evaluation of drilling fluid removal by cement slurry from horizontal wells with the use of an accurate mathematical model," *Journal of Petroleum Science and Engineering*, vol. 8, no. 3, pp. 191-204, 1992/10/01/ 1992, doi: 10.1016/0920-4105(92)90033-W.

[74] W. Huang, Y.-K. Leong, T. Chen, P.-I. Au, X. Liu, and Z. Qiu, "Surface chemistry and rheological properties of API bentonite drilling fluid: pH effect, yield stress, zeta potential and ageing behaviour," *Journal of Petroleum Science and Engineering*, vol. 146, pp. 561-569, 2016/10/01/ 2016, doi: https://doi.org/10.1016/j.petrol.2016.07.016.

[75] J. H. Schön, "Chapter 2 - Pore Space Properties," in *Developments in Petroleum Science*, vol. 65, J. H. Schön Ed.: Elsevier, 2015, pp. 21-84.

[76] C. Reeb, C. A. Davy, C. Pierlot, M. Bertin, V. Cantarel, and D. Lambertin, "Emulsification of low viscosity oil in alkali-activated materials," *Cement and Concrete Research*, vol. 162, p.

106963, 2022/12/01/ 2022, doi: 10.1016/j.cemconres.2022.106963.

[77] M. Omran and M. Khalifeh, "Development of One-Part Rock-Based Geopolymers for Downhole Cementing Applications," *Journal of Energy Resources Technology*, vol. 145, no. 10, 2023, doi: 10.1115/1.4062250.

[78] S. Y. Oderji, B. Chen, C. Shakya, M. R. Ahmad, and S. F. A. Shah, "Influence of superplasticizers and retarders on the workability and strength of one-part alkali-activated fly ash/slag binders cured at room temperature," *Construction and Building Materials*, vol. 229, p. 116891, 2019/12/30/ 2019, doi: https://doi.org/10.1016/j.conbuildmat.2019.116891.

[79] M. Omran, S. Hjelm, M. Khalifeh, and S. Salehi, "Synthesis of sustainable one-part geopolymers for well cementing applications," *Geoenergy Science and Engineering*, vol. 227, p. 211822, 2023/08/01/ 2023, doi: https://doi.org/10.1016/j.geoen.2023.211822.

[80] Z. Zuhua, Y. Xiao, Z. Huajun, and C. Yue, "Role of water in the synthesis of calcined kaolin-based geopolymer," *Applied Clay Science*, vol. 43, no. 2, pp. 218-223, 2009/02/01/ 2009, doi: https://doi.org/10.1016/j.clay.2008.09.003.

[81] H. Xu and J. S. J. van Deventer, "The effect of alkali metals on the formation of geopolymeric gels from alkali-feldspars," *Colloids and Surfaces A: Physicochemical and Engineering Aspects*, vol. 216, no. 1, pp. 27-44, 2003/04/15/ 2003, doi: https://doi.org/10.1016/S0927-7757(02)00499-5.

Appendices

Appendix 1 – Rheological compatibility of spacer and WBDF

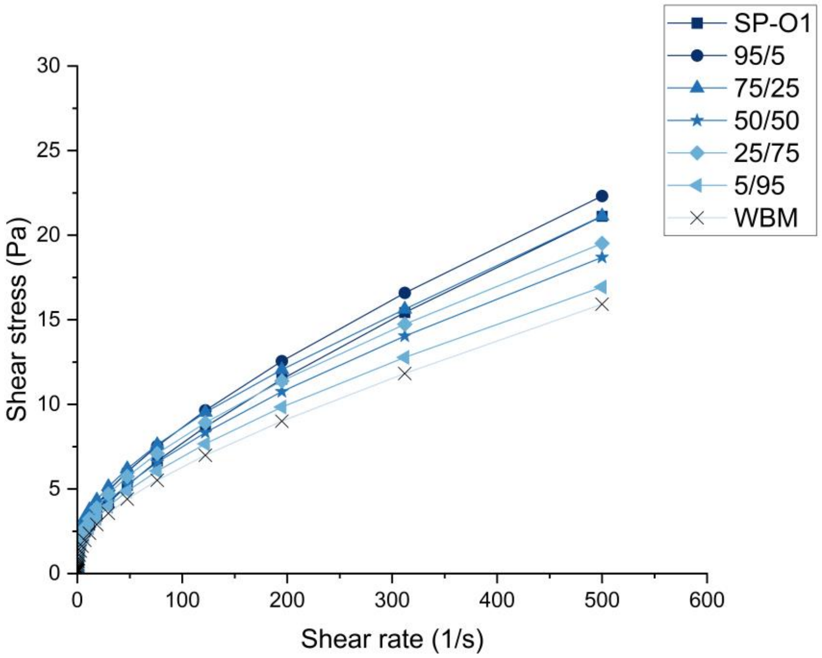

Figure 66 : Flow curve of different mixtures ratios between spacer (without surfactant) and WBDF measured at 50°C

Appendix 2 – Paper I

The Effect of Fluid Contamination on Rheological Properties of Geopolymer Materials

Pouya Khalili, Mahmoud Khalifeh, Arild Saasen

Paper OMAE2022-78994 presented at the 41th International

Conference on Ocean, Offshore and Arctic Engineering OMAE2022,

June5-10, Hamburg, Germany.

DOI: https://doi.org/10.1115/OMAE2022-78994

Appendix 3 – Paper II

The Effect of Drilling Fluid Contamination on the Properties of Granite-Based Geopolymers at Elevated Temperature

Pouya Khalili, Mahmoud Khalifeh, Arild Saasen

Paper SPE-217942-MS presented at the IADC/SPE International Drilling Conference and Exhibition, Galveston, Texas, USA, March 2024.

DOI: https://doi.org/10.2118/217942-MS

Appendix 4 – Paper III

Experimental Evaluation of Hardening Spacer for Rock-Based Geopolymer

Pouya Khalili, Mahmoud Khalifeh, Arild Saasen, Jostein Djuve,
Laurent Delabroy

Submitted to Scientific Journal, 2024

This paper is not included in the repository because it's still in review.

Appendix 5 – Paper IV

Rheological Compatibility of a Hardening Spacer Fluid and Oil-Based Drilling Fluid

Pouya Khalili, Mahmoud Khalifeh, Arild Saasen, Monica Naccache

SPE Journal

DOI: https://doi.org/10.2118/217446-PA

Rheological Compatibility of a Hardening Spacer Fluid and Oil-Based Drilling Fluid

P. Khalili[1]*, M. Khalifeh[1], A. Saasen[1], and M. Naccache[2]

[1]University of Stavanger
[2]Pontifícia Universidade Católica-RJ

Summary

In the placement process of the cement slurry, treatment fluids such as the spacer are pumped ahead of the cementitious slurry to minimize the contamination of the slurry by drilling fluid and ensure superior bonding to the casing and formation. The spacer discussed in this work can harden with time and act as a settable spacer. This characteristic can be an advantage for well integrity if some spacer pockets are left in the annulus. Rheological compatibility of different mixtures of the spacer with oil-based drilling fluid (OBDF) has been studied using a rheometer, and the resulting R-factor, which indicates the degree of compatibility between fluids, has been calculated. An increase in the flow curve was observed for the mixture of the fluids. However, based on the R-index, these fluids are compatible with displacement in the wellbore. A nonionic surfactant, typically used in conventional spacers acting as an emulsifier and a water-wetting agent, was used in the hardening spacer design. The results show that the addition of OBDF to hardening spacer containing surfactant can increase viscoelasticity. Hardening spacer containing surfactant can successfully reverse the OBDF emulsion. By performing a small-scale mud displacement experiment, we observed that surfactant can improve the wall cleaning efficiency of the spacer while having minimal impact on the bulk displacement.

Introduction

According to the study performed by Davies et al. (2014), a significant number of studied oil and gas wells worldwide experience well integrity issues. The study found that, depending on the data set being investigated, 1.9–75% of the wells were found to have such problems. Signs of inadequate zonal isolation include hydrocarbon migration and subsequent sustained casing pressure. Failing to properly remove mud and spacer from the annulus can endanger the establishment of zonal isolation with cement. Soares et al. (2017) showed that, in the event of mixing the cement with OBDF, the cement slurry thickens, even though the wetting agent used in OBDF plays a positive role in decreasing the plastic viscosity. The wetting agent alters the wettability of cement slurry particles from water-wet to oil-wet, causing retardation in the hydration process. OBDF contamination also changes the microstructure of cured Class G cement by increasing the porosity and permeability of samples (Li et al. 2016). The bond strength of cement to formation and casing is dramatically decreased when there is a film of drilling fluid on the formation and pipe surfaces (Opedal et al. 2014; Oyibo and Radonjic 2014; Santos et al. 2019; Carter and Evans 1964).

Geopolymers are a class of cementitious materials that are being developed for use in primary cementing and plug and well abandonment, with the goal of aligning with carbon reduction strategies. Although still in the developmental stage, it is expected to become an increasingly important material in the future due to its chemical and physical properties. This inorganic polymer is formed by adding the alkaline solution to a solid precursor that has a variety of aluminosilicate sources such as metakaolin, fly ash, red mud, and naturally occurring rocks (Yousefi Oderji et al. 2023). The contamination of geopolymers with drilling fluid has also been studied. According to Eid et al. (2021), water-based drilling fluid has the ability to deteriorate the compressive strength of rock-based geopolymer due to geopolymerization reaction in which water remains in the system, which differs from the hydration of cement. Water-based drilling fluid has a dilution effect and increases flowability. OBDF slightly increases the yield stress of geopolymer upon mixing at elevated temperatures (Khalili et al. 2022). A study with Class F fly ash geopolymer shows that 20% OBDF contamination can reduce the compressive strength of the material to half the initial value after 1 day of curing (Liu et al. 2019). Although the bonding of geopolymer to casing is discussed by Gomado et al. (2023), there is a gap in knowledge regarding the impact of drilling fluid on bonding. The mix design of the geopolymer is a determinant of how severe this contamination will be.

These above-mentioned results highlight the importance of efficient fluid displacement in the wellbore, which finally results in a well barrier that is capable of providing long-lasting well integrity. Important factors for proper mud removal are reducing the eccentricity of the casing inside the wellbore, characterization of fluids inside the well, and optimizing the flow rate. Using preflushes assists mud displacement and minimizes the contamination of cementitious material by drilling fluid. A spacer fluid is a type of preflush pumped ahead of cement slurry with several criteria in design such as friction pressure, density hierarchy, and rheological compatibility with drilling fluids to aid fluid displacement. Selecting a proper surfactant package as part of the spacer design is crucial because it determines the ability of fluid to erode the mudcake, to water-wet the casing and formation, and finally to invert the OBDF emulsion upon contact (Gordon et al. 2008; Nelson and Guillot 2006). Several types of spacers have been investigated in the literature. Brice and Holmes (1964) deployed a lightweight cement slurry, commonly known as scavenger, to displace the mud in turbulent flow. However, this type of slurry is not compatible with drilling fluid, and sedimentation might happen (Nelson and Guillot 2006). Carney (1974) introduced inverted emulsion as a spacer in the wellbore. Micro- and nanoemulsion spacer fluids recently enticed researchers to study them due to their ability to solubilize the oil phase in the OBDF, removing the filter cake, and altering the wettability (Curbelo et al. 2018; Wanderley Neto et al. 2020; da Silva et al. 2020; Maserati et al. 2010; Pietrangeli et al. 2015). Nevertheless, there are drawbacks associated with this type of spacer such as high cost of preparation and concerns associated with environmental impacts. There have also been efforts to turn drilling fluids into hardening material. Cowan et al. (1992) proposed adding blast furnace slag (BFS) to WBDF to convert it to cementitious

---

*Corresponding author; email: Pouya.khalili@uis.no

Original SPE manuscript received for review 19 April 2023. Revised manuscript received for review 24 July 2023. Paper (SPE 217446) peer approved 26 July 2023.

material. They concluded that conversion could improve zonal isolation with minimal effect on the properties of drilling fluid. Technical and economic aspects of mud conversion using BFS and ordinary Portland cement were evaluated by Schlemmer et al. (1994). It was concluded that the economic viability of converting mud to cement depends largely on the costs associated with disposing of used drilling mud. The application of BFS as a drilling fluid solidifier in the North Sea was discussed by Saasen et al. (1994). According to them, because of logistical difficulties, BFS is more likely to be used as an additive to the drilling fluid serving as an effective means of ensuring that the filter cake solidifies. The possibility of converting the OBDF to cement using alkali-activated fly ash was assessed by Liu et al. (2019) and it was observed that the mixture can develop notable strength.

Previous studies have examined the impact of multiple factors on drilling fluid displacement and cement placement through a combination of experimental and numerical simulation approaches. These factors include flow rate, viscosity, buoyancy, and geometric considerations. The influence of rheological properties of both the displacing and displaced fluids has been investigated in several studies (Nguyen et al. 1992; Allouche et al. 2000; Tehrani et al. 1992; Taghavi et al. 2009). The well-known study of Brice and Holmes (1964) evaluated the cement quality of 26 wells and claimed that turbulent flow improved the displacement [confirmed by the experimental work in Jakobsen et al. (1991)]. Maleki and Frigaard (2019) expressed that the degree of eccentricity and density difference between fluids are two major factors in having an efficient displacement in the annulus and a single statement cannot be made about the superiority of a particular flow regime. In addition, there have been investigations into the impact of density differences between the displacing and displaced fluids (Lockyear et al. 1990; Bu et al. 2016). Fluid displacement in the horizontal annulus (Sarmadi et al. 2021; Carrasco-Teja et al. 2008) and displacement involving a casing rotation (Carrasco-Teja and Frigaard 2009, 2010) have also been studied. However, the specific impact of surfactant in spacer design on drilling fluid displacement remains unclear and requires further investigation.

In this work, we used the geopolymerization concept to formulate a treatment fluid with low density and flexible viscosity profile that has the ability to set, leading to solidified spacer pockets that might be left in the annulus and thus contribute to zonal isolation. Additionally, the lower density of slurry yields lower hydrostatic pressure which in turn causes safer mud displacement in weak and depleted formations. The rheological compatibility of OBDF and the designed hardening spacer is evaluated. Moreover, the impact of including a nonionic surfactant in the design of the hardening spacer on rheological compatibility and displacement is also discussed.

Experimental Procedures

Materials. Table 1 shows the mix design of the spacer including the order and duration of mixing. Bentonite is used as a viscosifier and extender. Xanthan gum is used to adjust the viscosity of the spacer slurry and to maintain viscosity hierarchy with drilling fluid, meaning that the viscosity of the spacer is higher than the studied OBDF, which might lower the chance of intermixing of fluids in displacement in deviated wellbores. Granite and ground granulated blast-furnace slag (GGBFS) is used as precursor. The concentration of GGBFS and granite in the mix design can be changed to adjust the density of the slurry and early strength of the hardened spacer. The chemical composition of GGBFS and granite is shown in **Table 2.** Polyanionic cellulose was used as both fluid-loss control agent and viscosifier. Na_2CO_3, KOH (12 M), and potassium silicate solution with a Si/K molar ratio of 0.98 were used as alkaline activators. Fatty alcohol surfactant and 2-butoxyethanol solvent with a 1:1 ratio provided by a service company were used as surfactant package. An OBDF with mix design shown in **Table 3** was prepared in the laboratory. The fluids were prepared using an IKA Eurostar mixer at 1,400 1/minute rotational speed.

	Content by Weight (g)		Mixing Time (minutes)
Component	Spacer	Spacer + Surfactant Package	
Water	325	300	–
Bentonite	3	3	30
NaCl	9	9	5
Na_2CO_3	6	6	5
GGBFS	194	194	10
Granite	100	100	10
KOH solution(12 M)	10	10	5
Potassium silicate solution	20	20	5
PAC-RE	0.5	0.5	30
Xanthan gum	1	1	30
Surfactant package	–	25	5
Density (kg/m^3)	1440	1420	–

Table 1—Spacer mix design.

Chemical Element	SiO_2	Al_2O_3	Fe_2O_3	CaO	MgO	Na_2O	K_2O	Ti_2O
GGBFS (wt%)	16	6	0.2	25	7	0.4	0.8	1.8
Granite (wt%)	32	7.3	2.5	1.4	0.6	2.2	5.1	0.3

Table 2—Chemical composition of GGBFS and granite used in hardening spacer determined by X-ray fluorescence.

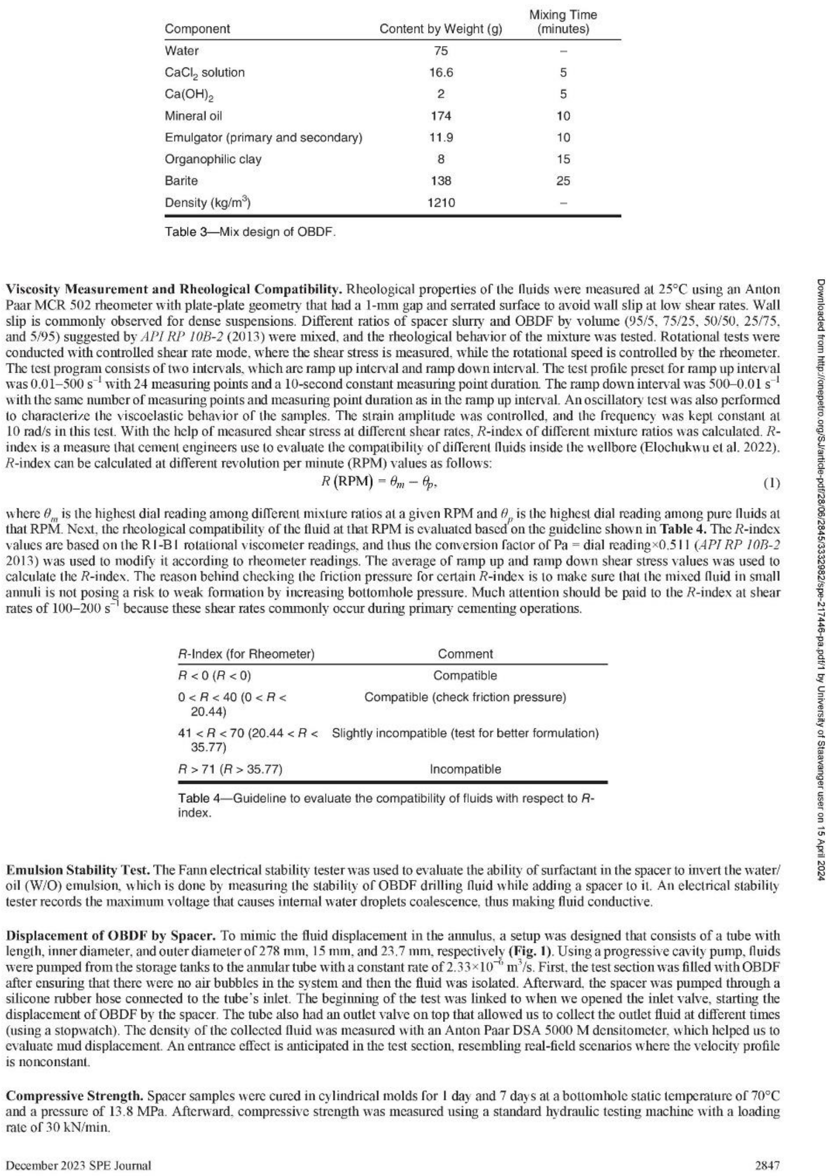

Component	Content by Weight (g)	Mixing Time (minutes)
Water	75	–
$CaCl_2$ solution	16.6	5
$Ca(OH)_2$	2	5
Mineral oil	174	10
Emulgator (primary and secondary)	11.9	10
Organophilic clay	8	15
Barite	138	25
Density (kg/m^3)	1210	–

Table 3—Mix design of OBDF.

Viscosity Measurement and Rheological Compatibility. Rheological properties of the fluids were measured at 25°C using an Anton Paar MCR 502 rheometer with plate-plate geometry that had a 1-mm gap and serrated surface to avoid wall slip at low shear rates. Wall slip is commonly observed for dense suspensions. Different ratios of spacer slurry and OBDF by volume (95/5, 75/25, 50/50, 25/75, and 5/95) suggested by *API RP 10B-2* (2013) were mixed, and the rheological behavior of the mixture was tested. Rotational tests were conducted with controlled shear rate mode, where the shear stress is measured, while the rotational speed is controlled by the rheometer. The test program consists of two intervals, which are ramp up interval and ramp down interval. The test profile preset for ramp up interval was 0.01–500 s^{-1} with 24 measuring points and a 10-second constant measuring point duration. The ramp down interval was 500–0.01 s^{-1} with the same number of measuring points and measuring point duration as in the ramp up interval. An oscillatory test was also performed to characterize the viscoelastic behavior of the samples. The strain amplitude was controlled, and the frequency was kept constant at 10 rad/s in this test. With the help of measured shear stress at different shear rates, *R*-index of different mixture ratios was calculated. *R*-index is a measure that cement engineers use to evaluate the compatibility of different fluids inside the wellbore (Elochukwu et al. 2022). *R*-index can be calculated at different revolution per minute (RPM) values as follows:

$$R\left(\mathrm{RPM}\right) = \theta_m - \theta_p, \tag{1}$$

where θ_m is the highest dial reading among different mixture ratios at a given RPM and θ_p is the highest dial reading among pure fluids at that RPM. Next, the rheological compatibility of the fluid at that RPM is evaluated based on the guideline shown in **Table 4.** The *R*-index values are based on the R1-B1 rotational viscometer readings, and thus the conversion factor of Pa = dial reading×0.511 (*API RP 10B-2* 2013) was used to modify it according to rheometer readings. The average of ramp up and ramp down shear stress values was used to calculate the *R*-index. The reason behind checking the friction pressure for certain *R*-index is to make sure that the mixed fluid in small annuli is not posing a risk to weak formation by increasing bottomhole pressure. Much attention should be paid to the *R*-index at shear rates of 100–200 s^{-1} because these shear rates commonly occur during primary cementing operations.

R-Index (for Rheometer)	Comment
$R < 0$ ($R < 0$)	Compatible
$0 < R < 40$ ($0 < R < 20.44$)	Compatible (check friction pressure)
$41 < R < 70$ ($20.44 < R < 35.77$)	Slightly incompatible (test for better formulation)
$R > 71$ ($R > 35.77$)	Incompatible

Table 4—Guideline to evaluate the compatibility of fluids with respect to *R*-index.

Emulsion Stability Test. The Fann electrical stability tester was used to evaluate the ability of surfactant in the spacer to invert the water/oil (W/O) emulsion, which is done by measuring the stability of OBDF drilling fluid while adding a spacer to it. An electrical stability tester records the maximum voltage that causes internal water droplets coalescence, thus making fluid conductive.

Displacement of OBDF by Spacer. To mimic the fluid displacement in the annulus, a setup was designed that consists of a tube with length, inner diameter, and outer diameter of 278 mm, 15 mm, and 23.7 mm, respectively **(Fig. 1)**. Using a progressive cavity pump, fluids were pumped from the storage tanks to the annular tube with a constant rate of 2.33×10^{-6} m^3/s. First, the test section was filled with OBDF after ensuring that there were no air bubbles in the system and then the fluid was isolated. Afterward, the spacer was pumped through a silicone rubber hose connected to the tube's inlet. The beginning of the test was linked to when we opened the inlet valve, starting the displacement of OBDF by the spacer. The tube also had an outlet valve on top that allowed us to collect the outlet fluid at different times (using a stopwatch). The density of the collected fluid was measured with an Anton Paar DSA 5000 M densitometer, which helped us to evaluate mud displacement. An entrance effect is anticipated in the test section, resembling real-field scenarios where the velocity profile is nonconstant.

Compressive Strength. Spacer samples were cured in cylindrical molds for 1 day and 7 days at a bottomhole static temperature of 70°C and a pressure of 13.8 MPa. Afterward, compressive strength was measured using a standard hydraulic testing machine with a loading rate of 30 kN/min.

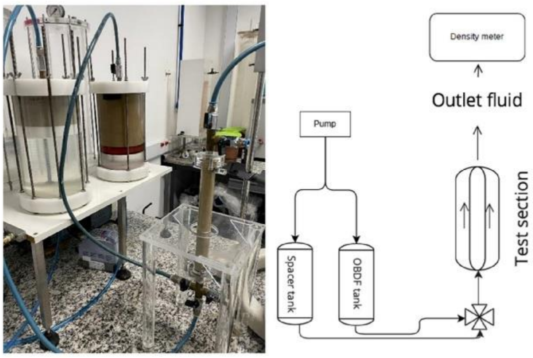

Fig. 1—(Left) displacement test setup. (Right) Schematic of the test setup.

Pumpability. The pumpability of the spacer slurry is evaluated by using OFITE atmospheric consistometer at a bottomhole circulating temperature of 50°C.

Results and Discussions

Compressive Strength. **Fig. 2** shows the compressive strength of the spacer cured for 1 day and 7 days. The spacer can develop over 10 MPa strength after 7 days while having a lower slurry density than conventional cement. Although developing mechanical strength is not among the main functions of the spacer, gradual hardening of the slurry can be of use to wellbore integrity if left in the wellbore.

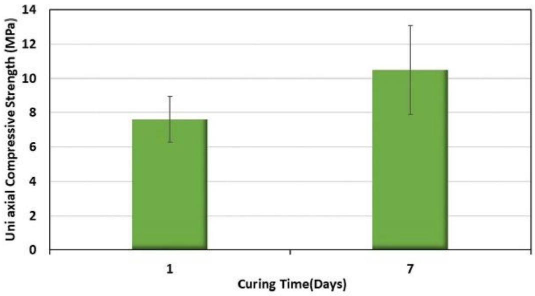

Fig. 2—Compressive strength of cured spacer after 1 day and 7 days, cured at 70°C bottomhole static temperature and 13.8 MPa pressure.

Pumpability. The investigated spacer has the ability of hardening; thus, it is important to evaluate the pumpability of the slurry. The consistency of the spacer slurry over time is shown in **Fig. 3.** It can be concluded that the slurry is pumpable for at least 8 hours at temperatures up to 50°C and it maintains stable consistency during the period of measurement, meaning that the spacer is safe for primary cementing operation. Slag as a binder improves solidified spacer's compressive strength, but its impact on fluid viscosity can be minimal depending on particle-size distribution (Kashani et al. 2013).

Flow Curve. Flow curves of OBDF, spacer, and spacer containing surfactant are plotted in **Fig. 4**, showing that all fluids present a yield stress and shear thinning behavior. The spacer fluids also show thixotropic effects. The ramp up and ramp down shear stress measurements are almost equal for OBDF. By looking at the linear scale flow curve, it can be noticed that OBDF has a higher degree of shear-thinning compared with the spacer. A viscosity profile closer to Newtonian is advantageous for the spacer and may result in better

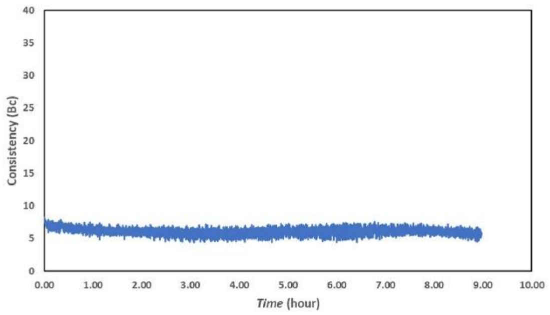

Fig. 3—Pumpability of hardening spacer measured at bottomhole circulating temperature of 50°C and atmospheric pressure.

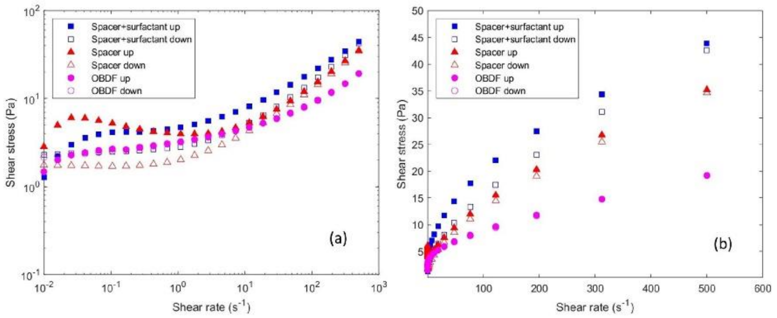

Fig. 4—Flow curve of OBDF, spacer, and spacer with surfactant at ramp up (up) and ramp down (down) measurements. (a) Logarithmic scale. (b) Linear scale.

mud displacement (Nguyen et al. 1992). Moreover, the spacer has generally a higher viscosity than OBDF and passes criteria of at least 10% higher viscosity at 100–200 s^{-1} shear rates that may help with fluid displacement.

From **Fig. 4**, it is obvious that there is a higher difference between ramp up and ramp down stress measurements in spacer fluid compared with OBDF, which indicates that OBDF preserves its structure when experiencing shear, despite showing time-dependent behavior as it is exposed to constant shear rate **(Fig. 5)**. At 0.01 s^{-1} shear rate, it takes approximately 100 seconds for the OBDF to break the structure and reach stress peak; after that, shear stress starts to decrease with a constant slope, meaning the fluid goes through changes. OBDF contains barite as a weighting agent, and these heavy particles gradually settle down and oil moves upward. Thus, it causes lower torque to be recorded after some time. As OBDF is exposed to higher shear rates, the time to reach the stress peak gets faster and the slope of decrease of shear stress over time becomes smaller as the particles experience higher drag force because of the higher flow velocity of the fluid. This means that dynamic sag tendency may become lower as higher shear rates are applied to the sample.

Adding surfactant to the spacer causes a decrease in interfacial tension between water and air. Thus, at enough surfactant concentration, micelles are formed, and consequently small air bubbles start to emerge in the fluid, forming a low-quality foam as shown in **Fig. 6a.** This resulted in an increased viscosity due to a rise in volume fraction of suspension (Stevenson 2012) and a higher difference between the upward and downward shear stress measurements. The explanation for the second observation might be the fact that air bubbles are being deformed or broken up completely during shearing (Herzhaft 2002), and consequently the stress measured during downward shearing is lower and the structure is more destroyed compared with a spacer without surfactants. It is believed that, due to the nonionic nature of surfactant used in the spacer, electrostatic forces between particles should not be affected. However, the van der Waals forces can be changed because of hydrogen forces between molecules on the surface of particles and the polar head of surfactants.

Strain Amplitude Sweep Test. It is not unreasonable to say that all fluids that are typically being used in the wellbore (e.g., cement, drilling fluid, and spacer) are viscoelastic because they consist of particles, clays, polymers, and deformable particles such as droplets.

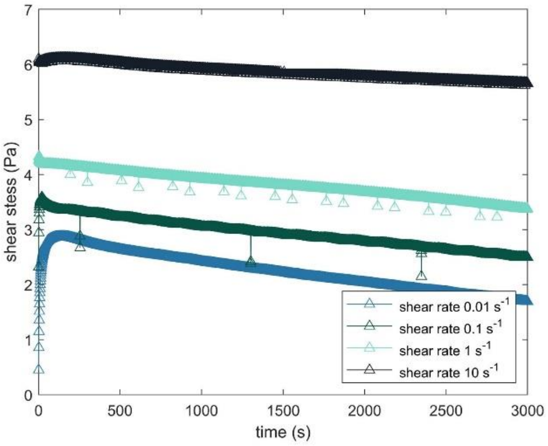

Fig. 5—Constant shear rate tests for OBDF.

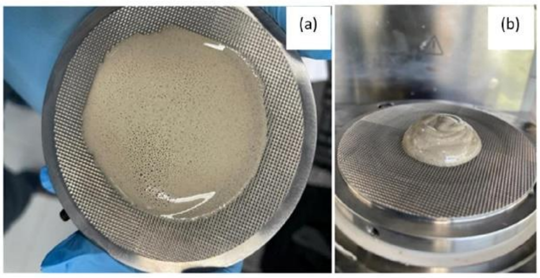

Fig. 6—(a) Air bubbles formed in the spacer after adding nonionic surfactant. (b) Strong gel was observed for 75% spacer containing surfactant and 25% OBDF mixture.

Therefore, measuring the viscosity of the fluid is not enough to understand the behavior of the fluid, especially when at rest or close to yield stress. **Fig. 7b** shows the storage and loss modulus of OBDF and spacer fluids. In this test, shear strain amplitude was varied sinusoidally from 0.01% to 100% and the resulting shear stress was recorded. The G' (storage modulus) is attributed to the elastic behavior of material upon deformation, while the amount of deformation energy dissipated due to internal friction between particles and molecules is represented as the G'' (loss modulus). From **Fig. 7b**, OBDF has a higher G' compared with spacer without the surfactant. The higher elasticity of OBDF is due to the structure of W/O emulsion and the forces that arise from interfacial tension, which tend to bring water droplets to equilibrium in a continuous phase (Oldroyd and Wilson 1953) and steric interaction between chains of absorbed surfactants (Tadros 1994). Brownian motion is also another reason to position the water droplets in place, thus leading to higher gel strength (Saasen 2002). The above-listed phenomenon is more pronounced when the volume fraction of water increases and the distance between droplets decreases in the emulsion. Introducing the surfactant to the spacer and resulting air bubbles in the continuous water phase generates a higher G' modulus. Thus, it is expected that forces more or less the same as those in W/O emulsion will contribute to increase in the elasticity of the spacer. The fluids exhibit a gel-like character in the linear viscoelastic (LVE) range, as the storage modulus is higher than the loss modulus. As long as the materials are inside the LVE range, they preserve their internal structure, and when they exit the LVE range, the particles or droplets (in the case of emulsion) gradually start to leapfrog, and the structure goes through irreversible changes. Finally, at the intersection of G' and G'', the material shows liquid behavior since the structure is completely broken. The stress at this strain is called flow point and it is reported in **Table 5.** The addition of surfactant to the spacer causes an increase in

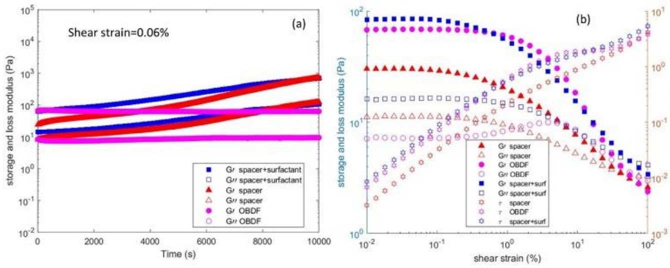

Fig. 7—(a) Time sweep test with constant shear strain selected in LVE range. (b) Shear strain amplitude sweep test.

flow point. The OBDF, unlike the other fluids, shows a G'' peak after the LVE range followed by reduction, which is a typical behavior of highly concentrated suspensions that exhibit a network of forces. When passing yield stress, few water droplets in the OBDF crystalline structure are bypassing each other, and thus a local network of forces is broken and they can move freely in those areas, leading to an increase in internal viscous friction (increase in G''). Meanwhile, the OBDF can maintain the integration of the overall network, meaning that G' is higher than G'' until reaching flow point.

Fluid	OBDF	Spacer	Spacer + Surfactant
LVE range (Pa)	0.409	0.075	0.202
Flow point ($G' = G''$, Pa)	2.3402	1.6739	3.5196

Table 5—Static yield stress of fluids measured by the oscillatory method.

Time Sweep Test. Monitoring G' and G'' over time with constant frequency (10 rad/s) and constant strain (0.06%) selected at the LVE range allows us to investigate the stability of the fluid. **Fig. 7a** shows that the G' and G'' of the spacer are more likely to change over an extended period of time because of solvent evaporation. Thus, it is suggested to use a solvent trap for tests with longer times. In the case of OBDF, G'' drops while G' increases simultaneously at the beginning, which can be attributed to barite settling. The changes are not as severe as those for the spacer.

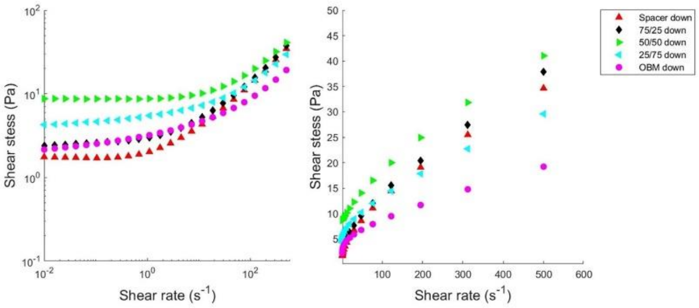

Fig. 8—Flow curve of different ratios of OBDF and spacer mixture at ramp up (up) and ramp down (down) measurements. (a) Logarithmic scale. (b) Linear scale.

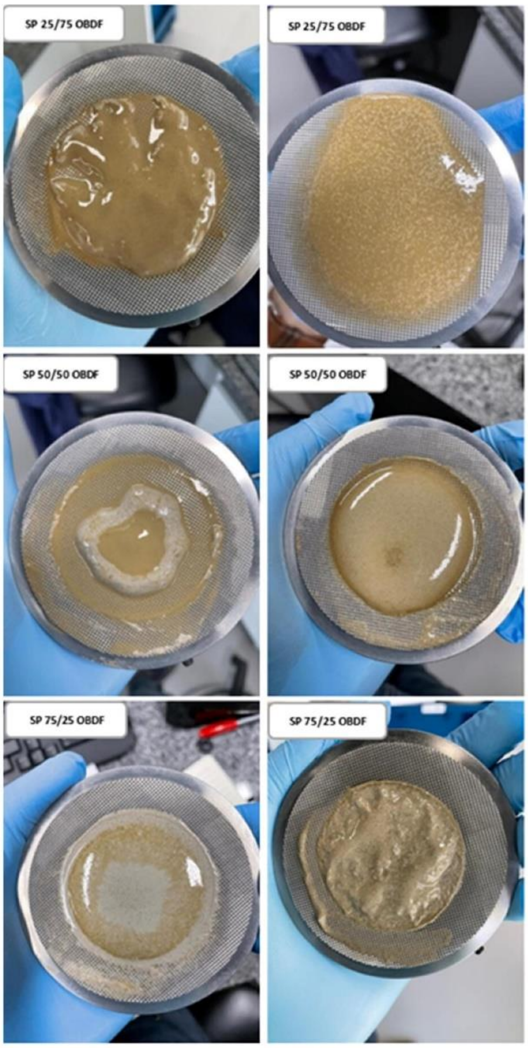

Fig. 9—Macroscopic observations of fluids. (Left) Different ratios of surfactant-free spacer and OBDF mixture. (Right) Different ratios of spacer containing surfactant and OBDF mixture.

Mixtures of Spacer and OBDF. Spacer and drilling fluids are usually in direct contact inside the annulus during mud displacement. Thus, it is of immense importance to evaluate the rheological behavior of the mixture of fluids. **Fig. 8** shows the ramp down flow curve of different ratios by volume of OBDF and spacer (without surfactant) mixed. For instance, 75/25 stands for 75% spacer and 25% OBDF in the mixture and 25/75 stands for 75% OBDF and 25% spacer in the mixture. The fluid that has a lower volume was added to the fluid with a higher volume. In the 75/25 mixture, there are two separate phases due to high interfacial tension between these two fluids, as shown in **Fig. 9.** These resulted in a modest increase in the viscosity profile **(Fig. 8)** and flow point **(Table 6)** of the mixture compared with the neat spacer. When adding spacer to OBDF with the same ratio (25/75), however, there is a shift in viscosity profile compared with neat OBDF. OBDF is W/O emulsion that contains surfactant with a hydrophilic-lipophilic balance value lower than 7 to reduce (Ding et al. 2019) interfacial tension between oil and water and thus keep the water as discrete phase. As the spacer is mixed with OBDF, the emulsion tries to attract the water from the spacer due to an osmotic pressure gradient (Li et al. 2015). Consequently, there will be separate phases of OBDF and spacer that are now thicker than before due to the loss of water, as shown in **Fig. 9**. Increase in the storage modulus **(Fig. 10a)** and the flow point shear stress of this mixture confirms the statements mentioned above. This is even more noticeable in the 50% spacer and 50% OBDF mixture, and the resulting G' and G'' and flow point is the highest.

Shear Stress	OBDF	5/95	25/75	50/50	75/25	95/5	Spacer
LVE range end (Pa)	0.409	0.563	0.369	0.576	0.246	0.068	0.075
Flow point ($G' = G''$, Pa)	2.340	2.870	4.121	6.391	3.850	1.622	1.674

Table 6—Viscoelastic properties of OBDF and surfactant-free spacer mixture measured by amplitude sweep test.

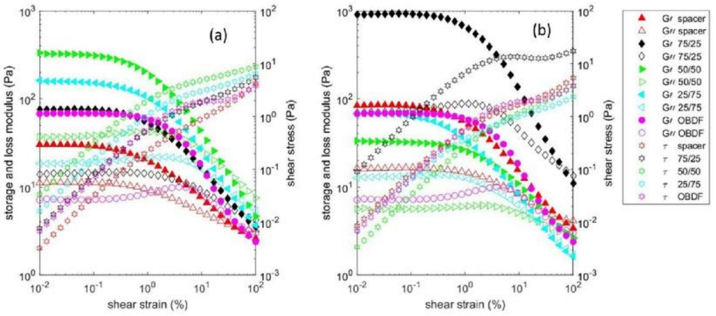

Fig. 10—Shear strain amplitude sweep test. (a) Mixture of spacer and OBDF. (b) Mixture of spacer containing surfactant and OBDF.

Surfactant is an essential component of the spacer that solubilizes the oil and water-wets the surface of the casing and formation. Depending on the type of surfactant, different rheological behavior of the mixture fluid is expected. **Fig. 11** shows the ramp down flow curve of different mixture ratios by volume of OBDF and spacer that contains a nonionic surfactant. When 25% spacer is added to 75% OBDF, there is a reduction in the measured shear stress **(Fig. 11)** and flow point **(Table 7)**. At this mixture ratio, there is enough concentration of nonionic surfactant to diffuse into the oil layer and absorb on the W/O interface and reduce the interfacial viscoelasticity, thus increasing the chance of coalescence of internal water droplets. The water content of the W/O emulsion is also increased and creates higher internal pressure of water droplets (Al-Sabagh et al. 2013). The combination of these two phenomena in turn results in accelerated demulsification and reduced LVE range of the mixture **(Fig. 10b)**. At the 50/50 mixture, the flow curve shifts over and above the OBDF flow curve, and highly uniform fluid was observed **(Fig. 9)**, meaning that critical concentration of nonionic surfactant to reverse the emulsion and turn it into oil/water or water/oil/water is passed. When we added 25% OBDF to 75% spacer by volume, a significant increase in flow point and viscoelasticity was observed **(Fig. 10b)**. This can be confirmed by an increase in the shear stress in lower shear rates measured with the rotational method. When surfactant is included in the design, 50/50 drilling fluid and spacer mixture had lower flow curve shear stresses compared to the pure spacer. This means that a dispersed oil-in-water emulsion is formed that has fewer solid particles compared with a pure spacer. On the other hand, when there is no surfactant in the spacer, the 50/50 mixture had a higher flow curve compared with pure spacer while containing fewer solid particles. Because there is no surfactant in the spacer to lower the interfacial tension, an immiscible mixture is formed. Also, OBDF tries to attract water from the spacer into the internal phase (Li et al. 2015), leaving a thick layer of the solid phase of spacer on the bottom.

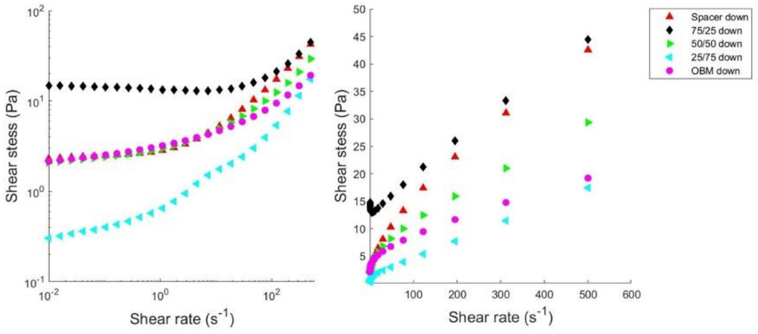

Fig. 11—Flow curve of different ratios of OBDF and spacer with surfactant mixture. (a) Logarithmic scale. (b) Linear scale.

Shear Stress	OBDF	5/95	25/75	50/50	75/25	95/5	Spacer
LVE range end (Pa)	0.409	0.358	0.091	0.184	3.002	2.560	0.201
Flow point ($G' = G''$, Pa)	2.340	2.008	1.325	3.108	15.756	17.202	3.520

Table 7—Viscoelastic properties of OBDF and spacer containing surfactant mixture measured by amplitude sweep test.

Comparing the highest shear stress flow curve of the spacer without surfactant/OBDF **(Fig. 8)**, which was for 50/50, and the spacer with surfactant/OBDF mixtures **(Fig. 11)**, which happened for 75/25, it can be concluded that surfactant in the design mostly impacted the shear stress measured at low shear rates and fewer changes on the stress at higher shear rates were noticed.

Viscosity Models. Calculating rheological parameters gives us insight into the flow behavior of the fluids. Additionally, it can help fluid displacement simulations to produce trusted and worthier results. A common model is the Herschel-Bulkley (H-B), which has three parameters to fairly estimate the viscosity of shear-dependent yield stress fluids. It can be expressed as follows:

$$\tau = \tau_y + k\dot{\gamma}^n \ , \ \tau > \tau_y, \tag{2}$$

where k is the consistency index, and n is the H-B flow behavior index. $n < 1$, $n > 1$, and $n = 1$ indicate shear-thinning, shear-thickening, and Bingham behavior, respectively. The yield stress can be obtained using these models to fit the rheological data in the flow curve. The mathematical variable known as the consistency index is solely dependent on the value of n and cannot be used to make comparisons between different fluids, which is a crucial function that viscosity models should perform. The application of curve fitting to diverse shear rate ranges produces entirely distinct values of k. Nelson and Ewoldt (2017) made alterations to the H-B model with the aim of removing its dependence on the value of k:

$$\tau = \tau_y \left[1 + \left(\frac{\dot{\gamma}}{\dot{\gamma}_c}\right)^n\right]. \tag{3}$$

Saasen and Ytrehus (2020) made some modifications to the model to overcome its limitations and make it more suitable for a fluid with lower shear rates. They named this modified model the dimensionless shear rate model, and it was intended for application in a different industry:

$$\tau = \tau_y + \tau_s \left(\frac{\dot{\gamma}}{\dot{\gamma}_c}\right)^n. \tag{4}$$

The surplus stress (τ_s) can be obtained by subtracting the yield stress from the shear stress, which is determined at a relevant shear rate based on the condition of flow. Yield stress is obtained from the H-B model. The relevant shear rate ($\dot{\gamma}_c$) is determined based on the flow condition and geometry, and during cement placement, a common shear rate is 195 s^{-1} (Kamali et al. 2021), which is close to 100 rev/min using a conversion factor of $\text{s}^{-1} = \text{RPM} \times 1.703$. To improve the accuracy of fitting, two different characteristic shear rates, one at higher shear rates (312 s^{-1}) and one at lower shear rates (122 s^{-1}) than the surplus shear rate, are chosen to calculate the flow behavior index:

$$n_{ls} = \frac{\ln\left(\frac{\tau_{122} - \tau_y}{\tau_s}\right)}{\ln\left(\frac{\dot{\gamma}_{122}}{\dot{\gamma}_c}\right)}, \tag{5}$$

$$n_{hs} = \frac{\ln\left(\frac{\tau_{312} - \tau_y}{\tau_s}\right)}{\ln\left(\frac{\dot{\gamma}_{312}}{\dot{\gamma}_c}\right)}. \tag{6}$$

Ramp down shear stress measurements from 500 to 1 s^{-1} were used to perform curve fitting because ramp up measurements could be affected by viscoelasticity or thixotropy in lower shear rates. **Table 8** shows the rheological parameters after curve fitting of the flow curve of different mixture ratios of OBDF and spacer. The highest yield stress belongs to the 50% spacer and 50% OBDF mixture. The flow behavior index calculated by the dimensionless shear rate model also slightly increases as one moves toward the 50/50 mixture ratio. The impact of including the surfactant in the spacer design on the rheological parameters of the mixture is shown in **Table 9** for different mixture ratios. The 25/75 mixture has the lowest yield stress while having high n_{ls} and n_{hs}, as demulsification in this ratio is expected. A yield stress peak is observed for the 95/5 and 75/25, and we try to explain the reasoning for this in the next sections.

Model	Parameter	Unit	OBDF	5/95	25/75	50/50	75/25	95/5	Spacer
H-B	τ_y	Pa	3.112	3.733	5.321	8.125	2.698	1.532	1.545
	k	Pa·s^n	0.304	0.394	0.342	0.361	0.436	0.648	0.535
	n	–	0.637	0.626	0.685	0.727	0.705	0.670	0.663
	R^2	–	0.9991	0.9989	0.9997	0.9998	0.9997	0.9999	0.9999
	SSE	Pa^2	0.2684	0.4721	0.1764	0.2219	0.4089	0.179	0.1172
Dimensionless shear rate model	τ_y	Pa	3.112	3.733	5.321	8.125	2.698	1.532	1.545
	τ_s	Pa	8.556	10.4	12.515	16.808	17.705	21.977	17.53
	n_{ls}	–	0.630	0.612	0.680	0.740	0.683	0.659	0.655
	n_{hs}	–	0.659	0.653	0.702	0.733	0.709	0.672	0.663

Table 8—Rheological parameters calculated for mixtures of OBDF and surfactant-free spacer.

Model	Parameter	Unit	OBDF	5/95	25/75	50/50	75/25	95/5	Spacer
H-B	τ_y	Pa	3.112	1.86	0.963	2.975	12.68	11.1	2.286
	k	Pa·s^n	0.304	0.373	0.057	0.321	0.088	0.164	0.547
	n	–	0.637	0.612	0.910	0.706	0.947	0.873	0.691
	R^2	–	0.9991	0.9992	0.9982	0.9985	0.9991	0.9991	0.9999
	SSE	Pa^2	0.2684	0.2489	0.5679	1.217	1.023	1.479	0.1243
Dimensionless shear rate model	τ_y	Pa	3.112	1.86	0.963	2.975	12.68	11.1	2.286
	τ_s	Pa	8.556	9.065	6.749	12.936	13.322	16.64	20.788
	n_{ls}	–	0.630	0.619	0.896	0.659	0.948	0.862	0.677
	n_{hs}	–	0.659	0.657	0.942	0.706	0.927	0.846	0.692

Table 9—Rheological parameters calculated for mixtures of OBDF and spacer containing surfactant.

***R*-Index.** The compatibility of the two fluids is established when the rheological behavior of the mixture remains relatively unchanged compared with the rheology of the individual fluids, namely, the OBDF and spacer slurry. Any substantial increase in the flow curve values indicates gelation of the mixture, which is considered undesirable and indicative of incompatibility. In the best-case scenario, two fluids can be considered rheologically compatible when any mixtures of the fluids have flow curves laying between the flow curves of the pure fluids. When there is a notable increase in the flow curve of the mixture, it indicates that there will be an undesired rise in the bottomhole pressure required for the spacer to displace the mixing zone. This increased pressure can potentially result in the fracturing of the formation. The increase in the flow curve values of the mixture can also affect mud displacement. According to the effective laminar flow rule system proposed by Couturler et al. (1990), the frictional pressure gradient exerted by the displacing fluid (spacer) should be at least 20% higher than that of the displaced fluid (mixture) for efficient displacement. This implies that displacement in the wellbore becomes harder if the less viscous displacing fluid (spacer) is displacing a mixture with higher viscosity. Thus, cement engineers developed a system to evaluate the compatibility of the fluids in the wellbore. **Table 10** shows the *R*-index of OBDF and spacer without surfactant that was calculated for different shear rates. Based on the *R*-index guideline shown earlier in **Table 4**, the fluids are compatible. However, the friction pressure should be checked based on operational parameters and wellbore geometry. Adding surfactant to hardening spacer decreases the *R*-index at higher shear rates while increasing the *R*-index at lower shear rates compared with surfactant-free spacer

Shear Rate (s^{-1})	Shear Stress (Pa)							
	OBM	5/95	25/75	50/50	75/25	95/5	Spacer	*R*-Index
500	10.32	23.28	29.94	39.59	38.03	43.66	34.92	8.74
312	8.39	18.11	23.78	30.50	28.25	32.42	26.11	6.31
195	7.04	14.50	19.38	24.69	21.69	24.39	19.68	5.01
122	7.12	11.93	16.38	20.60	16.93	18.48	14.97	5.63
47.60	4.76	8.57	11.46	14.78	10.74	10.83	8.99	5.79
11.60	3.82	5.91	7.51	10.40	6.21	5.32	4.82	5.58
4.53	3.59	4.91	6.71	8.730	4.86	3.61	3.61	5.12

Table 10—*R*-index calculated for surfactant-free spacer, OBDF, and mixture of them for different shear rates.

(Table 11). This rises from the formation of strong gel for 75/25 and 95/5 mixture ratios. *R*-index at a relevant shear rate (195 s^{-1}) is 5.01 and 6.32 for the spacer/OBDF and spacer (surfactant)/OBDF mixture, respectively.

Shear Rate (s^{-1})	Shear Stress (Pa)							
	OBM	5/95	25/75	50/50	75/25	95/5	Spacer	*R*-Index
500	10.32	19	17.41	30.67	45.39	49.28	43.23	6.04
312	8.39	14.15	11.36	23.57	35.68	38.65	32.70	5.95
195	7.04	10.99	7.96	18.61	29.32	31.57	25.26	6.32
122	7.12	8.75	5.75	15.00	24.98	26.73	19.74	6.99
47.60	4.76	5.93	3.46	10.25	19.89	21.06	12.34	8.72
11.60	3.82	3.84	2.14	6.20	16.84	18.09	6.730	11.36
4.53	3.59	3.10	1.55	4.82	16.58	18.10	4.990	13.11

Table 11—*R*-index calculated for spacer with surfactant, OBDF, and mixture of them for different shear rates.

Emulsion Stability Test. The electrical stability of OBDF is shown in **Fig. 12.** It is clear that as the volume of titrated spacer increases, the stability of the emulsion is undermined. This means that the spacer increases the water content, and in turn, bigger and additional water droplets are formed in the emulsion resulting in lower voltage for internal phase coalescence and current initiation. When the spacer that contains surfactant is added to OBDF, at a lower concentration, the recorded voltage converges to zero. In other words, the surfactant in the spacer could break the OBDF emulsion by absorbing into water droplet interface and forming two continuous phases. The decrease in

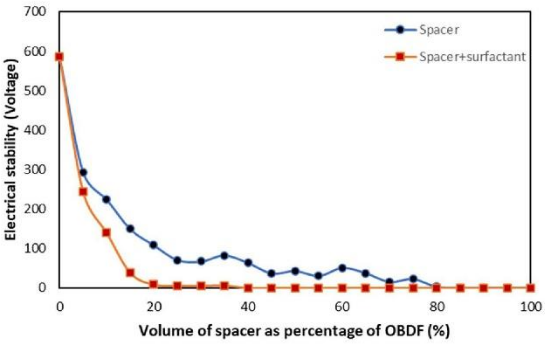

Fig. 12—Impact of spacer on the stability of OBDF.

flow curve of the 25/75 mixture relative to OBDF confirms this **(Fig. 11b)**. This is necessary to obtain a better bonding during cementing and while curing the spacer.

Surfactant Mechanisms in Hardening Spacer. Incorporating nonionic surfactant in the hardening spacer causes an increase in yield stress. The surfactant can act in two ways: First, its polar head can be absorbed into the hydrophilic surface of slag particles, leaving lipophilic tails to attract each other and increase the yield stress (Feneuil et al. 2017). Second, at enough surfactant concentration, air bubbles are formed as a result of mechanical stirring and can be stabilized by the surfactant. These air bubbles increase the volume fraction of the suspension resulting in higher viscosities (Barnes et al. 1989). There is a resemblance between oil droplets and air bubbles present in the spacer that contains surfactant. The addition of OBDF to the hardening spacer (with surfactant) results in a substantial increase in the yield stress and storage modulus. It is believed that oil is positioned between the slag particles with the help of surfactants **(Fig. 13)**. The hydrophobic tails interact with the mineral oil, while the polar head is absorbed by the hydrophilic slag particles. Consequently, a very stable physical-chemical network of structure in suspension is formed, which is shear-dependent (Reeb et al. 2022).

Displacement of OBDF by Spacer. Two scenarios of immiscible displacement of OBDF by (a) spacer and (b) spacer containing surfactant were tested. This experiment aimed to evaluate the impact of surfactant on the OBDF displacement. **Fig. 14** shows the outlet fluid density

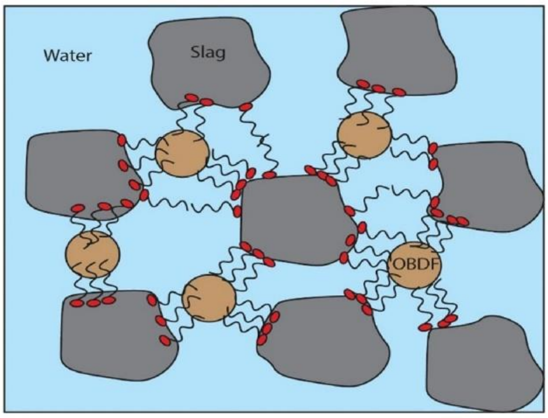

Fig. 13—Schematic of possible mechanism for pronounced viscoelasticity observed for 95/5 and 75/25 spacer/OBDF mixture.

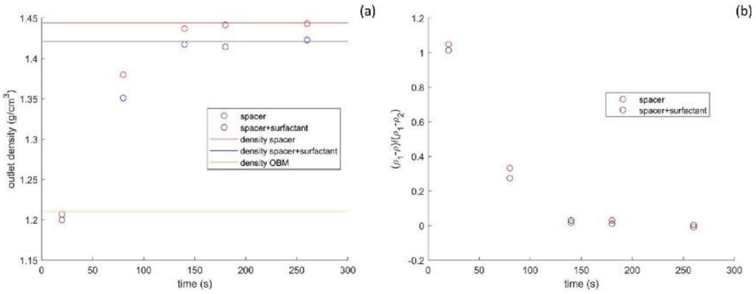

Fig. 14—OBDF displacement test. Solid lines represent the density of pure fluids. (a) Density of outlet fluid is measured as a function of time. (b) Normalized density as a function of time.

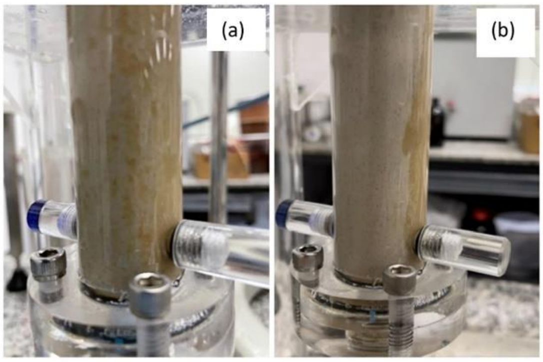

Fig. 15—Picture of the annular test section after displacement. OBDF and spacer have brown and gray colors, respectively. (a) Displacement of OBDF by surfactant-free spacer. (b) Displacement of OBDF by spacer containing surfactant.

collected at different times for the above-mentioned scenarios. For better understating, the normalized outlet density, $(\rho_1 - \rho)/(\rho_1 - \rho_2)$ is also shown in **Fig. 14**, where ρ_1 and ρ_2 are the density of spacer and OBDF, respectively, and ρ is the measured density of outlet fluid. At the beginning of displacement, the normalized outlet density is equal to unity because only OBDF leaves the annulus. As the displacement continues, the density of the outlet fluid increases as a mixture of spacer (higher density) and OBDF leaves the test section, and thus the normalized outlet density lies between 0 and 1. At a long enough time, the only fluid that leaves the annulus is the spacer so that the measured outlet density converges to the spacer density and the normalized outlet density to zero. This is an indication that the spacer has displaced the maximum possible amount of OBDF from test section. In **Fig. 15**, it is evident that, even after displacement, some OBDF is left in the annulus. The volume of OBDF (Fluid 2) that is removed from the annulus by the flow of the displacing fluid (spacer) is equal to the volume of the spacer that fills the annulus when the final steady-state condition is reached, and no further displacement occurs. Thus, the normalized outlet density cannot be used to quantitatively evaluate the volume of removed OBDF. To compare the extent of mud bypassed by the spacer in two cases with an equal pumping rate, one can examine the time it takes for the normalized outlet density to converge to zero. The results show that the surfactant in the spacer design has minimal impact on the OBDF displacement efficiency although resulting in a different flow behavior of the mixture. Surfactant, however, played a key role in cleaning the annulus walls that were covered with OBDF, as shown in **Fig. 15**. According to Foroushan et al. (2018), reducing the interfacial tension can lower the radial interface instability, and, consequently, a thinner layer of mud is left on the walls.

Conclusion

The rheological compatibility of the hardening spacer and OBDF was discussed here. Surfactant in spacer design is a crucial factor that controls the flow behavior of the spacer/OBDF mixture. A nonionic surfactant resulted in unexpected viscoelasticity for 95/5 and 75/25 mixture of spacer/OBDF. Based on R-index values, however, the hardening spacer and OBDF are rheologically compatible. The hardening spacer with surfactant can break the OBDF emulsion at a 25/75 mixture ratio and reverse the emulsion at a 50/50 mixture ratio. The displacement of OBDF by spacer on a small scale was also tested. The result shows that, although different rheological properties of the mixture were measured, depending on whether there is surfactant in design, there is no significant difference in the displacement of OBDF by the spacer. Nevertheless, the surfactant seems to be more beneficial to cleaning the static mud layer on the walls.

Nomenclature

G' = storage modulus, Pa
G'' = loss modulus, Pa
k = consistency index, Pa·s^n
n = flow behavior index, dimensionless
n_{ls} = flow behavior index at shear rates below the surplus shear rate, dimensionless
n_{hs} = flow behavior index at shear rates above the surplus shear rate, dimensionless
R^2 = coefficient of determination
SSE = sum of square of errors, Pa^2
θ_p = highest dial reading among pure fluids
θ_m = highest dial reading among different mixtures
$\dot{\gamma}$ = shear rate, s^{-1}
$\dot{\gamma}_c$ = relevant shear rate, s^{-1}
τ = shear stress, Pa
τ_y = yield stress, Pa
τ_s = surplus stress, Pa
μ_p = Bingham plastic viscosity, Pa·s

ρ = measured density of outlet fluid, g/cm^3
ρ_1 = density of spacer slurry, g/cm^3
ρ_2 = density of OBDF, g/cm^3

Acknowledgments

The authors want to thank the rheology group of PUC-Rio for giving us the opportunity to use their laboratory equipment. The authors gratefully acknowledge TotalEnergies, Aker BP, ConocoPhillips, and Research Council of Norway for financially supporting the SafeRock KPN Project (RCN #319014319014—New Cementitious Material for Oil Well Cementing Applications—SafeRock) at the University of Stavanger, Norway.

References

Allouche, M., Frigaard, I. A., and Sona, G. 2000. Static Wall Layers in the Displacement of Two Visco-Plastic Fluids in a Plane Channel. *J Fluid Mech* **424**: 243–277. https://doi.org/10.1017/S0022112000001956.

Al-Sabagh, A. M., Kandile, N. G., El-Ghazawy, R. A. et al. 2013. Synthesis and Evaluation of New Demulsifiers Incorporating Linear Alkyl Benzene Moiety for Treating Water-in-Oil Emulsion. *J Dispers Sci Technol* **34** (7): 996–1007. https://doi.org/10.1080/01932691.2012.695941.

API RP 10B-2, *Recommended Practice for Testing Well Cements*. 2013. Washington, DC, USA: American Petroleum Institute (API).

Barnes, H. A., Hutton, J. F., and Walters, K. 1989. *An Introduction to Rheology*, First edition. Netherlands: Elsevier.

Brice, J. W. and Holmes, B. C. 1964. Engineered Casing Cementing Programs Using Turbulent Flow Techniques. *J Pet Technol* **16** (5): 503–508. SPE-742-PA. https://doi.org/10.2118/742-PA.

Bu, Y., Li, Z., Wan, C. et al. 2016. Determination of Optimal Density Difference for Improving Cement Displacement Efficiency in Deviated Wells. *J Nat Gas Sci Eng* **31**: 119–128. https://doi.org/10.1016/j.jngse.2016.03.008.

Carney, L. 1974. Cement Spacer Fluid. *J Pet Technol* **26** (8): 856–858. SPE-4784-PA. https://doi.org/10.2118/4784-PA.

Carrasco-Teja, M. and Frigaard, I. A. 2009. Displacement Flows in Horizontal, Narrow, Eccentric Annuli with a Moving Inner Cylinder. *Phys Fluids* **21** (7): 073102. https://doi.org/10.1063/1.3193712.

Carrasco-Teja, M., Frigaard, I. A., Seymour, B. R. et al. 2008. Viscoplastic Fluid Displacements in Horizontal Narrow Eccentric Annuli: Stratification and Travelling Wave Solutions. *J Fluid Mech* **605**: 293–327. https://doi.org/10.1017/S0022112008001535.

Carrasco-Teja, M. and Frigaard, I. A. 2010. Non-Newtonian Fluid Displacements in Horizontal Narrow Eccentric Annuli: Effects of Slow Motion of the Inner Cylinder. *J Fluid Mech* **653**: 137–173. https://doi.org/10.1017/S0022112010000212.

Carter, L. G. and Evans, G. W. 1964. A Study of Cement-Pipe Bonding. *J Pet Technol* **16** (2): 157–160. SPE-764-PA. https://doi.org/10.2118/764-PA.

Couturler, M., Guillot, D., Hendriks, H. et al. 1990. Design Rules And Associated Spacer Properties For Optimal Mud Removal In Eccentric Annuli. Paper presented at the CIM/SPE International Technical Meeting, Calgary, Alberta, Canada, 10–13 June. SPE-21594-MS. https://doi.org/10.2118/21594-MS.

Cowan, K. M., Hale, A. H., and Nahm, J. J. 1992. Conversion of Drilling Fluids to Cements With Blast Furnace Slag: Performance Properties and Applications for Well Cementing. Paper presented at the SPE Annual Technical Conference and Exhibition, Washington, D.C., USA, 4–7 October. SPE-24575-MS. https://doi.org/10.2118/24575-MS.

Curbelo, F. D. S., Garnica, A. I. C., Araújo, E. A. et al. 2018. Vegetable Oil-Based Preflush Fluid in Well Cementing. *J Pet Sci Eng* **170**: 392–399. https://doi.org/10.1016/j.petrol.2018.06.061.

da Silva, D. C., Araújo, C. R. B. de, Oliveira Freitas, J. C. de et al. 2020. Formulation of New Microemulsion Systems Containing Produced Water for Removal of Filter Cake from Olefin-Based Drilling Fluid. *J Pet Sci Eng* **193**: 107425. https://doi.org/10.1016/j.petrol.2020.107425.

Davies, R. J., Almond, S., Ward, R. S. et al. 2014. Oil and Gas Wells and Their Integrity: Implications for Shale and Unconventional Resource Exploitation. *Mar Pet Geol* **56**: 239–254. https://doi.org/10.1016/j.marpetgeo.2014.03.001.

Ding, S., Serra, C. A., Vandamme, T. F. et al. 2019. Double Emulsions Prepared by Two-Step Emulsification: History, State-of-the-Art and Perspective. *J Control Release* **295**: 31–49. https://doi.org/10.1016/j.jconrel.2018.12.037.

Eid, E., Tranggono, H., Khalifeh, M. et al. 2021. Impact of Drilling Fluid Contamination on Performance of Rock-Based Geopolymers. *SPE J.* **26** (6): 3626–3633. SPE-205477-PA. https://doi.org/10.2118/205477-PA.

Elochukwu, H., Samansu Douglas, E., and Chikere, A. O. 2022. Evaluation of Methyl Ester Sulphonate Spacer Fluid Additive for Efficient Wellbore Clean-Up. *Energy Geosci* **3** (1): 73–79. https://doi.org/10.1016/j.engeos.2021.11.002.

Feneuil, B., Pitois, O., and Roussel, N. 2017. Effect of Surfactants on the Yield Stress of Cement Paste. *Cem Concr Res* **100**: 32–39. https://doi.org/10.1016/j.cemconres.2017.04.015.

Foroushan, H. K., Ozbayoglu, E. M., Miska, S. Z. et al. 2018. On the Instability of the Cement/Fluid Interface and Fluid Mixing. *SPE Drill & Compl* **33** (1): 63–76. SPE-180322-PA. https://doi.org/10.2118/180322-PA.

Gomado, F. D., Khalifeh, M., and Aasen, J. A. 2023. Expandable Geopolymers for Improved Zonal Isolation and Plugging. Paper presented at the SPE/IADC International Drilling Conference and Exhibition, Stavanger, Norway, 7–9 March. SPE-212493-MS. https://doi.org/10.2118/212493-MS.

Gordon, C. L., Lewis, S. J., and Tonmukayakul, P. 2008. Rheological Properties of Cement Spacer: Mixture Effects. Paper presented at the AADE Fluids Conference and Exhibition, Texas, USA, 8–9 April. AADE-08-DF-HO-09.

Herzhaft, B. 2002. Correlation between Transient Shear Experiments and Structure Evolution of Aqueous Foams. *J Colloid Interface Sci* **247** (2): 412–423. https://doi.org/10.1006/jcis.2001.8153.

Jakobsen, J., Sterri, N., Saasen, A. et al. 1991. Displacements in Eccentric Annuli During Primary Cementing in Deviated Wells. Paper presented at the SPE Production Operations Symposium, Oklahoma City, Oklahoma, USA, 7–9 April. SPE-21686-MS. https://doi.org/10.2118/21686-MS.

Kamali, M., Khalifeh, M., Saasen, A. et al. 2021. Alternative Setting Materials for Primary Cementing and Zonal Isolation – Laboratory Evaluation of Rheological and Mechanical Properties. *J Pet Sci Eng* **201**: 108455. https://doi.org/10.1016/j.petrol.2021.108455.

Kashani, A., Provis, J. L., and van Deventer, J. S. J. 2013. Effect of Ground Granulated Blast Furnace Slag Particle Size Distribution on Paste Rheology: A Preliminary Model. Paper presented at the Powders and Grains, Vol. 1, 1094–1097, Sydney, Australia, 18 June. https://doi.org/10.1063/1.4812126.

Khalili, P., Khalifeh, M., and Saasen, A. 2022. The Effect of Fluid Contamination on Rheological Properties of Geopolymer Materials. Paper presented at the ASME 2022 41st International Conference on Ocean, Offshore and Arctic Engineering, Hamburg, Germany. https://doi.org/10.1115/OMAE2022-78994.

Li, Z., Liu, H., Guo, X. et al. 2016. Contamination of Cement Slurries with Oil Based Mud and Its Components in Cementing Operations. *J Nat Gas Sci Eng* **29**: 160–168. https://doi.org/10.1016/j.jngse.2016.01.003.

Li, M., Ou, H., Li, Z. et al. 2015. Contamination of Cement Slurries with Diesel-Based Drilling Fluids in a Shale Gas Well. *J Nat Gas Sci Eng* **27**: 1312–1320. https://doi.org/10.1016/j.jngse.2015.08.010.

Liu, X., Nair, S., Aughenbaugh, K. et al. 2019. Mud-to-Cement Conversion of Non-Aqueous Drilling Fluids Using Alkali-Activated Fly Ash. *J Pet Sci Eng* **182**: 106242. https://doi.org/10.1016/j.petrol.2019.106242.

Lockyear, C. F., Ryan, D. F., and Gunningham, M. M. 1990. Cement Channeling: How to Predict and Prevent. *SPE Drill Eng* **5** (3): 201–208. SPE-19865-PA. https://doi.org/10.2118/19865-PA.

Maleki, A. and Frigaard, I. A. 2019. Comparing Laminar and Turbulent Primary Cementing Flows. *J Pet Sci Eng* **177**: 808–821. https://doi.org/10.1016/j.petrol.2019.02.054.

Maserati, G. ., Daturi, E. ., Belloni, A. . et al. 2010. Nano-Emulsions as Cement Spacer Improve the Cleaning of Casing Bore During Cementing Operations. Paper presented at the SPE Annual Technical Conference and Exhibition, Florence, Italy, 19–22 September. SPE-133033-MS. https://doi.org/10.2118/133033-MS.

Nelson, A. Z. and Ewoldt, R. H. 2017. Design of Yield-Stress Fluids: A Rheology-to-Structure Inverse Problem. *Soft Matter* **13** (41): 7578–7594. https://doi.org/10.1039/c7sm00758b.

Nelson, E. B. and Guillot, D. 2006. Chapter 5 - Mud Removal. In *Well Cementing*, 143–191. Houston, Texas, USA: Schlumberger.

Nguyen, D., Kagan, M., and Rahman, S. S. 1992. Evaluation of Drilling Fluid Removal by Cement Slurry from Horizontal Wells with the Use of an Accurate Mathematical Model. *J Pet Sci Eng* **8** (3): 191–204. https://doi.org/10.1016/0920-4105(92)90033-W.

Oldroyd, J. G. and Wilson, A. H. 1953. The Elastic and Viscous Properties of Emulsions and Suspensions. *Proc R Soc Lond A* **218** (1132): 122–132. https://doi.org/10.1098/rspa.1953.0092.

Opedal, N., Todorovic, J., Torsæter, M. et al. 2014. Experimental Study on the Cement-Formation Bonding. Paper presented at the SPE International Symposium and Exhibition on Formation Damage Control, Lafayette, Louisiana, USA, 26–28 February. SPE-168138-MS. https://doi.org/10.2118/168138-MS.

Oyibo, A. and Radonjic, M. 2014. Impact of Physical and Chemical Mud Contamination on Cement-Formation Shear Bond Strength. Paper presented at the ASME 2014 33rd International Conference on Ocean, Offshore and Arctic Engineering, MAE2014–24596, San Francisco, California, USA, 8–13 June. https://doi.org/10.1115/OMAE2014-24596.

Pietrangeli, G., Quintero, L., and Gonzalez, Y. 2015. In-Situ Microemulsions Enhance Removal of Non-Aqueous Drilling Fluid in Gulf of Guinea Wells. Paper presented at the SPE European Formation Damage Conference and Exhibition, Budapest, Hungary, 3–5 June. SPE-174239-MS. https://doi.org/10.2118/174239-MS.

Reeb, C., Davy, C. A., Pierlot, C. et al. 2022. Emulsification of Low Viscosity Oil in Alkali-Activated Materials. *Cem Concr Res* **162**: 106963. https://doi.org/10.1016/j.cemconres.2022.106963.

Saasen, A. 2002. Sag of Weight Materials in Oil Based Drilling Fluids. Paper presented at the IADC/SPE Asia Pacific Drilling Technology, Jakarta, Indonesia, 9–11 September. SPE-77190-MS. https://doi.org/10.2118/77190-MS.

Saasen, A. and Ytrehus, J. D. 2020. Viscosity Models for Drilling Fluids—Herschel-Bulkley Parameters and Their Use. *Energies* **13** (20): 5271. https://doi.org/10.3390/en13205271.

Saasen, A., Salmelid, B., Blomberg, N. et al. 1994. The Use of Blast Furnace Slag in North Sea Cementing Applications. Paper presented at the European Petroleum Conference, London, UK, 25–27 October. SPE-28821-MS. https://doi.org/10.2118/28821-MS.

Santos, L., Alghamdi, A., and Taleghani, A. 2019. Experimental Evaluation of the Impact of Oil-Based Mud Residuals on Cement-Formation Bonding Strength. Paper presented at the AADE National Technical Conference and Exhibition, Denver, Colorado, USA, 9–10 April. AADE-19-NTCE-102.

Sarmadi, P., Renteria, A., and Frigaard, I. A. 2021. Primary Cementing of Horizontal Wells. Displacement Flows in Eccentric Horizontal Annuli. Part 2. Computations. *J Fluid Mech* **915**. https://doi.org/10.1017/jfm.2021.158.

Schlemmer, R. P., Branam, N. E., Edwards, T. M. et al. 1994. Drilling Fluid Conversion: Selection and Use of Portland or Blast-Furnace-Slag Cement. *SPE Drill & Compl* **9** (4): 249–255. SPE-26324-PA. https://doi.org/10.2118/26324-PA.

Soares, A. A., Freitas, J. C. de O., Melo, D. M. de A. et al. 2017. Cement Slurry Contamination with Oil-Based Drilling Fluids. *J Pet Sci Eng* **158**: 433–440. https://doi.org/10.1016/j.petrol.2017.08.064.

Stevenson, P. 2012. *Foam Engineering: Fundamentals and Applications*. Chichester, West Sussex, UK: John Wiley & Sons. https://doi.org/10.1002/9781119954620.

Tadros, Th. F. 1994. Fundamental Principles of Emulsion Rheology and Their Applications. *Colloids Surf A Physicochem Eng Asp* **91**: 39–55. https://doi.org/10.1016/0927-7757(93)02709-N.

Taghavi, S. M., Seon, T., Martinez, D. M. et al. 2009. Buoyancy-Dominated Displacement Flows in near-Horizontal Channels: The Viscous Limit. *J Fluid Mech* **639**: 1–35. https://doi.org/10.1017/S0022112009990620.

Tehrani, Ahmadi., Ferguson, J., and Bittleston, S. H. 1992. Laminar Displacement in Annuli: A Combined Experimental and Theoretical Study. Paper presented at the SPE Annual Technical Conference and Exhibition, Washington, D.C., USA, 4–7 October. SPE-24569-MS. https://doi.org/10.2118/24569-MS.

Wanderley Neto, A. O., da Silva, V. L., Rodrigues, D. V. et al. 2020. A Novel Oil-in-Water Microemulsion as A Cementation Flushing Fluid for Removing Non-Aqueous Filter Cake. *J Pet Sci Eng* **184**: 106536. https://doi.org/10.1016/j.petrol.2019.106536.

Yousefi Oderji, S., Chen, B., and Mohseni, E. 2023. The Efficiency of Borax as an Additive on Properties of One-Part Fly Ash/Slag-Based Alkali-Activated Materials. *Eur J Env Civ Eng*: 1–13. https://doi.org/10.1080/19648189.2023.2182367.

Appendix 6 – Paper V

A case study for tailored formulation of geopolymers aided by annular displacement simulations

Alondra Renteria, Pouya Khalili, Ian Frigaard, Mahmoud Khalifeh

Geoenergy Science and Engineering

DOI: https://doi.org/10.1016/j.geoen.2023.212110

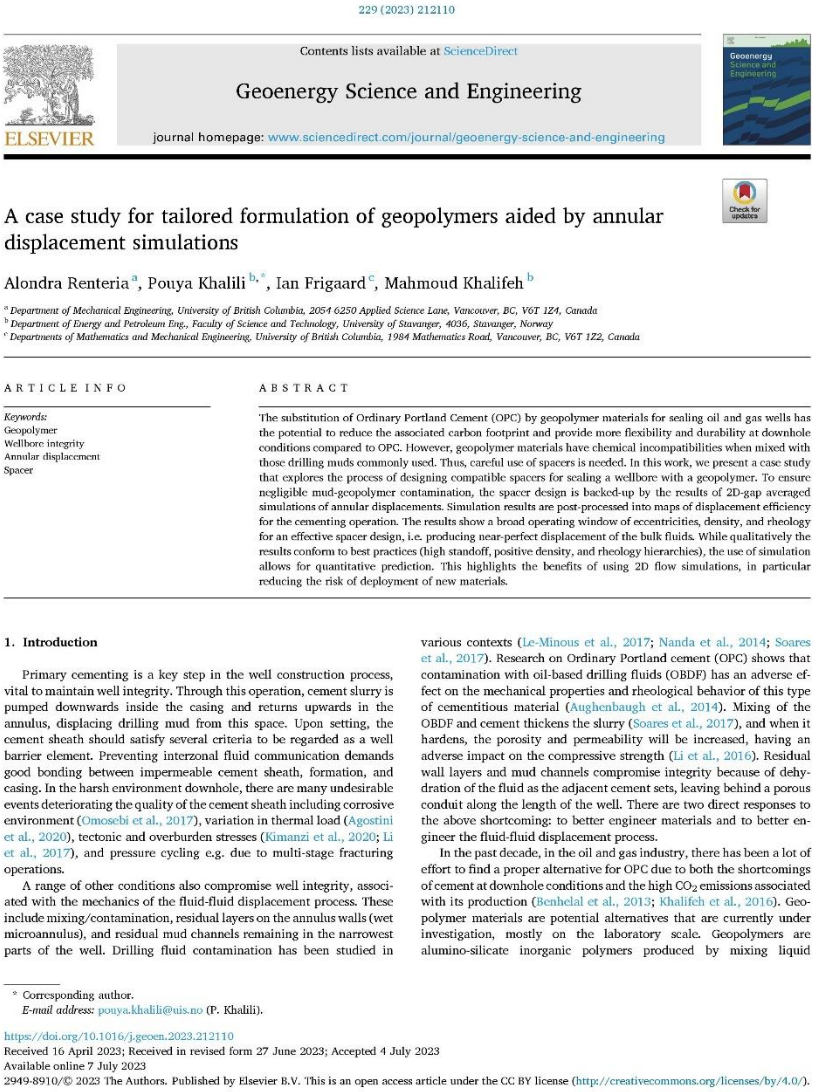

229 (2023) 212110

Contents lists available at ScienceDirect

Geoenergy Science and Engineering

journal homepage: www.sciencedirect.com/journal/geoenergy-science-and-engineering

A case study for tailored formulation of geopolymers aided by annular displacement simulations

Alondra Renteria[a], Pouya Khalili[b,*], Ian Frigaard[c], Mahmoud Khalifeh[b]

[a] *Department of Mechanical Engineering, University of British Columbia, 2054 6250 Applied Science Lane, Vancouver, BC, V6T 1Z4, Canada*
[b] *Department of Energy and Petroleum Eng., Faculty of Science and Technology, University of Stavanger, 4036, Stavanger, Norway*
[c] *Departments of Mathematics and Mechanical Engineering, University of British Columbia, 1984 Mathematics Road, Vancouver, BC, V6T 1Z2, Canada*

ARTICLE INFO

Keywords:
Geopolymer
Wellbore integrity
Annular displacement
Spacer

ABSTRACT

The substitution of Ordinary Portland Cement (OPC) by geopolymer materials for sealing oil and gas wells has the potential to reduce the associated carbon footprint and provide more flexibility and durability at downhole conditions compared to OPC. However, geopolymer materials have chemical incompatibilities when mixed with those drilling muds commonly used. Thus, careful use of spacers is needed. In this work, we present a case study that explores the process of designing compatible spacers for sealing a wellbore with a geopolymer. To ensure negligible mud-geopolymer contamination, the spacer design is backed-up by the results of 2D-gap averaged simulations of annular displacements. Simulation results are post-processed into maps of displacement efficiency for the cementing operation. The results show a broad operating window of eccentricities, density, and rheology for an effective spacer design, i.e. producing near-perfect displacement of the bulk fluids. While qualitatively the results conform to best practices (high standoff, positive density, and rheology hierarchies), the use of simulation allows for quantitative prediction. This highlights the benefits of using 2D flow simulations, in particular reducing the risk of deployment of new materials.

1. Introduction

Primary cementing is a key step in the well construction process, vital to maintain well integrity. Through this operation, cement slurry is pumped downwards inside the casing and returns upwards in the annulus, displacing drilling mud from this space. Upon setting, the cement sheath should satisfy several criteria to be regarded as a well barrier element. Preventing interzonal fluid communication demands good bonding between impermeable cement sheath, formation, and casing. In the harsh environment downhole, there are many undesirable events deteriorating the quality of the cement sheath including corrosive environment (Omosebi et al., 2017), variation in thermal load (Agostini et al., 2020), tectonic and overburden stresses (Kimanzi et al., 2020; Li et al., 2017), and pressure cycling e.g. due to multi-stage fracturing operations.

A range of other conditions also compromise well integrity, associated with the mechanics of the fluid-fluid displacement process. These include mixing/contamination, residual layers on the annulus walls (wet microannulus), and residual mud channels remaining in the narrowest parts of the well. Drilling fluid contamination has been studied in various contexts (Le-Minous et al., 2017; Nanda et al., 2014; Soares et al., 2017). Research on Ordinary Portland cement (OPC) shows that contamination with oil-based drilling fluids (OBDF) has an adverse effect on the mechanical properties and rheological behavior of this type of cementitious material (Aughenbaugh et al., 2014). Mixing of the OBDF and cement thickens the slurry (Soares et al., 2017), and when it hardens, the porosity and permeability will be increased, having an adverse impact on the compressive strength (Li et al., 2016). Residual wall layers and mud channels compromise integrity because of dehydration of the fluid as the adjacent cement sets, leaving behind a porous conduit along the length of the well. There are two direct responses to the above shortcoming: to better engineer materials and to better engineer the fluid-fluid displacement process.

In the past decade, in the oil and gas industry, there has been a lot of effort to find a proper alternative for OPC due to both the shortcomings of cement at downhole conditions and the high CO_2 emissions associated with its production (Benhelal et al., 2013; Khalifeh et al., 2016). Geopolymer materials are potential alternatives that are currently under investigation, mostly on the laboratory scale. Geopolymers are alumino-silicate inorganic polymers produced by mixing liquid

---

* Corresponding author.
E-mail address: pouya.khalili@uis.no (P. Khalili).

https://doi.org/10.1016/j.geoen.2023.212110
Received 16 April 2023; Received in revised form 27 June 2023; Accepted 4 July 2023

hardener with reactive aluminum and silicate source (precursor) such as fly ash, rice husk ash, metakaolin, red mud, and naturally occurring rocks. Mechanisms that are involved in geopolymerization are dissolution of aluminosilicate solid particles in high pH environment and creation of Si–O–H, transportation of molecules because of higher activity of ions and yielding oligomers, and polycondensation by gluing the oligomers which results in 3D structure. The product is combination of crystalline, and amorphous to semi-crystalline three-dimensional aluminosilicate chains. These three-dimensional long chains of aluminum silicate exhibit, *inter alia*, lower permeability, chemical shrinkage, and fluid loss (Khalifeh et al., 2016, 2019). Studies on geopolymers have shown that it has different behavior compared to OPC when it comes to contamination with drilling fluids (Eid et al., 2021). Geopolymer is more sensitive to water-based drilling fluid (WBDF), due to the geopolymerization process that involves releasing water, unlike the hydration process in OPC. WBDF acts as a dilutant for geopolymer and reduces the rheology profile. Contamination with OBDF increases the gel strength of the geopolymer. Oil droplets convert the water continuous geopolymer to an o/w emulsion. Thus, when at rest, due to an increase in phase volume, colloidal interaction, and gel strength are developed in the fluid (Barnes et al., 1989). Although, at higher shear rates, because of deformability, oil droplets change from spherical to ellipsoidal shape and cause contaminated slurry viscosity to fall below the neat geopolymer. Contamination with OBDF has an adverse impact on geopolymer compressive strength (Eid et al., 2021; Khalili et al., 2022). Therefore, in order to realise the considerable advantages of using geopolymers, one needs to understand the fluid-fluid displacement process, so that contamination/mixing can be kept under control.

Fluid mechanics of cement placement has been studied since the 1960's (McLean et al., 1967). While the hydraulics aspects of cementing circulation were studied quite early (summarized e.g. by Nelson (1990)), primary cementing is a single pass displacement flow, i.e. the drilling mud must be replaced by the cement slurry. This makes the fluid mechanics aspects much more complex. By the early 1990's rule-based design systems had evolved (Couturler et al., 1990; Ryan et al., 1992), and were becoming implemented in one-dimensional wellbore hydraulics software codes. These systems had many positives in terms of simplicity but failed to predict the actual defects of the displacement process. Equally, they targeted vertical wells, so that shortcomings were exposed by the shift towards horizontal drilling of the late 1990s.

A new era of cementing simulation started with the 2D gap-averaged (2DGA) model of Bittleston et al. (2002). The theoretical background to this style of model and robust computational methods were established by Pelipenko and Frigaard (2004a); Pelipenko and Frigaard (2004b), who also made the connection to the earlier rule-based systems (Pelipenko and Frigaard, 2004c), showing them to be conservative. The importance of this transition to the 2DGA framework cannot be overstated. It was now possible to simulate and visualise steady-state annular displacement flows, as well as unsteady and unstable flows. Using the same framework, the 2DGA model has been used to study horizontal annuli displacement flows (Carrasco-Teja et al., 2008), displacement flows with a moving inner cylinder (Carrasco-Teja and Frigaard, 2009, 2010; Tardy and Bittleston, 2015), turbulent and mixed regime displacement flows (Maleki and Frigaard, 2017, 2018, 2019). In the past decade, these simulations have become an industry standard, often matching/predicting defects measured later in field case studies.

Although recent years have seen the advent of three-dimensional (3D) computational fluid dynamics simulations (Etrati and Frigaard, 2019; Kragset and Skadsem, 2018; Sarmadi et al., 2021, 2022; Skadsem et al., 2019a, 2019b), these calculations face serious challenges when simulating a full wellbore. Simply put, if a 3D code is used it is in order to resolve physics on the scale of the annular gap. However, the mesh refinement needed on these scales, combined with mesh aspect ratio limits for computational accuracy, means that the numbers of mesh cells become astronomical on the size of the well. Additionally, computational times must be scaled with the cube of the number of axial mesh cells. This means that high quality computations, repeatable over ranges of operational parameters, are currently restricted to lengths of 20–50 m of the wellbore.

Thus, for the present, the 2DGA approach represents the state of the art for studying mud removal and cement placement. A quality mud removal process includes carefully designing cement slurry, preflush, and drilling fluid, as well as performing displacement simulations based on the available well and operational data. The preflush is a buffer fluid, pumped ahead of cement slurry, with density close to water (washes) or densified/viscosified (spacer). The latter is more advanced chemically and needs to be designed carefully in terms of density and rheology to ensure efficient displacement (Gordon et al., 2008; Nelson and Guillot, 2006), as well as considerations of chemical compatibility in case of mixing and contamination.

This paper aims to develop a simulation-aided design strategy for the displacement of sequence of fluids (mud, spacer, geopolymer), targeted at geopolymer placement i.e., inside an eccentric annulus. The strategy is focused on a typical North Sea well. In the first step, we collect well geometry data, intended pump rates, approximate mud rheology, and density. We simulate the displacement using the 2DGA approach and assuming only generic (invented) spacer properties. This informs the development of a tailored spacer. Not only must the rheology and density fit with the preliminary simulations, but the design must be compatible spacers with both mud and geopolymer. Given the relatively new utilization of geopolymers in primary cementing, a chemically compatible spacer has been developed for this emerging technology. Lastly, we return to the 2DGA simulations with the tailored spacer to verify that the displacement will be effective and that the mud and geopolymer won't mix. Typically, displacement simulations are conducted using a finalized spacer design to evaluate its performance. However, if the simulation results suggest that a redesign is necessary, it can be costly and time-consuming. The proposed spacer design procedure aims to streamline this process by suggesting the optimal rheology and density upfront, making the previously laborious task of optimizing spacer density and rheology more efficient and less prone to the need for redesigning.

2. Case study presentation

This paper discusses mud displacement/geopolymer placement in a North Sea platform well that has a depth of 2811 m TVD and was completed as a production well with four casings. The two particular casings (surface and intermediate casing) for which the displacement is investigated have casing shoes located at 522 m and 1374 m TVD. Rock-based geopolymer slurry with adequate pumping time was developed at the University of Stavanger (Chamssine et al., 2022) and measured rheological data was used to perform the simulation. OBDF, WBDF, and spud mud with a mix design close to the actual field drilling fluids were synthesized in the laboratory. Three different spacer fluids were designed based on the chemical compatibility with geopolymer and simulation results. Mix design, the method of preparation of fluids, and the procedure of testing the rheological properties of the fluids are described in detail in the following.

2.1. Geopolymer formulation

Two different geopolymer slurry designs were selected as appropriate for the type of casing and temperature profile; see Table 1. Geopolymer slurries were prepared using a commercial Constant Speed Blender, and following API standard (American Petroleum Institute, 2013). The solid precursor rich in aluminosilicate was added to liquid hardener in 15s at 4000 rpm and afterward the slurry was further mixed for 35s at 12000 rpm. Solid precursor was a blend of granite, ground granulated blast furnace slag (GGBFS), and microsilica. The geopolymer mix design and solid precursor composition are listed in Tables 1 and 2. Prior to each set of tests, the slurry was conditioned in OFITE

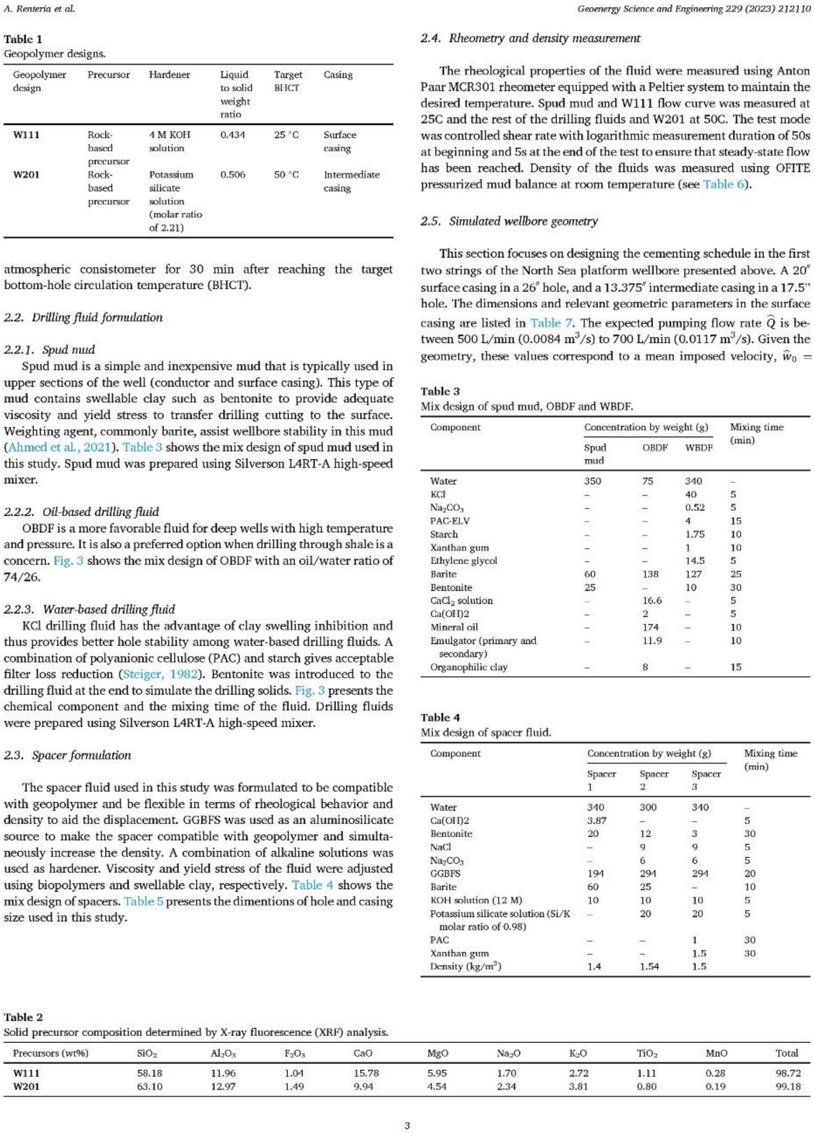

Table 1
Geopolymer designs.

Geopolymer design	Precursor	Hardener	Liquid to solid weight ratio	Target BHCT	Casing
W111	Rock-based precursor	4 M KOH solution	0.434	25 °C	Surface casing
W201	Rock-based precursor	Potassium silicate solution (molar ratio of 2.21)	0.506	50 °C	Intermediate casing

atmospheric consistometer for 30 min after reaching the target bottom-hole circulation temperature (BHCT).

2.2. *Drilling fluid formulation*

2.2.1. *Spud mud*

Spud mud is a simple and inexpensive mud that is typically used in upper sections of the well (conductor and surface casing). This type of mud contains swellable clay such as bentonite to provide adequate viscosity and yield stress to transfer drilling cutting to the surface. Weighting agent, commonly barite, assist wellbore stability in this mud (Ahmed et al., 2021). Table 3 shows the mix design of spud mud used in this study. Spud mud was prepared using Silverson L4RT-A high-speed mixer.

2.2.2. *Oil-based drilling fluid*

OBDF is a more favorable fluid for deep wells with high temperature and pressure. It is also a preferred option when drilling through shale is a concern. Fig. 3 shows the mix design of OBDF with an oil/water ratio of 74/26.

2.2.3. *Water-based drilling fluid*

KCl drilling fluid has the advantage of clay swelling inhibition and thus provides better hole stability among water-based drilling fluids. A combination of polyanionic cellulose (PAC) and starch gives acceptable filter loss reduction (Steiger, 1982). Bentonite was introduced to the drilling fluid at the end to simulate the drilling solids. Fig. 3 presents the chemical component and the mixing time of the fluid. Drilling fluids were prepared using Silverson L4RT-A high-speed mixer.

2.3. *Spacer formulation*

The spacer fluid used in this study was formulated to be compatible with geopolymer and be flexible in terms of rheological behavior and density to aid the displacement. GGBFS was used as an aluminosilicate source to make the spacer compatible with geopolymer and simultaneously increase the density. A combination of alkaline solutions was used as hardener. Viscosity and yield stress of the fluid were adjusted using biopolymers and swellable clay, respectively. Table 4 shows the mix design of spacers. Table 5 presents the dimentions of hole and casing size used in this study.

2.4. *Rheometry and density measurement*

The rheological properties of the fluid were measured using Anton Paar MCR301 rheometer equipped with a Peltier system to maintain the desired temperature. Spud mud and W111 flow curve was measured at 25C and the rest of the drilling fluids and W201 at 50C. The test mode was controlled shear rate with logarithmic measurement duration of 50s at beginning and 5s at the end of the test to ensure that steady-state flow has been reached. Density of the fluids was measured using OFITE pressurized mud balance at room temperature (see Table 6).

2.5. *Simulated wellbore geometry*

This section focuses on designing the cementing schedule in the first two strings of the North Sea platform wellbore presented above. A 20″ surface casing in a 26″ hole, and a 13.375″ intermediate casing in a 17.5" hole. The dimensions and relevant geometric parameters in the surface casing are listed in Table 7. The expected pumping flow rate $\widehat{Q}$ is between 500 L/min (0.0084 m^3/s) to 700 L/min (0.0117 m^3/s). Given the geometry, these values correspond to a mean imposed velocity, $\widehat{w}_0 =$

Table 3
Mix design of spud mud, OBDF and WBDF.

Component	Concentration by weight (g)			Mixing time (min)
	Spud mud	OBDF	WBDF	
Water	350	75	340	–
KCl	–	–	40	5
Na_2CO_3	–	–	0.52	5
PAC-ELV	–	–	4	15
Starch	–	–	1.75	10
Xanthan gum	–	–	1	10
Ethylene glycol	–	–	14.5	5
Barite	60	138	127	25
Bentonite	25	–	10	30
$CaCl_2$ solution	–	16.6	–	5
Ca(OH)2	–	2	–	5
Mineral oil	–	174	–	10
Emulgator (primary and secondary)	–	11.9	–	10
Organophilic clay	–	8	–	15

Table 4
Mix design of spacer fluid.

Component	Concentration by weight (g)			Mixing time (min)
	Spacer 1	Spacer 2	Spacer 3	
Water	340	300	340	–
Ca(OH)2	3.87	–	–	5
Bentonite	20	12	3	30
NaCl	–	9	9	5
Na_2CO_3	–	6	6	5
GGBFS	194	294	294	20
Barite	60	25	–	10
KOH solution (12 M)	10	10	10	5
Potassium silicate solution (Si/K molar ratio of 0.98)	–	20	20	5
PAC	–	–	1	30
Xanthan gum	–	–	1.5	30
Density (kg/m^3)	1.4	1.54	1.5	

Table 2
Solid precursor composition determined by X-ray fluorescence (XRF) analysis.

Precursors (wt%)	SiO_2	Al_2O_3	F_2O_3	CaO	MgO	Na_2O	K_2O	TiO_2	MnO	Total
W111	58.18	11.96	1.04	15.78	5.95	1.70	2.72	1.11	0.28	98.72
W201	63.10	12.97	1.49	9.94	4.54	2.34	3.81	0.80	0.19	99.18

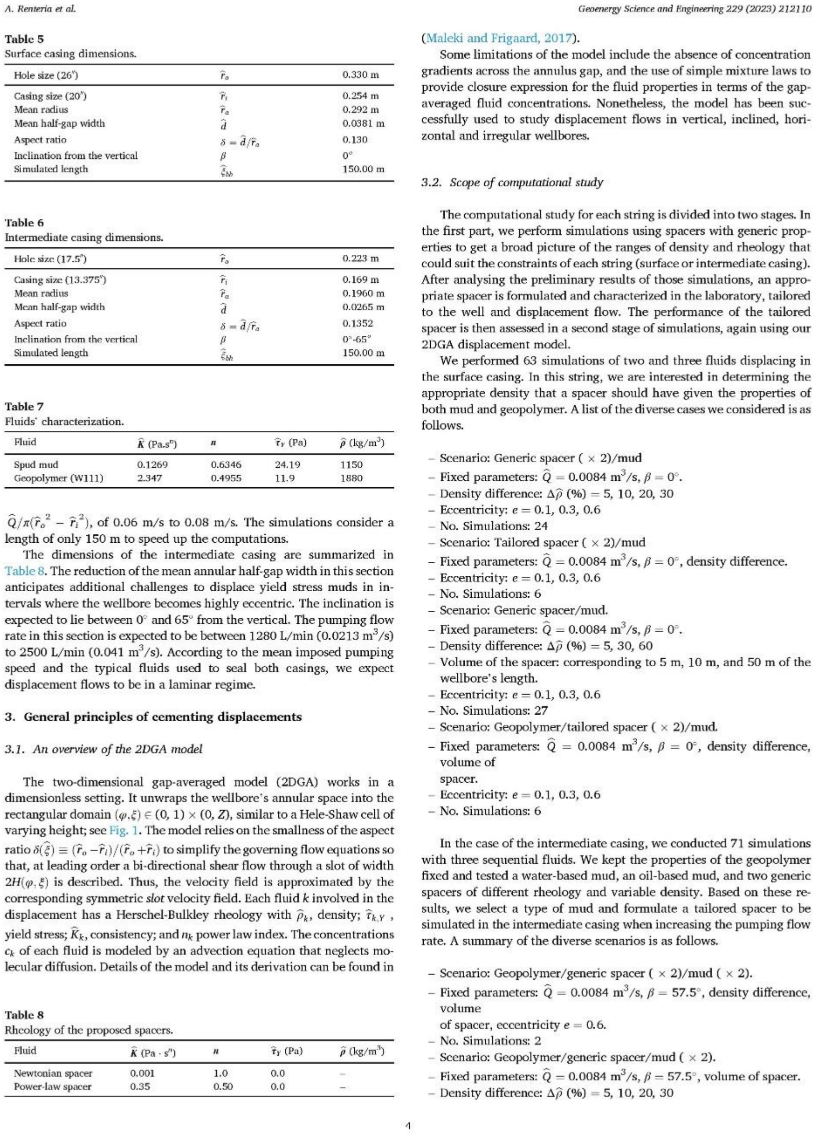

Table 5
Surface casing dimensions.

Hole size (26″)	$\widehat{r}_o$	0.330 m
Casing size (20″)	$\widehat{r}_i$	0.254 m
Mean radius	$\widehat{r}_a$	0.292 m
Mean half-gap width	$\widehat{d}$	0.0381 m
Aspect ratio	$\delta = \widehat{d}/\widehat{r}_a$	0.130
Inclination from the vertical	β	0°
Simulated length	$\widehat{\xi}_{bh}$	150.00 m

Table 6
Intermediate casing dimensions.

Hole size (17.5″)	$\widehat{r}_o$	0.223 m
Casing size (13.375″)	$\widehat{r}_i$	0.169 m
Mean radius	$\widehat{r}_a$	0.1960 m
Mean half-gap width	$\widehat{d}$	0.0265 m
Aspect ratio	$\delta = \widehat{d}/\widehat{r}_a$	0.1352
Inclination from the vertical	β	0°-65°
Simulated length	$\widehat{\xi}_{bh}$	150.00 m

Table 7
Fluids' characterization.

Fluid	$\widehat{K}$ (Pa.s^n)	n	$\widehat{\tau}_Y$ (Pa)	$\widehat{\rho}$ (kg/m^3)
Spud mud	0.1269	0.6346	24.19	1150
Geopolymer (W111)	2.347	0.4955	11.9	1880

$\widehat{Q}/\pi(\widehat{r}_o{}^2 - \widehat{r}_i{}^2)$, of 0.06 m/s to 0.08 m/s. The simulations consider a length of only 150 m to speed up the computations.

The dimensions of the intermediate casing are summarized in Table 8. The reduction of the mean annular half-gap width in this section anticipates additional challenges to displace yield stress muds in intervals where the wellbore becomes highly eccentric. The inclination is expected to lie between 0° and 65° from the vertical. The pumping flow rate in this section is expected to be between 1280 L/min (0.0213 m^3/s) to 2500 L/min (0.041 m^3/s). According to the mean imposed pumping speed and the typical fluids used to seal both casings, we expect displacement flows to be in a laminar regime.

3. General principles of cementing displacements

3.1. *An overview of the 2DGA model*

The two-dimensional gap-averaged model (2DGA) works in a dimensionless setting. It unwraps the wellbore's annular space into the rectangular domain $(\varphi, \xi) \in (0, 1) \times (0, Z)$, similar to a Hele-Shaw cell of varying height; see Fig. 1. The model relies on the smallness of the aspect ratio $\delta(\widehat{\xi}) \equiv (\widehat{r}_o - \widehat{r}_i)/(\widehat{r}_o + \widehat{r}_i)$ to simplify the governing flow equations so that, at leading order a bi-directional shear flow through a slot of width $2H(\varphi, \xi)$ is described. Thus, the velocity field is approximated by the corresponding symmetric *slot* velocity field. Each fluid k involved in the displacement has a Herschel-Bulkley rheology with $\widehat{\rho}_k$, density; $\widehat{\tau}_{k,Y}$, yield stress; $\widehat{K}_k$, consistency; and n_k power law index. The concentrations c_k of each fluid is modeled by an advection equation that neglects molecular diffusion. Details of the model and its derivation can be found in (Maleki and Frigaard, 2017).

Table 8
Rheology of the proposed spacers.

Fluid	$\widehat{K}$ (Pa · s^n)	n	$\widehat{\tau}_Y$ (Pa)	$\widehat{\rho}$ (kg/m^3)
Newtonian spacer	0.001	1.0	0.0	–
Power-law spacer	0.35	0.50	0.0	–

Some limitations of the model include the absence of concentration gradients across the annulus gap, and the use of simple mixture laws to provide closure expression for the fluid properties in terms of the gap-averaged fluid concentrations. Nonetheless, the model has been successfully used to study displacement flows in vertical, inclined, horizontal and irregular wellbores.

3.2. *Scope of computational study*

The computational study for each string is divided into two stages. In the first part, we perform simulations using spacers with generic properties to get a broad picture of the ranges of density and rheology that could suit the constraints of each string (surface or intermediate casing). After analysing the preliminary results of those simulations, an appropriate spacer is formulated and characterized in the laboratory, tailored to the well and displacement flow. The performance of the tailored spacer is then assessed in a second stage of simulations, again using our 2DGA displacement model.

We performed 63 simulations of two and three fluids displacing in the surface casing. In this string, we are interested in determining the appropriate density that a spacer should have given the properties of both mud and geopolymer. A list of the diverse cases we considered is as follows.

- Scenario: Generic spacer (× 2)/mud
- Fixed parameters: $\widehat{Q} = 0.0084$ m^3/s, $\beta = 0°$.
- Density difference: $\Delta\widehat{\rho}$ (%) = 5, 10, 20, 30
- Eccentricity: $e = 0.1, 0.3, 0.6$
- No. Simulations: 24
- Scenario: Tailored spacer (× 2)/mud
- Fixed parameters: $\widehat{Q} = 0.0084$ m^3/s, $\beta = 0°$, density difference.
- Eccentricity: $e = 0.1, 0.3, 0.6$
- No. Simulations: 6
- Scenario: Generic spacer/mud.
- Fixed parameters: $\widehat{Q} = 0.0084$ m^3/s, $\beta = 0°$.
- Density difference: $\Delta\widehat{\rho}$ (%) = 5, 30, 60
- Volume of the spacer: corresponding to 5 m, 10 m, and 50 m of the wellbore's length.
- Eccentricity: $e = 0.1, 0.3, 0.6$
- No. Simulations: 27
- Scenario: Geopolymer/tailored spacer (× 2)/mud.
- Fixed parameters: $\widehat{Q} = 0.0084$ m^3/s, $\beta = 0°$, density difference, volume of spacer.
- Eccentricity: $e = 0.1, 0.3, 0.6$
- No. Simulations: 6

In the case of the intermediate casing, we conducted 71 simulations with three sequential fluids. We kept the properties of the geopolymer fixed and tested a water-based mud, an oil-based mud, and two generic spacers of different rheology and variable density. Based on these results, we select a type of mud and formulate a tailored spacer to be simulated in the intermediate casing when increasing the pumping flow rate. A summary of the diverse scenarios is as follows.

- Scenario: Geopolymer/generic spacer (× 2)/mud (× 2).
- Fixed parameters: $\widehat{Q} = 0.0084$ m^3/s, $\beta = 57.5°$, density difference, volume of spacer, eccentricity $e = 0.6$.
- No. Simulations: 2
- Scenario: Geopolymer/generic spacer/mud (× 2).
- Fixed parameters: $\widehat{Q} = 0.0084$ m^3/s, $\beta = 57.5°$, volume of spacer.
- Density difference: $\Delta\widehat{\rho}$ (%) = 5, 10, 20, 30

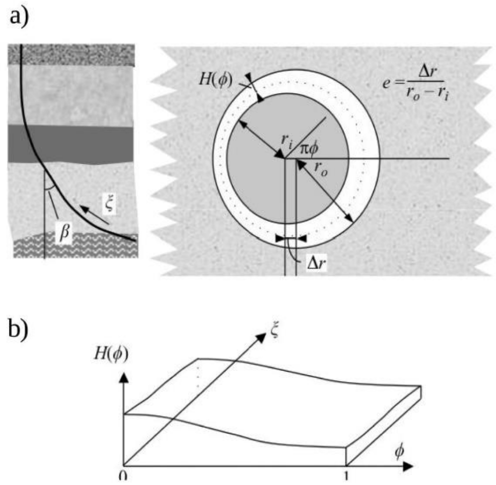

Fig. 1. Schematic of the well and of the variables that describe the eccentric annular geometry in a cross-section. Taken from (Pelipenko and Frigaard, 2004c).

- Eccentricity: $e = 0.1, 0.3, 0.6$
- No. Simulations: 24
- Scenario: Geopolymer/tailored spacer/mud.
- Fixed parameters: density difference, volume of spacer.
- Eccentricity: $e = 0, 0.2, 0.4, 0.6, 0.8$
- Flow rate: $\widehat{Q} = 0.021$ m^3/s, 0.029 m^3/s, 0.042 m^3/s.
- Inclination: $\beta = 0°, 45°, 65°$
- No. Simulations: 45

4. Results

All simulations were performed in half symmetric annulus to speed up the computations, thus allowing us to cover numerous scenarios. Note also that the simulated length for each casing is reduced to 150 m. This evidently speeds up the computation considerably. The other reason is simply that one does not need a very long annulus to discern if the displacement is effective or not. Below we present the results of annular displacements for each string.

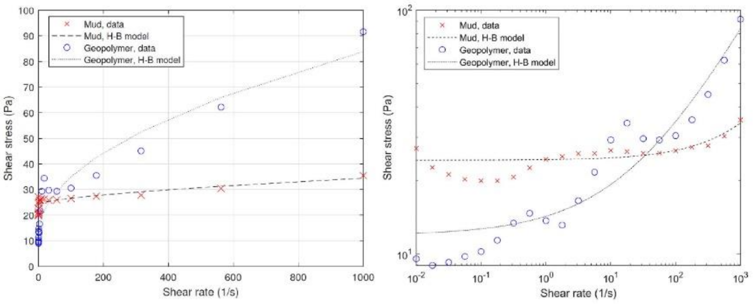

Fig. 2. Rheometry of spud mud and geopolymer. The dashed line shows fitting with the Herschel-Bulkley (H–B) model. (Left) linear scale (Right) logarithmic scale.

4.1. Simulations in the surface casing

Fig. 2 presents the measured flow curve for spud mud and geopolymer formulations. Both fluids display yield stress and shear-thinning behavior. The data have been fitted to the Herschel-Bulkley constitutive relationship; the resulting parameters for each fluid are reported in Table 7.

Given the large yield stress of the mud, it is expected that eccentricity and buoyancy stresses will dominate the displacement. Moreover, the substantially large density difference between mud and geopolymer offers a broad window for selecting the properties of a suitable spacer.

4.1.1. Displacements with generic spacers

We test displacing the mud in Table 7 by two spacers of different rheology and several density values. The rheological parameters of the spacers are reported in Table 8. The first spacer is a Newtonian fluid of low viscosity, and the second spacer is a power-law fluid with high consistency and shear-thinning properties. Fig. 3 illustrates the apparent viscosity of mud, geopolymer, and the proposed spacers. Both mud and geopolymer present shear-thinning behavior and large yield stress. Their flow curves are similar across five decades of shear rate. However, the large difference in density contrast ($730\ \mathrm{kg/m^3}$) between these two fluids leaves plenty of room for selecting a spacer of intermediate density.

In terms of rheology, the Newtonian fluid may represent a low viscous wash; whereas the power-law fluid is a more viscous spacer. This contrasting rheology was selected to demonstrate the relative effect of rheology versus buoyancy when displacing in the surface casing.

Both generic spacers are tested individually, in a sequence of only two fluids in the annulus (mud-spacer). The density of each spacer is varied to achieve a density difference between spud mud (1) and spacer (2) of, $\Delta\widehat{\rho} = (\widehat{\rho}_2 - \widehat{\rho}_1)/\widehat{\rho}_1 \times 100$, of 5%, 10%, 20%, and 30%. The flow rate in all cases is fixed at $0.0084\ \mathrm{m^3/s}$ ($0.06\ \mathrm{m/s}$).

Fig. 4 shows a summary of the resulting mud-Newtonian spacer displacements mapped for different levels of eccentricity and increasing the spacer density. Each sub-figure in Fig. 4 presents a concentration map at three stages in the displacement ($t = 31, 45, 150$). The concentration of the in-situ mud and the displacing spacer are represented by blue and red, respectively. The annulus is unwrapped so that **W** stands for the annular gap wide side and **N** for the narrow side in the azimuthal coordinate φ. The flow proceeds from bottom to top, in the direction of the axial coordinate ξ. The streamlines of the flow are presented in white.

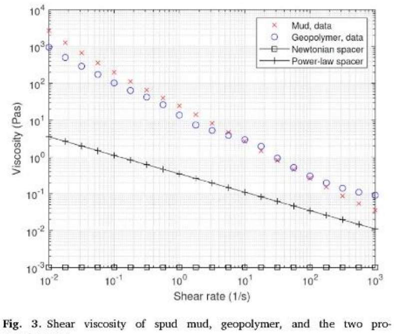

Fig. 3. Shear viscosity of spud mud, geopolymer, and the two proposed spacers.

We can separate the map into basically two main regions: incomplete and complete displacements, after pumping a given volume of spacer. The incomplete displacements are characterized by channeling of the displacing fluid towards the wide side of the eccentric annulus. This region is found when the displacing fluid has a low-density contrast with respect to the mud. Bypassing of the narrow side occurs for the three levels of eccentricity tested at $\Delta\rho = 5\%$. We also observe that on increasing eccentricity, the tip of the displacing front becomes more elongated until it resembles a spike at $e = 0.6$.

A similar effect of eccentricity can be seen when $\Delta\rho = 10\%$. In this case, values of moderate eccentricity ($e = 0.1, 0.3$) result in a dispersed front that moves towards the wide side of the annulus. Yet, the eccentricity effect is compensated by the secondary flows near the front driven by buoyancy force. In this way, the net result is a complete displacement at $e = 0.1, 0.3$, but is incomplete at $e = 0.6$ when eccentricity dominates. The remaining displacements in Fig. 4, with a larger density contrast ($\Delta\rho = 20, 30\%$), have successful displacements with a flat mud-spacer interface and slight dispersion for higher values of eccentricity.

We can also quantify the effectiveness of a displacement by computing the volumetric efficiency. This indicator is defined as the percentage of mud dis-placed at a given time. The efficiency can be computed from the 2DGA model simply by integrating the concentration (c_2) of the displacing fluid in the well at a given time:

$$\eta(t) = \frac{\int_0^{\xi_{bh}} \int_0^1 r_a H c_2(\varphi, \xi, t) d\varphi d\xi}{\int_0^{\xi_{bh}} \int_0^1 r_a H d\varphi d\xi} \tag{1}$$

Where $\eta(t)$ is the volumetric efficiency, t is the dimensionless time, ξ_{bh} is the measured bottom hole depth, r_a is the average radius, and H is the half annular gap width function. Fig. 5 shows the time evolution of the volumetric efficiency for the displacements shown in Fig. 4. In all cases, the volumetric efficiency ramps up from zero to a plateau at long times. The spacer with the lowest density contrast also presents the lowest volumetric efficiency at long times. Interestingly, in this case, increasing the eccentricity appears to improve the efficiency. The larger gap in the wide side of the annulus aids mud removal in that zone, although still bypassing the narrow side. On increasing the spacer's density contrast in Fig. 5 (ii) we observe that the volumetric efficiency rises considerably and improves with decreasing eccentricity. Finally, Fig. 5 (iii) and Fig. 5 (iv) present successful displacements with complete mud removal ($\eta = 1$).

Since the volumetric efficiency can grow rapidly when the displacement is effective in the wide side, high values of η may be misleading in terms of how truly effective the displacement with respect to wellbore integrity is. Even if the volume of mud left in the narrow side of the annulus is smaller than the portion removed in the wide side, it can still pose a risk of developing leakage paths. To correct for this fact, another way to evaluate mud removal with emphasis on wellbore integrity is the narrow side efficiency introduced by (Maleki and Frigaard, 2019). The narrow side efficiency is defined as the mud displaced in the narrowest quartile of the annulus at a given time:

$$\eta_N(t) = \frac{\int_0^{\xi_{bh}} \int_{3/4}^1 r_a H c_2(\varphi, \xi, t) d\varphi d\xi}{\int_0^{\xi_{bh}} \int_{3/4}^1 r_a H d\varphi d\xi} \tag{2}$$

The variables in (2) are as in equation (1). The integral in φ represents the azimuthal coordinate, and extends only over the narrowest quarter $\varphi \in [3/4, 1]$. Fig. 6 shows the narrow side efficiency, η_N, for the displacements shown in Fig. 4. Now we can notice that the spacer with the lowest density contrast in Fig. 6 (i) has effectively $\eta_N = 0$ at all times, indicating channeling of the narrow side. The volumetric efficiency in Fig. 5 (i) doesn't inform of the poor coverage in the narrow side. The effect of eccentricity is also better described using the narrow side efficiency. For example, in Fig. 6 (ii) when the eccentricity is large ($e = 0.6$), η_N indicates channeling of the mud in the narrow side, whereas, in Fig. 5 (ii) the effect of eccentricity appears only as a slight decrease in

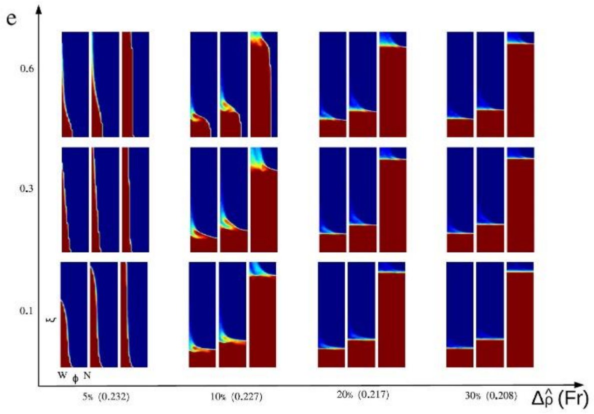

Fig. 4. Displacing mud (blue) by a Newtonian spacer (red), mapped in the eccentricity vs density difference plane. Dimensionless time in each concentration plot from left to right is t = 31, 45, 150.

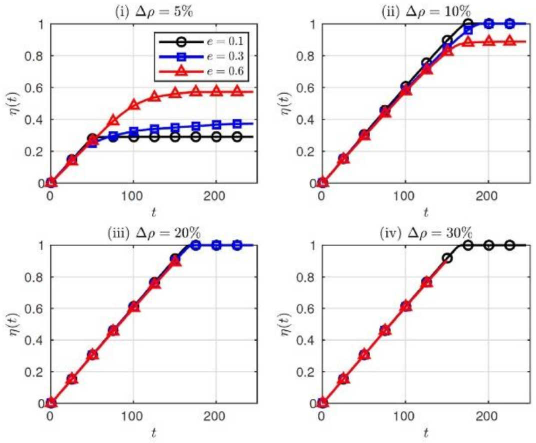
(i) $\Delta\rho = 5\%$

(ii) $\Delta\rho = 10\%$

(iii) $\Delta\rho = 20\%$

(iv) $\Delta\rho = 30\%$

Fig. 5. Volumetric efficiency for displacing the spud mud by a Newtonian spacer with increasing density contrast.

the volumetric efficiency. On the other hand, as we move to the larger density differences in Fig. 6(iii) and 6 (iv), we observe little difference between the narrow side efficiencies and the displacement efficiencies (Fig. 5). These larger density differences are sufficient to remove the mud from the narrow side, even for eccentricity up to 0.6.

In summary, the Newtonian spacer performs better when formulated with a density contrast of at least 10% and wellbores with a moderate eccentricity ($e \leq 0.3$). The secondary flows driven by the density difference aid to stabilize

The mud-spacer interface, resulting in the complete removal of the mud. Therefore, provided that there is a sufficient density contrast between the two fluids, the particular rheology of the spacer will have little

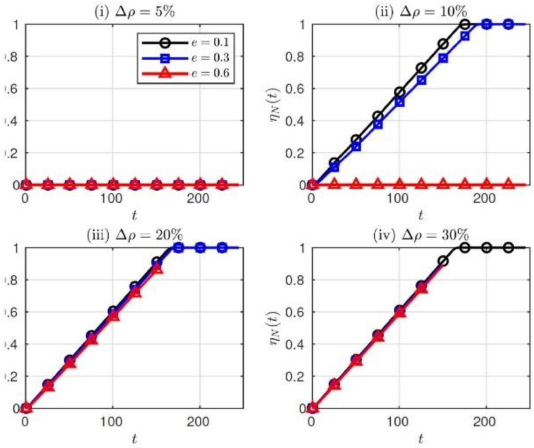

Fig. 6. Narrow side efficiency for displacing the mud by a Newtonian spacer with increasing density contrast.

impact.

To illustrate this point, let's consider now the same displacement sequences, but testing the power-law spacer shown in Table 8. This shear-thinning fluid has considerably larger effective viscosity compared to the Newtonian spacer. Fig. 7 shows a summary of the several displacements with the power-law spacer, different levels of density contrast (5%, 10%, 20%, 30%), and the three eccentricities studied ($e = 0.1, 0.3, 0.6$). The map resembles the one presented in Fig. 4 with minimal differences observed by eye. Upon detailed inspection of the volumetric efficiency presented in Fig. 8, we observe a subtle

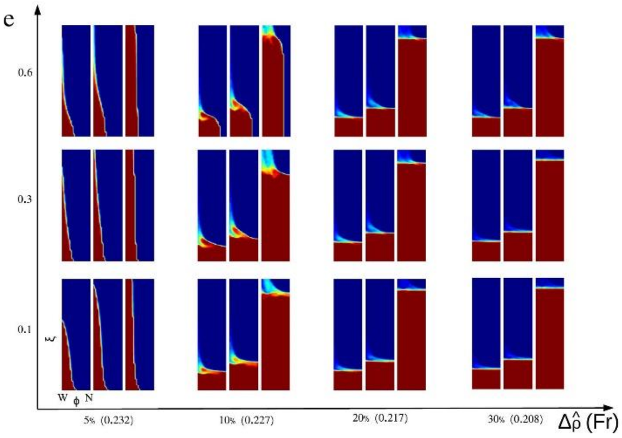

Fig. 7. Displacing mud (blue) by a Newtonian spacer (red), mapped in the eccentricity vs density difference plane. Dimensionless time in each concentration plot from left to right is t = 31, 45, 150.

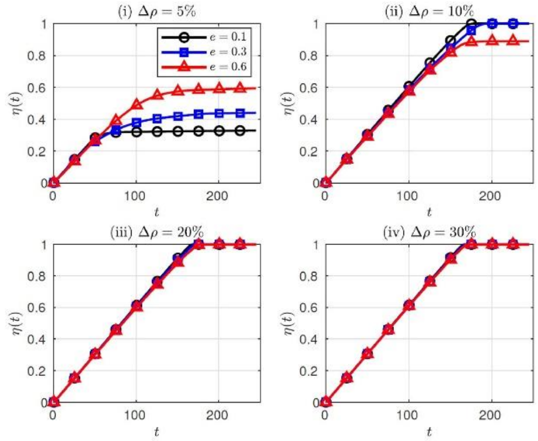

Fig. 8. Volumetric efficiency for displacing the mud by a power-law spacer.

increase in the efficiency curve for $e = 0.3$, Fig. 8 (i), compared with the low-viscous Newtonian spacer in Fig. 5 (i). Furthermore, the resulting narrow side efficiency, reported in Fig. 9, appears to be equivalent when using the Newtonian spacer (Fig. 6). In general, we would only expect improvements with a highly viscous spacer for mild eccentricities and fluids of similar densities.

4.1.2. Displacements with tailored spacers

Fig. 10 presents the measured flow curve of two spacers designed following the results of the generic spacers studied above. Spacer 1 has been fitted to a power-law constitutive equation, while Spacer 2 has been fitted to the Bingham model. Values for each fitting are reported in Table 9, along with their density.

Fig. 11 shows the displacement sequence for three fluids in the

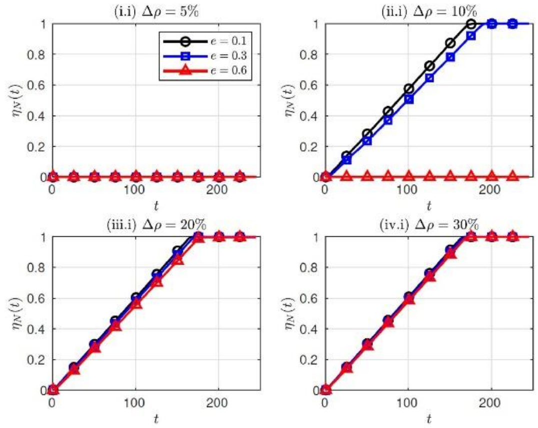

Fig. 9. Narrow side efficiency for displacing the mud by a power-law spacer.

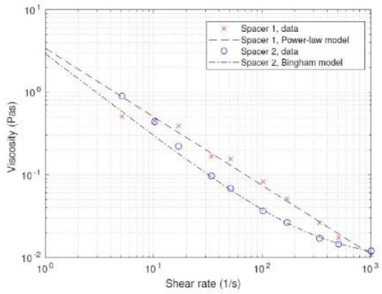

Fig. 10. Shear viscosity of the spacers and their fit to different constitutive relationships.

Table 9
Tailored spacer properties.

Fluid	$\hat{K}$ (Pa · s^n)	n	$\hat{\tau}_Y$ (Pa)	$\hat{\rho}$ (kg/m^3)
Spacer 1 (Power-law model)	3.406	0.17	0.0	1400
Spacer 2 (Bingham model)	0.0090	1.0	2.906	1540

annulus (mud-spacer-geopolymer), and three values of eccentricity (e = 0.1, 0.3, 0.6) when using spacer 1. Likewise, Fig. 12 shows the three-fluid displacement when considering the properties of spacer 2. Following the previous results from two-fluids displacements, the density contrast provided by any of the pairs mud/spacer 1 ($\Delta\rho = 21.74\%$) or mud/spacer 2 ($\Delta\rho = 33.91\%$) is sufficient to effectively remove the in-situ mud even at high eccentricities. Note, however, that on increasing the eccentricity the flow is restricted to the wide side of the annulus. This fact could result in traces of spacer left in the narrow side potentially contaminating the geopolymer. This scenario could be exacerbated if the spacer had a density similar to the geopolymer's. According to the results shown in Figs. 11 and 12, we can confirm that given the relatively wide annular gap and the vertical configuration of the surface casing, establishing a sufficiently high density difference between the sequence of fluids can result in a successful displacement via secondary flows. From the perspective of annular displacements, the high density of the geopolymer is advantageous to effectively remove even high yield stress muds in surface casings.

4.2. Simulations in the intermediate casing

Table 10 lists the properties of two different drilling fluids we test for drilling in the intermediate casing. The water-based drilling fluid is 110 kg/m^3 denser than the oil-based drilling fluid and has a smaller yield stress. Other H–B parameters describing their rheology are similar. The first set of simulations in the intermediate casing are aimed at selecting both the type of drilling fluid and a suitable spacer.

4.2.1. Displacements with generic spacers

We use the same proposed rheology for the generic Newtonian and power-law spacers listed in Table 8. We define a density difference of $\Delta\rho$ = 5% and eccentricity of $e = 0.6$. These parameters are set to compare how the two different drilling fluids would perform under a challenging environment.

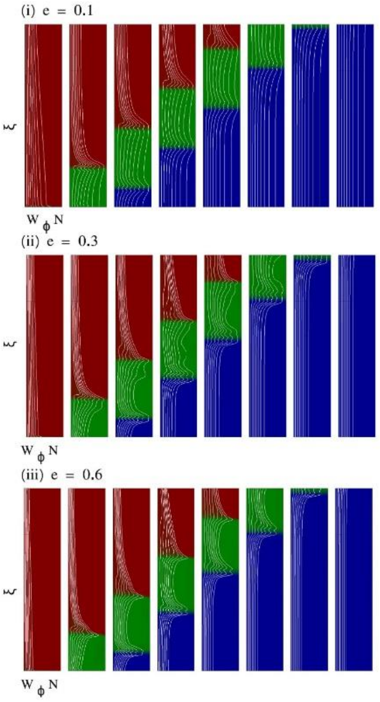

Fig. 11. Two fluids sequence pumping Spacer 1. Density differences are 21.74%.

Fig. 13 shows the advancing displacement when using the generic Newtonian spacer and either the water-based drilling fluid or the oil-based drilling fluid, Fig. 13 (i) and (ii), respectively. In both cases we observe that the flow is restricted to the wide side of the annular gap, resulting in some channeling of the mud by the spacer. This creates a long spacer/drilling fluid interface subject to mixing and developing instabilities. Particularly with the combination of oil-based drilling fluid/spacer the layer in the narrow side appears to develop buoyancy driven instabilities when lighter fingers of drilling fluid become internally trapped in the spacer (Fig. 13 (ii)). Because of the larger viscosity ratio between the oil-based drilling fluid and the Newtonian spacer, channeling in the narrow side is also more severe than the channeling occurring in the water-based drilling fluid (Fig. 13 (i)). Similar results are obtained when considering the power-law generic spacer.

Fig. 14 presents the resulting displacements for the sequences water-based drilling fluid/power-law spacer/geopolymer, Fig. 14 (i); and oil-based drilling fluid/power-law spacer/geopolymer. We have set again the same density contrast $\Delta\rho = 5\%$ and high eccentricity e = 0.6. The power-law spaces perform somehow better than the Newtonian when displacing water-based drilling fluid. Residual water-based drilling fluid in the narrow side of the gap is negligible. However, channeling of the

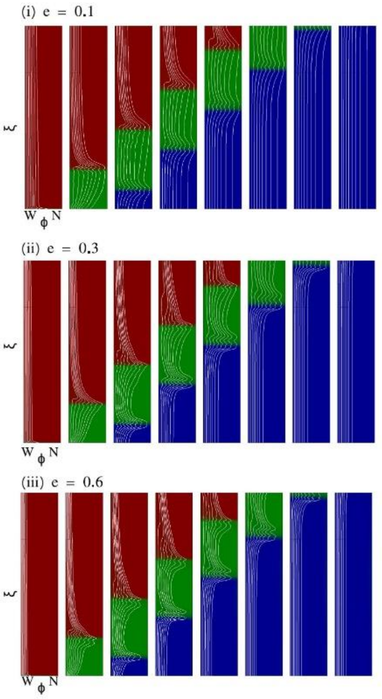

Fig. 12. Two fluids sequence pumping Spacer 2. Density differences are 33.91%.

Table 10
Rheology of fluids for intermediate casing.

Fluid	$\widehat{K}$ (Pa · sn)	n	$\widehat{\tau}_Y$ (Pa)	$\widehat{\rho}$ (kg/m3)
Water-based drilling fluid	0.381	0.5656	0.5385	1270
Oil-based drilling fluid	0.4975	0.5632	1.138	1160
Geopolymer (W201)	0.1636	0.9824	4.118	1980

oil-based drilling fluid in the narrow side remains present.

When looking at the performance of the spacer to remove the mud, the combi-nation water-based drilling fluid/power-law spacer seems more effective. Nevertheless, the large density of the geopolymer aids to remove either combination of drilling fluid/spacer at the end of the displacement.

4.2.2. *Displacements with tailored spacers*

Table 11 summarizes the properties of the fluids selected for the final simulations in the intermediate casing. The water-based drilling fluid was selected based on the results of the previous section. The properties

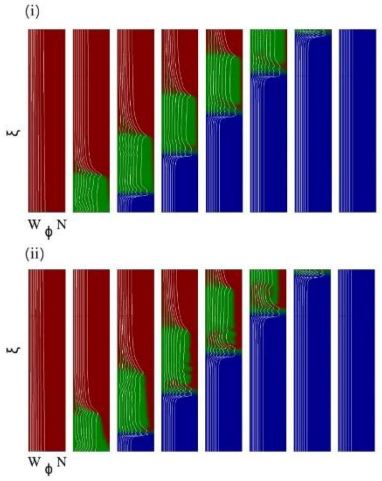

Fig. 13. A Newtonian spacer displacing (i) water-based drilling fluid (ii) oil-based drilling fluid. E = 0.6 Density differences are 5%.

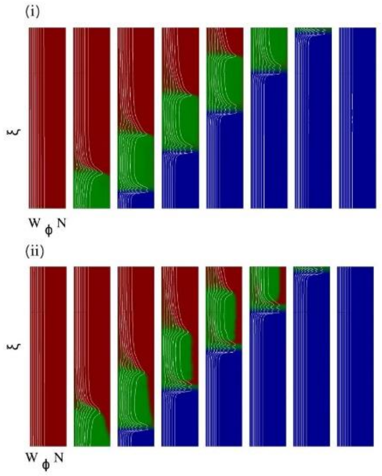

Fig. 14. A power-law spacer displacing (i) water-based drilling fluid (ii) oil-based drilling fluid. E = 0.6 Density differences are 5%.

Table 11
Rheology of fluids for intermediate casing.

Fluid	$\widehat{K}$ (Pa · s^n)	n	$\widehat{\tau}_Y$ (Pa)	$\widehat{\rho}$ (kg/m^3)
Water-based drilling fluid	0.381	0.5656	0.5385	1270
Geopolymer (W201)	0.1636	0.9824	4.118	1980
Spacer 3 (Herschel-Buckley)	0.4405	0.65	1.12	1500

of the geopolymer re-main fixed. The spacer designed for this section of the well has a Herschel-Buckley rheology, with a small yield stress and shear-thinning behavior. It has also an intermediate density of 1500 kg/m^3 when compared to the surface casing tailored spacers (Table 9).

A typical flow rate for an intermediate casing with the given dimensions is about 1600 L/min (0.027 m^3/s). We test three values of flow rate around this value: a flow rate reduced by 20%, $\widehat{Q}_1 = 1280$ L/min (0.0213 m^3/s); increased 10%, $\widehat{Q}_2 = 1760$ L/min (0.029 m^3/s); and increased 56%, $\widehat{Q}_3 = 2500$ L/min (0.041 m^3/s). Since the wellbore inclination in this section can vary significantly, we performed simulations for three representative values: 0°, 45°, and 65° from vertical.

Fig. 15 presents a colormap for the narrow side efficiency based on the volume of geopolymer in the annulus at the end of each simulation. The flow rate is fixed at $\widehat{Q}_1 = 1280$ L/min. The selected sequence of fluids water-based drilling fluid/geopolymer/tailored spacer is successful to remove the drilling fluid and place the geopolymer around the inclined annulus even when the eccentricity is moderate ($e \leq 0.6$). Only extreme values of eccentricity combined with deviations from the vertical (i.e., $e \geq 0.8$ and $\beta > 0$) can have a detrimental effect on the geopolymer coverage in the narrowest region of the annulus. As observed in the results of the simulations using generic spacers, when the wellbore is very eccentric, the flow tends to bypass the narrow gap thus increasing the risk of contaminating the geopolymer. The inclination of the wellbore decreases the buoyancy force provided driven by the density difference in the fluids. Increasing the flow rate does not have a major effect on the results. Figs. 16 and 17 report the narrow efficiency of the geopolymer when increasing the flow rate for the same scenarios shown in Fig. 15. In both cases, the efficiency of the displacing geopolymer is only limited in the narrow side by highly eccentric and inclined wellbores.

Fig. 18 illustrates a map of displacements with the three tested flow rates and inclinations at a fixed eccentricity of $e = 0.8$. Contamination of the geopolymer in the narrow side is noticeable in all cases. The spacer becomes less effective at displacing the narrow side with increasing inclination and to a lesser extent, with increasing flow rate.

Geopolymers exhibit promising mechanical and rheological characteristics, making them a viable alternative to ordinary Portland cement (OPC) with the added advantage of lower CO2 emissions. The challenge now lies in implementing geopolymer in the annulus for practical use. The findings of 2D flow displacement simulation in higher section of the well indicate a wide range of suitable eccentricities, densities, and rheological properties for designing an efficient spacer. This design enables effective placement of the geopolymer. Thus, this approach helps mitigate the potential risks associated with introducing new materials. Future research directions could explore the placement of geopolymer in lower sections of the well, particularly in cases where horizontal annulus is prevalent. Additionally, investigating geopolymer application in boreholes with geometrical irregularities such as washouts, keyseats, and breakouts would be valuable areas of study.

5. Summary

This paper has presented a design methodology for tailoring the properties of spacers and applied this to a specific case of a geopolymer placement in a typical North Sea well. The method consists of 3 stages. First, a preliminary simulation study using generic spacer properties to establish the broad feasibility of the displacement. Second, initial displacement results are used to tailor a spacer that will fit within the scope from stage 1, but which also satisfies properties such as compatibility between mud and geopolymer, where contamination can be more sensitive. The final design stage checks the tailored spacer (density and rheology) within a second simulation study, to verify that the proposed spacer is effective. This method can minimize the risk of failure

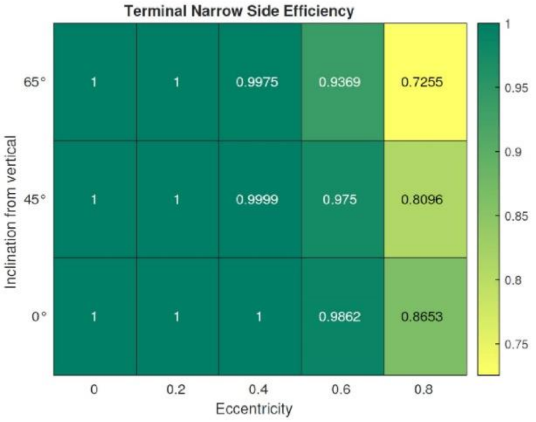

Fig. 15. Summary of the Narrow side efficiency after pumping 1.2 annular volumes of geopolymer at $\widehat{Q}_1$. The sequence is water-based drilling fluid/spacer 3/geopolymer.

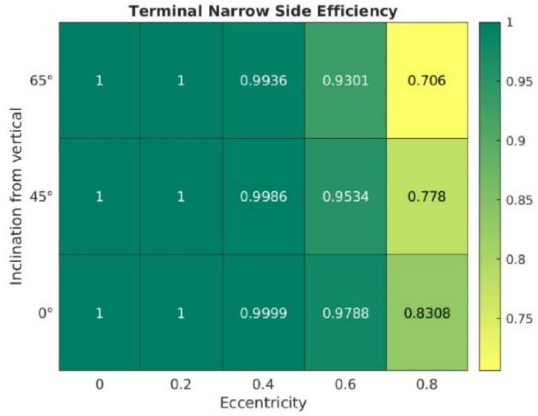

Fig. 16. Summary of the Narrow side efficiency after pumping 1.2 annular volumes of geopolymer at $\hat{Q}_2$. The sequence is water-based drilling fluid/spacer 3/geopolymer.

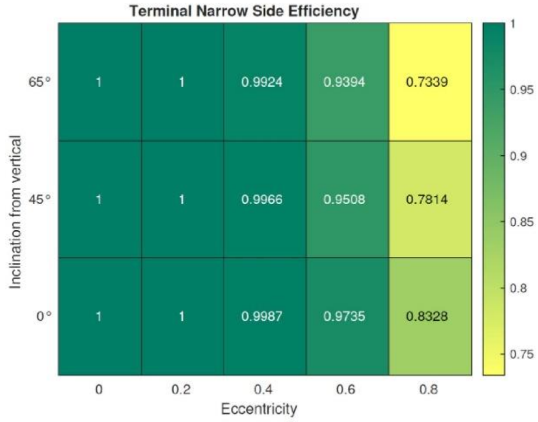

Fig. 17. Summary of the Narrow side efficiency after pumping 1.2 annular volumes of geopolymer at $\hat{Q}_3$ The sequence is water-based drilling fluid/spacer 3/geopolymer.

associated with placement of a new cementitious material such as severe mud contamination and potential well integrity failure. Thus, contributing to a more sustainable energy development process.

The use of simulation in this type of iterative design represents part of the innovation of the paper, the other being the application to geopolymer placement. Given that two-dimensional gap-averaged simulation models are widely available to the industry, using these tools to expose potential design flaws is imperative. Post-processing to create maps such as Figs. 15–17, together with the visual impact of simulations that show the fluid placement, is relatively quick to perform. This is important both educationally and practically. Scoping out design windows in this manner is certainly feasible on the timescales of deep

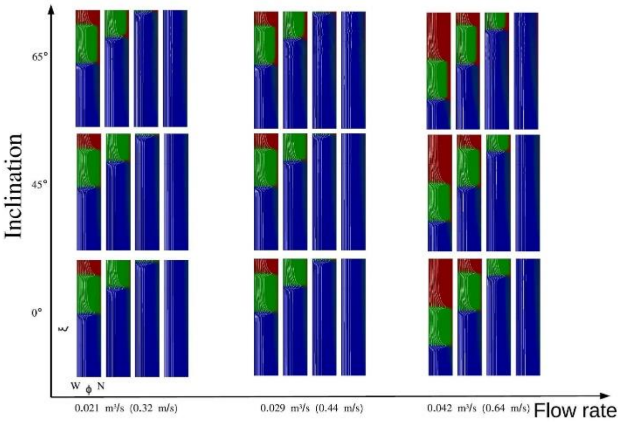

Fig. 18. Concentration maps when increasing inclination and flow rate. The eccentricity is fixed at $e = 0.8$. For the flow rate 0.021 m^3/s and 0.029 m^3/s, the dimensionless time in each concentration plot from left to right is $t = 213.5, 266.5, 319.5, 372.5$. For the flow rate 0.042 m^3/s, $t = 144.5, 216, 288, 359.5$.

offshore wells and could be performed routinely for groups of onshore wells, e.g. pad drilled with similar characteristics.

The high density of the geopolymer is advantageous in annular displacements in vertical and moderately inclined wells. It provides a large density window to design a suitable spacer and creates the required buoyancy to remove both mud and spacer from the narrow side of vertical and close-to-vertical wellbores. Our simulations results reveal a broad range of parameters where the displacement will be effective and the geopolymer may be reliably used.

The only constraint for this particular case study is to keep a high standoff (above 20%, eccentricity <0.8). Such eccentricities should be possible with recommended centralizer placement in the vertical parts of the well. Indeed, it is common to recommend standoff above 30% in best practices. Thus, we do not see this as constraining. Of course, lower in the well as we come to the production casing with longer casing runs and increased inclination, achieving a good standoff is always problematic. This aspect is not however specific to the geopolymer application. Study of the production casing cement placement is part of our future plan.

Lastly, we acknowledge some limitations in our study. First, model results are only as good as their assumptions. Enhanced two-dimensional models and three-dimensional simulations are coming. Although these will refine the analysis and allow a better understanding of dispersion, mixing, and wet microannulus phenomena, the current model predictions on bulk displacement and efficiencies will not change. Secondly, we emphasize that our study on geopolymer usage has been confined to fluid mechanical phenomena (rheology and displacement mechanics). Other factors such as wellhead geometry/equipment and varying geological conditions also need studying before these are widely adopted.

Declaration of competing interest

The authors declare that they have no known competing financial interests or personal relationships that could have appeared to influence the work reported in this paper.

Data availability

Data will be made available on request.

Acknowledgements

PK & MK gratefully acknowledge TotalEnergies, AkerBP, ConocoPhillips and Research Council of Norway for financially supporting the SafeRock KPN Project (RCN #319014- New Cementitious Material for Oil Well Cementing Applications - SafeRock) at the University of Stavanger, Norway.

IAF & AR acknowledge financial from NSERC and Schlumberger through CRD Project.No. 516022–17.

References

Agostini, C.E., et al., 2020. Thermal Shock Transient Analysis for Well Integrity through Operational Envelope. Offshore Technology Conference.

Ahmed, A., Alsaihati, A., Elkatatny, S., 2021. An overview of the common water-based formulations used for drilling onshore gas wells in the Middle East. Arabian J. Sci. Eng. 46 (7), 6867–6877.

Aughenbaugh, K., Nair, S., Cowan, M., van Oort, E., 2014. Contamination of deepwater well cementations by synthetic-based drilling fluids. In: SPE Deepwater Drilling and Completions Conference, Galveston, Texas, USA, September 2014 Paper Number: SPE-170325-MS. https://doi.org/10.2118/170325-MS.

Barnes, H.A., Hutton, J.F., Walters, K., 1989. An Introduction to Rheology. Elsevier, Netherlands.

Benhelal, E., Zahedi, G., Shamsaei, E., Bahadori, A., 2013. Global strategies and potentials to curb CO2 emissions in cement industry. J. Clean. Prod. 51, 142–161.

Bittleston, S.H., Ferguson, J., Frigaard, I.A., 2002. Mud removal and cement placement during primary cementing of an oil well – laminar non-Newtonian displacements in an eccentric annular Hele-Shaw cell. J. Eng. Math. 43 (2), 229–253.

Carrasco-Teja, M., Frigaard, I.A., 2009. Displacement flows in horizontal, narrow, eccentric annuli with a moving inner cylinder. Phys. Fluids 21 (7), 073102.

Carrasco-Teja, M., Frigaard, I.A., 2010. Non-Newtonian fluid displacements in horizontal narrow eccentric annuli: effects of slow motion of the inner cylinder. J. Fluid Mech. 653, 137–173.

Carrasco-Teja, M., Frigaard, I.A., Seymour, B.R., Storey, S., 2008. Viscoplastic fluid displacements in horizontal narrow eccentric annuli: stratification and travelling wave solutions. J. Fluid Mech. 605, 293–327.

Chamssine, F., Khalifeh, M., Saasen, A., 2022. Effect of Zn2+ and K+ as retarding agents on rock-based geopolymers for downhole cementing operations. J. Energy Resour. Technol. 144 (5).

Couturler, M., Guillot, D., Hendriks, H., Callet, F., 1990. Design Rules and Associated Spacer Properties for Optimal Mud Removal in Eccentric Annuli. CIM/SPE International Technical Meeting, Calgary, Alberta.

Eid, E., Tranggono, H., Khalifeh, M., Salehi, S., Saasen, A., 2021. Impact of drilling fluid contamination on performance of rock-based geopolymers. SPE J. 26 (6), 3626–3633.

Etrati, A., Frigaard, I., 2019. Laminar Displacement Flows in Vertical Eccentric Annuli: Experiments and Simulations, ASME 2019 38th International Conference on Ocean, Offshore and Arctic Engineering.

Gordon, C.L., Lewis, S.J., Tonmukayakul, P., 2008. Rheological Properties of Cement Spacer: Mixture Effects. AADE Fluids Conference and Exhibition, Texas. April 8-9.

Institute, A.P., 2013. API RP 10B-2, Recommended Practice for Testing Well Cements. API, Washington, DC.

Khalifeh, M., Saasen, A., Hodne, H., Motra, H.B., 2019. Laboratory evaluation of rock-based geopolymers for zonal isolation and permanent P&A applications. J. Petrol. Sci. Eng. 175, 352–362.

Khalifeh, M., Saasen, A., Vrålstad, T., Larsen, H.B., Hodne, H., 2016. Experimental study on the synthesis and characterization of aplite rock-based geopolymers. Journal of Sustainable Cement-Based Materials 5 (4), 233–246.

Khalili, P., Khalifeh, M., Saasen, A., 2022. The Effect of Fluid Contamination on Rheological Properties of Geopolymer Materials, ASME 2022 41st International Conference on Ocean, Offshore and Arctic Engineering.

Kimanzi, R., Wu, Y., Salehi, S., Mokhtari, M., Khalifeh, M., 2020. Experimental evaluation of geopolymer, nano-modified, and neat class H cement by using diametrically compressive tests. J. Energy Resour. Technol. 142 (9).

Kragset, S., Skadsem, H.J., 2018. Effect of Buoyancy and Inertia on Viscoplastic Fluid: Fluid Displacement in an Inclined Eccentric Annulus with an Irregular Section, ASME 2018 37th International Conference on Ocean, Offshore and Arctic Engineering.

Le-Minous, J.C., et al., 2017. Permeability Study of API Class G and B Cements Considering Seawater and WBM Contamination. SPE/IADC Drilling Conference and Exhibition.

Li, B., Li, H., Zhou, F., Guo, B., Chang, X., 2017. Effect of cement sheath induced stress on well integrity assessment in carbon sequestration fields. J. Nat. Gas Sci. Eng. 46, 132–142.

Li, Z., Liu, H., Guo, X., Ou, H., Gu, T., 2016. Contamination of cement slurries with oil based mud and its components in cementing operations. J. Nat. Gas Sci. Eng. 29, 160–168.

Maleki, A., Frigaard, I., 2017. Primary cementing of oil and gas wells in turbulent and mixed regimes. J. Eng. Math. 107 (1), 201–230.

Maleki, A., Frigaard, I.A., 2018. Turbulent displacement flows in primary cementing of oil and gas wells. Phys. Fluids 30 (12), 123101.

Maleki, A., Frigaard, I.A., 2019. Comparing laminar and turbulent primary cementing flows. J. Petrol. Sci. Eng. 177, 808–821.

McLean, R.H., Manry, C.W., Whitaker, W.W., 1967. Displacement mechanics in primary cementing. J. Petrol. Technol. 19 (2), 251–260.

Nanda, J.K., Patil, A.R., Pal, O.R., 2014. Evaluation of Contaminated Cement Returns: A Case Study, International Petroleum Technology Conference.

Nelson, E.B., 1990. Well Cementing. Schlumberger Educational Services.

Nelson, E.B., Guillot, D., 2006. Well Cementing. Schlumberger.

Omosebi, O.A., et al., 2017. Cement Degradation in CO2 - H2S Environment under High Pressure-High Temperature Conditions. SPE Bergen One Day Seminar.

Pelipenko, S., Frigaard, I.A., 2004a. On steady state displacements in primary cementing of an oil well. J. Eng. Math. 46 (1), 1–26.

Pelipenko, S., Frigaard, I.A., 2004b. Two-dimensional computational simulation of eccentric annular cementing displacements. IMA J. Appl. Math. 69 (6), 557–583.

Pelipenko, S., Frigaard, I.A., 2004c. Visco-plastic fluid displacements in near-vertical narrow eccentric annuli: prediction of travelling-wave solutions and interfacial instability. J. Fluid Mech. 520, 343–377.

Ryan, D.F., Kellingray, D.S., Lockyear, C.F., 1992. Improved Cement Placement on North Sea Wells Using a Cement Placement Simulator. European Petroleum Conference.

Sarmadi, P., Renteria, A., Frigaard, I.A., 2021. Primary cementing of horizontal wells. Displacement flows in eccentric horizontal annuli. Part 2. Computations. J. Fluid Mech. 915, A83.

Sarmadi, P., Renteria, A., Thompson, C., Frigaard, I.A., 2022. Effects of wellbore irregularity on primary cementing of horizontal wells, Part 2: small scale effects. J. Petrol. Sci. Eng. 210, 110026.

Skadsem, H.J., Kragset, S., Lund, B., Ytrehus, J.D., Taghipour, A., 2019a. Annular displacement in a highly inclined irregular wellbore: experimental and three-dimensional numerical simulations. J. Petrol. Sci. Eng. 172, 998–1013.

Skadsem, H.J., Kragset, S., Sørbø, J., 2019b. Cementing an Irregular Annulus Geometry: Full-Scale Experiments and 3D Simulations. SPE/IADC International Drilling Conference and Exhibition.

Soares, A.A., et al., 2017. Cement slurry contamination with oil-based drilling fluids. J. Petrol. Sci. Eng. 158, 433–440.

Steiger, R.P., 1982. Fundamentals and use of potassium/polymer drilling fluids to minimize drilling and completion problems associated with hydratable clays. J. Petrol. Technol. 34 (8), 1661–1670.

Tardy, P.M.J., Bittleston, S.H., 2015. A model for annular displacements of wellbore completion fluids involving casing movement. J. Petrol. Sci. Eng. 126, 105–123.

Appendix 7 – IP (front page)

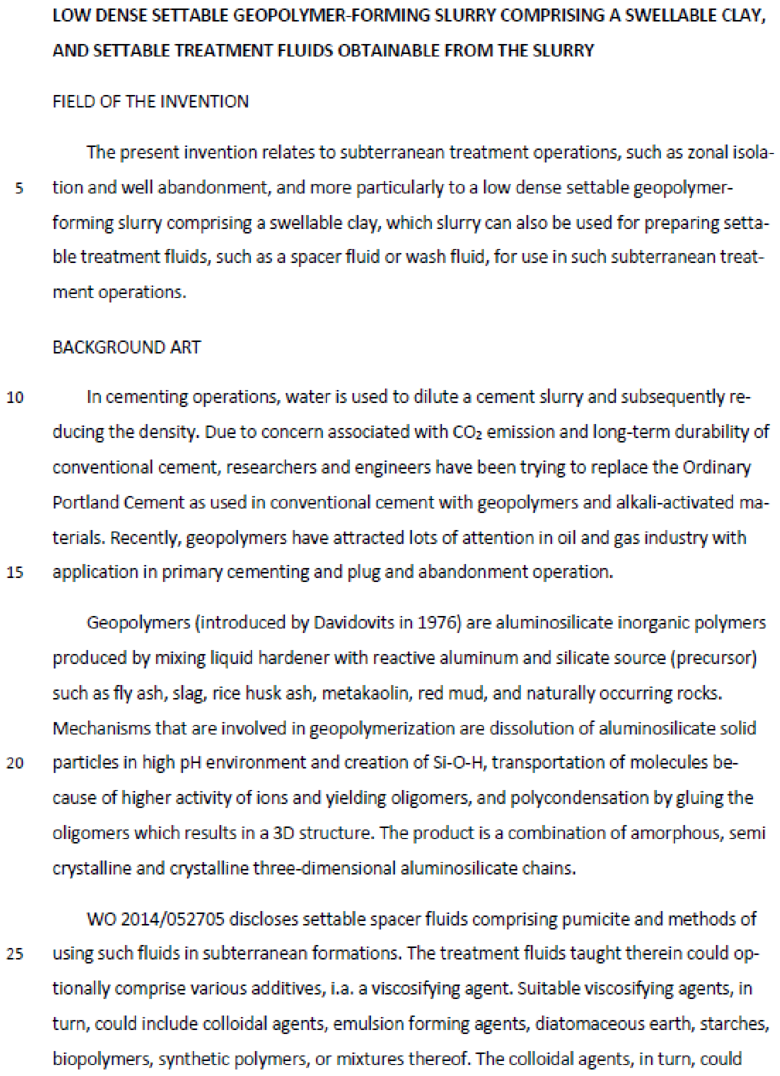

LOW DENSE SETTABLE GEOPOLYMER-FORMING SLURRY COMPRISING A SWELLABLE CLAY, AND SETTABLE TREATMENT FLUIDS OBTAINABLE FROM THE SLURRY

FIELD OF THE INVENTION

The present invention relates to subterranean treatment operations, such as zonal isolation and well abandonment, and more particularly to a low dense settable geopolymer-forming slurry comprising a swellable clay, which slurry can also be used for preparing settable treatment fluids, such as a spacer fluid or wash fluid, for use in such subterranean treatment operations.

BACKGROUND ART

In cementing operations, water is used to dilute a cement slurry and subsequently reducing the density. Due to concern associated with CO_2 emission and long-term durability of conventional cement, researchers and engineers have been trying to replace the Ordinary Portland Cement as used in conventional cement with geopolymers and alkali-activated materials. Recently, geopolymers have attracted lots of attention in oil and gas industry with application in primary cementing and plug and abandonment operation.

Geopolymers (introduced by Davidovits in 1976) are aluminosilicate inorganic polymers produced by mixing liquid hardener with reactive aluminum and silicate source (precursor) such as fly ash, slag, rice husk ash, metakaolin, red mud, and naturally occurring rocks. Mechanisms that are involved in geopolymerization are dissolution of aluminosilicate solid particles in high pH environment and creation of Si-O-H, transportation of molecules because of higher activity of ions and yielding oligomers, and polycondensation by gluing the oligomers which results in a 3D structure. The product is a combination of amorphous, semi crystalline and crystalline three-dimensional aluminosilicate chains.

WO 2014/052705 discloses settable spacer fluids comprising pumicite and methods of using such fluids in subterranean formations. The treatment fluids taught therein could optionally comprise various additives, i.a. a viscosifying agent. Suitable viscosifying agents, in turn, could include colloidal agents, emulsion forming agents, diatomaceous earth, starches, biopolymers, synthetic polymers, or mixtures thereof. The colloidal agents, in turn, could